A Review of Advances in Multifunctional $XTiO_3$ Perovskite-type Oxides as (photo)(Piezo)-catalysts for Environmental Remediation and Energy Production

Ridha Djellabi, Marcela Frias Ordonez, Francesco Conte, Ermelinda Falletta, Claudia L. Bianchi, Ilenia Rossetti

Corresponding author:

Abstract

Multifunctional $XTiO_3$ perovskites have drawn outstanding interest towards environmental remediation and energy conversion thanks to their unique structural, optical, physiochemical, electrical and thermal characteristics. $XTiO_3$ perovskites are able to initiate different surface catalytic reactions. Under ultrasonic vibration or heating, $XTiO_3$ perovskites can induce piezo-catalytic reactions due to the titling of their conduction and valence bands, resulting ~~on~~ in the formation of separated charge carriers in the medium. ~~By contrast~~In addition, under light irradiation, $XTiO_3$ perovskites are considered as a new class of photocatalysts for environmental and energy related applications. ~~Interestingly~~Furthermore, synergistic piezo-photocatalytic processes have received much attention recently for multi-ultrafast catalytic reactions. The engineering of $XTiO_3$ perovskite-type oxides is the backbone to control their ~~behavior~~ properties and performance~~and efficiency~~ ~~whatever~~ whichever their application. In the present ~~report~~review, we focus on the recent advances on variously synthesized, doped and formulated $XTiO_3$ perovskite-type oxides showing piezo- and/or photocatalytic exploitation in environmental remediation and energy conversion.

Keywords: $XTiO_3$ Perovskites, Piezocatalysis, Photocatalysis, Environmental remediation, Energy conversion.

Graphical abstract

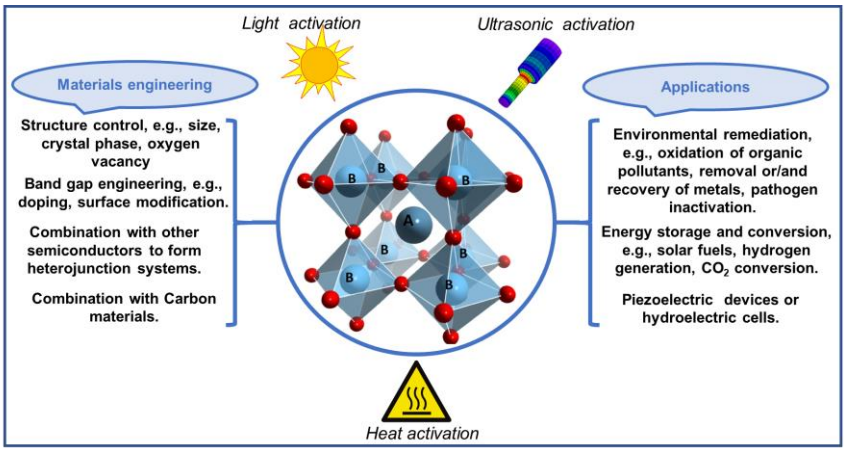

Table of contents

I. Introduction

Nowadays, due to the dramatic increase in worldwide population, associated with a huge industrialization and consumption of natural resources, the world is facing two main issues, the first is concerning the environmental protection and remediation [1-3] and the second is basically related to the energy control, storage and alternative conversion [4-6]. The scientific and industrial communities are struggling to find solutions to the above-mentioned challenges. Therefore, alternative economic and eco-techniques are strongly recommended for continuous and safe applicability. Currently, research on materials science and engineering is one of the hottest topics. Developing a material with special and/or tailored characteristics is the successful way for a convincing real application. Although the engineering of materials is the strongest leader behind the fast recent technology advances, the scientific community keeps addressing the materials science to narrow the gap towards the real use of smart materials in several applications including environmental and energy fields. Perovskite materials, named after the Russain mineralogist, Lev Alekseyevich von Perovski, are an exceptional class of materials thanks to their large availability, fascinating physicochemical, photonic and piezoelectric characteristics, making them very useful in a wide range of everyday and emerging applications such as solar cells, field effect transistors, environmental remediation, energy storage and conversion, electronic devices and so on [7-12]. The standard perovskite is calcium titanate ($CaTiO_3$) [11], however, perovskite-structured materials include compounds in the form of XBX_3, e.g., $SrTiO_3$, $BaTiO_3$, $CaRbF_3$, $LaAlO_3$, $BaCeO_3$, $BaZrO_3$, etc. Among these materials,

$XTiO_3$ perovskite-type oxides have been ~~widely~~ extensively reported for a wide range of usages. The interesting thing in this class of materials is their multifunctionality in terms of applications as well as their availability.

Over the last decades, $XTiO_3$-based perovskites showed a great potential as piezo catalysts for the removal of organic and inorganic pollutants from water and air [13]. The piezo catalytic advanced oxidation process is based on the application of ultrasonic irradiation to induce the tilting of both the valence and conduction bands of piezocatalysts, resulting in the formation of separated redox charges, which in turn are able to form surface reactive oxygen species (ROSs) [14]. The high polarization potential in $XTiO_3$ piezocatalysts is a determinant key for enhanced generation of ROSs. Several modification routes have been reported to enhance the piezoactivity of $XTiO_3$ including the co-loading of co-cations or oxides to $XTiO_3$ [15-18], phase structure control [19, 20], oxygen vacancy control [21] morphology control [22, 23]. Zhao et al. [24] reported that the electrical conductivity of $Bi_{0.5}Na_{0.5}TiO_3$ is more decisive than the piezoelectric coefficient for enhanced piezocatalytic activity. In terms of piezo catalysis, the relationship between the piezo-materials and the used driving force (ultrasound or heating) is very significant to continuously generate redox charges on the surface of such materials.

On the other hand, recently $XTiO_3$ perovskites have drawn outstanding interest in the field of photocatalysis [25], thanks to their high ROSs yield generation as the result of the combination of photoexcitation and piezoelectric effects. On top of that, $XTiO_3$ based perovskites have been widely applied for the conversion of energy and

Commentato [IR1]: check that it is uniformly written. E.g. just before it was piezo cata···(with space), here without, below with pace and with "minus"

Commentato [IR2]:

Commentato [IR3]:

Commentato [IR4]:

photosynthesis [26-28]. Likewise, intensive research has been done to enhance the photocatalytic efficiency of $XTiO_3$ through common routes such as doping, surface modification and formation of heterojunction systems [29-32]. Interestingly, unlike conventional photocatalytic semiconductors, $XTiO_3$ photocatalysts can combine both the photocatalytic and piezocatalytic activities as a synergistic process on the same platform, wherein, many studies have been reported recently to investigate the piezo-photocatalytic ability of different $XTiO_3$ materials [19, 24, 33-36].

In this review, the most popular synthesis routes of $XTiO_3$-based materials were summarized. The modification of $XTiO_3$ materials and their combination with other oxides or carbon materials was addressed. Detailed discussion regarding the mechanistic pathways on $XTiO_3$ based materials under different driving force (ultrasonic, heat or/and light irradiation) towards the removal of organic/inorganic pollutants and pathogenic species were comparatively discussed. In addition, energy conversion using $XTiO_3$ based materials was commented, as well. The scheme in **Figure 1** summarizes the most popular $XTiO_3$ based materials engineering for the use in environmental and energy production, which was the aim of the present review.

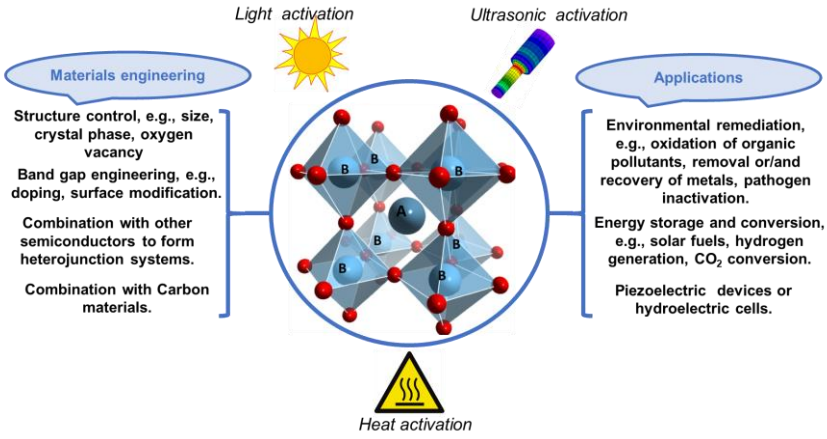

Figure 1. ~~Scheme shows the m~~Main $XTiO_3$ based materials and their common applications.

II. Synthesis and characterization of $XTiO_3$ materials

II.1. Synthesis

In $XTiO_3$ perovskite-type system, the physicochemical and photonic properties, e.g., crystal structure, light absorption, piezoelectric potential, conductivity, etc., are likely depending on the used synthesis route and structural/surface modification. In this section, the most reported synthesis routes and design of bare $XTiO_3$ perovskite-type oxides or their combination with other oxides will be discussed.

II.1.1. Solid-state synthesis

The solid-state reaction route is one of the most conventional method for the fabrication of bare $XTiO_3$ perovskite-type oxides such as $PbTiO_3$ [37], $BaTiO_3$ [38], $CaTiO_3$ [39], $SrTiO_3$ [40] and for the design of modified $XTiO_3$ perovskite-type oxides, e.g. $Pb(Zr_xTi_{1-x})O_3$ [41], (Pb, La)(Zr, Ti)O_3 [42], $(Bi_{1/2}Na_{1/2})TiO_3$-$BaTiO_3$ [43], (1-x)($Bi_{1/2}$

Formattato: Pedice

$Na_{1/2})TiO_3$-x$SrTiO_3$ [44], $(Ba_{0.83}Ca_{0.17})TiO_3$ [45], $Ba_{1-x-y}Sr_xCa_yTiO_3$ [46], $0.5Ba(Zr_{0.2}Ti_{0.8})O_3$ -$0.5(Ba_{0.7}Sr_{0.3})TiO_3$ [47], (1-x)$Ba(Sn,Ti)O_{3-x}(Ba,Ca)TiO_3$ [48]. It is widely used even at industrial scale because of easy-implementation based on the ball-milling mixing. The starting materials such as carbonates and oxides react under mechanical stress, followed by an extreme heating treatment (above 1273K) to create the desired crystalline structure [49]. However, this process has numerous disadvantages. For instance, from an environmental point of view, it consumes high-energy and organic solvents (e.g. ethanol) to assure an homogeneous mixing [40]. Moreover, it is hard to obtain pure and single-phase perovskite particles within nano-sized scale [49], which is strongly related to initial reactant powders particle size and the level of energy of the ball milling process. Lee et al. [49] have reported the fabrication of $(Bi_{0.5}Na_{0.5})TiO_3$ and their modified complex perovskites by a solvent-free mechanochemical reaction, starting from micro-sized reactant powders and using a high-energy planetary mill. The authors demonstrated that by improving parameters such as ball-impact energy and frequency, it was feasible to generate nano-crystalline and single-phase titanate perovskites in shorter reaction time (30-40 min), which resulted in lower calcination temperature and time.

II.1.2. Hydrothermal method

The hydrothermal method is characterized by chemical reactions performed in a sealed heated aqueous solution at high temperature and high autogenous pressure [50]. By changing the system parameters (e.g., temperature, reaction time, pH, precursor nature, precursor concentration and growth modifiers), the hydrothermal synthesis provides

benefits like controlled particle size and morphology. Additionally, hydrothermal synthesis allows the fabrication of high surface area $XTiO_3$ powders with a pure and fine crystalline structure compared to conventional methods [51], which can advantageously enhance the photocatalytic activity [22]. In terms of hydrothermal synthesis, in order to control the shape and the size of $XTiO_3$ based materials, the synthesis parameters such temperature, type of precursors and duration of synthesis reaction, etc., should be carefully investigated.

Fujinami et al. [52] reported the hydrothermal synthesis of $SrTiO_3$ in form of cubic nanoparticles by applying hydrazine and oleic acid (OLA) as controllers of cubic shape and particle size, respectively. Titanium bis(ammonium lactate) dihydroxide (TALH) and strontium hydroxide octahydrate were employed as water-soluble titanium and strontium precursors and the reaction was performed at 200ºC. The authors reported that $SrTiO_3$ nanoparticles exhibit cubic shape and with size lower than 10nm, highly dispersible in a non-polar organic solvent like hexane. It was mentioned that the use of oleic acid enhances the dispersibility of nanoparticles. While, $SrTiO_3$ NPs prepared without the use of oleic acid were found to be larger, aggregated and easily precipitated in hexane. Dang et al. [53] studied the effect of oleic acid and hydrazine on the formation of $SrTiO_3$ nanocubes. The study reported four morphologies by changing concentration ratios of Sr:OLA:Hydrazine ((1:1:1), (1:2:2), (1:2:4), (1:4:4)). The observations for each ratio were as follows: irregular morphology (1:1:1), monodispersed 20 nm nanocubes (1:2:2), broad size distribution nanocubes (1:2:4), non-cubic like particles (1:4:4), out of which the (1:2:2) ratio was the best.

On the other hand, Huang et al. [54] studied the effect of NaOH concentration, reaction time and temperature for the synthesis of $SrTiO_3$ nanocubes by hydrothermal treatment. P25-TiO_2 and $Sr(OH)_2 \cdot 2H_2O$ were used as starting materials. The authors used a ratio greater than 1 between Sr/Ti, to avoid secondary phases, besides the pH increase, which favors the formation of $SrTiO_3$. The addition of an alkaline mineralizer provoked aggregation, which contributed to cubic phase growth. The authors synthesized $SrTiO_3$ particles with a range of particle size of 20-100 nm considering 3M NaOH, 72 h and 130ºC as the best synthesis conditions.

Lee et al. [55] have studied the effect of some synthesis parameters to get a nano-cubic $BaTiO_3$ via hydrothermal method applying aqueous-P25-TiO_2 suspension, $Ba(OH)_2$, and NaOH as starting materials. The authors reported that the NaOH concentration plays an important role to get a high crystallinity of cubic phase $BaTiO_3$. It was reported also that $BaCO_3$ can be detected in small amount as its formation requires lower pH values compared to $BaTiO_3$. Furthermore, the authors mentioned that the increase in synthesis duration is an important key to generate a highly crystalline cubic-$BaTiO_3$. The size of $BaTiO_3$ can be precisely controlled ~~by~~ through the calcination temperature.

Kimijima et al. [56] reported the hydrothermal synthesis of controlled-cubic, concave-cubic and rod-like $CaTiO_3$ fine particles without the use of NaOH or KOH to adjust pH value to avoid Na^+ and K^+ ions impurities in the crystal structure in previous studies. A complex between titanium tetraisopropoxide (TIPO) and triethanolamine (TEOA) was used as one of the Ti-sources. The study highlighted the role of TEOA as a shape controller of cubic-like $CaTiO_3$ particles, besides preventing hydrolysis of TIPO in

aqueous solution. In addition, a degree of supersaturation between Ca and Ti - precursors is essential for the particle size control.

II.1.3. Electrospinning

Electrospinning method was initially used for the preparation of polymer fibers. However, it has expanded its field of application to ceramics and composites fibers synthesis due to its low-cost and simplicity, allowing a continuous fabrication of fibers down to ten nanometers [57, 58]. Most of these ceramic fibers conveyed piezoelectric, ferroelectric and catalytic properties. The core of this technique is the electrostatic interactions generated by the application of an electrostatic field [59]. The electrospinning setup can be divided in three main elements: a high voltage power supply, a spinneret and a collecting plate. **Figure 2** shows the electrospinning synthesis steps $(Bi_{1/2}Na_{1/2})TiO_3$-based nanofibers [16].

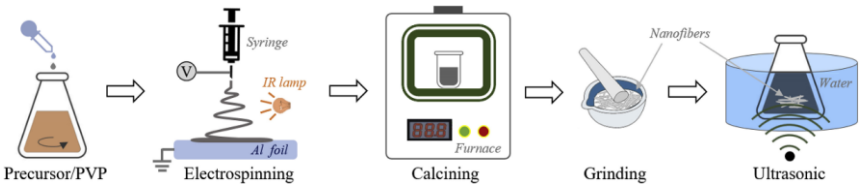

Figure 2. Step-by-step electrospinning synthesis $(Bi_{1/2}Na_{1/2})TiO_3$-based nanofibers. Reproduced with permission from [16].

Choi *et al.* [60] synthesized lead zirconate titanate (PZT) by electrospinning method starting from lead acetate trihydrate, zirconium ethoxide, titanium isopropoxide, polyvinylpyrrolidone, and applying different annealing processes (353, 723, 823, 923,

1023 and 1123K). The annealing process was applied in two different ways: direct (D) or stepwise (S). In the former ~~process~~option, the authors reported a diameter reduction tendency as the annealing temperature increased, whereas in the latter process the correlation between diameter and annealing temperature was directly proportional. The nanofibers were estimated within a diameter between 30-250 nm. Moreover, by X-ray diffraction analysis the authors observed PZT perovskite structure at annealing temperature of 823K [16]. Sahoo *et al.* [59] reported its synthesis by electrospinning method starting from PVP-$BaTiO_3$ composite nanofibers, which converted into pure $BaTiO_3$ fibers after a calcination procedure at 1273K. As precursors, the authors utilized barium carbonate, titanium acetate/titanium isopropoxide and PVP. The effect of polymer concentration on the final diameter of fibers was also studied, by varying its concentration within a range of 8-12%. It was found that at higher concentration of PVP, viscosity was modified, resulting in a growth of diameter as well, 150 nm for 8% PVP, and 250 nm for 12% PVP concentration **Figure 3.**

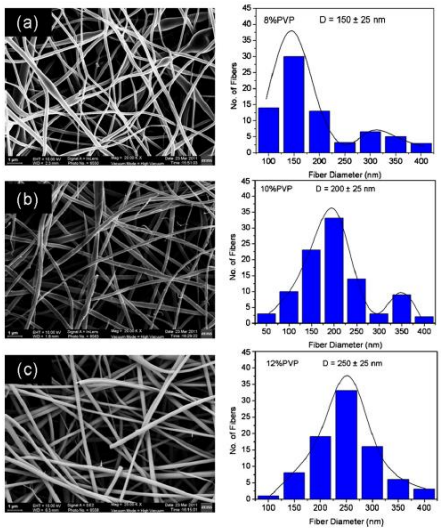

Figure 3. PVP-$BaTiO_3$ nanofibers synthesized with different polymer concentration: (a) 8%, (b) 10% and (c) 12% PVP concentration, and their equivalent size distribution. Reproduced with permission [59].

Bhardwaj and Kundu [61] discussed several parameters that can govern the electrospinning technique and the final fiber morphology. Hence, the authors classified them broadly in solution and process parameters. Firstly, solution concentration, polymer molecular weight, viscosity, surface tension and conductivity composed the solution parameters category. All these previous parameters are correlated to each other. Poly(ethylene oxide) (PEO), poly(vinylalcohol) (PVA), poly(vinylpyrrolidone) (PVP) are the most reported polymers for ceramic fibers synthesis with the purpose of controlling solution's viscosity. In the second category, process parameters applied voltage, feed rate, flow rate, types of collector and tip-to-collector distance are contained. In addition, it is reported that the ambient parameters such as humidity and temperature play a significant role in determining the final morphology and size of

electrospun fibers.

This technique has also been reported in combination with sol-gel process for the synthesis of 1D ceramic fibers with controllable composition, size, shape (core-sheath, hollow or porous structure) and in large quantities [62]. Fan *et al.* [63] reported the synthesis of ultra-fine lead zirconium titanate (PZT - $Pb(Zr_{0.3}, Ti_{0.7})O_3$) fibers prepared by the combination of these two methods. The authors used a 0.3M starting solution composed by lead acetate trihydrate, zirconium tetra n-propoxide, titanium (IV) butoxide in a mix of methanol/acetic acid solvents. Poly(vinylpyrrolidone) (PVP) was employed to modify the viscosity of the solution. The as-spun PZT/PVP composite fibers were deposited onto Si or $Au/SiO_2/Si$ substrates, dried and pre-heated at 400ºC for 30 min. Herein, the fibers underwent an annealing process at 550 and 650ºC for 30 min. The SEM images **Figure 4** showed PZT cylindrical nanofibers with a diameter ~100 nm, whereas the XRD pattern (**Figure 5**) exhibited a transition phase from amorphous phase (PZT/PVP composite fibers) to pyrochlore phase up to a tetragonal phase, characteristic of PZT, as the annealing temperature increased.

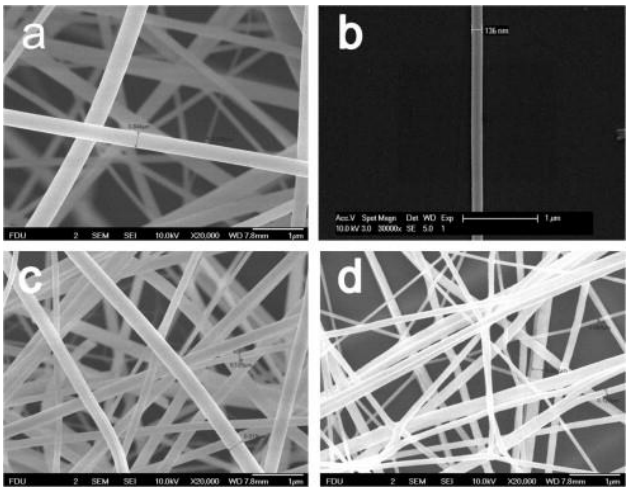

Figure 4. SEM images of PZT nanofibers: (a and b) PZT/PVP composite fibers, (c) fibers pre-heated at 400ºC, (d) fibers annealed at 650ºC. Reproduced with permission from [63].

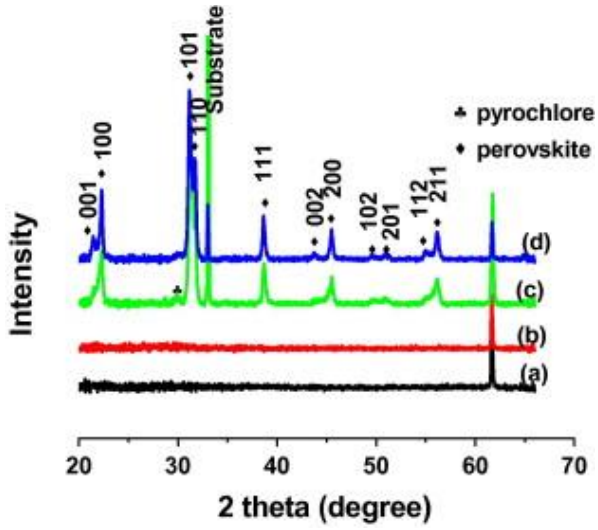

Figure 5. XRD pattern of PZT nanofibers: (a) PZT/PVP composite fibers, (b) fibers pre-heated at 400ºC, (c) fibers annealed at 500ºC, (d) fibers annealed at 650ºC.

Reproduced with permission from [63].

Other $XTiO_3$ such as $BaTiO_3$ [64], $NiTiO_3$ [65], $CdTiO_3$ [66], $MgTiO_3$ [67], and $(Bi_{1/2}Na_{1/2})TiO_3$-based nanofibers [16] have also been synthesized by electrospinning technique starting from sol-gel precursors. The average diameters oscillated between 80-190 nm, 150-200 nm, 150-200 nm and 200-400 nm, and 32-206 nm, respectively. Poly(vinylpyrrolidone) (PVP) and polyvinyl acetate (PVAc) were used as high molecular weight polymers for the fabrication of electrospun polymer nanofibers that underwent into a heating process.

II.1.4. Sol-gel synthesis

Sol-gel is a well-known wet chemical route that allows the manufacture of high-quality $XTiO_3$ – based materials and their composites. The sol-gel synthesis provides several advantages such as easy to implementation, inexpensiveness, high quality products and production of materials with large surface areas [68]. Surface properties can be excellently controlled through these five step-process: hydrolysis, condensation, aging, drying and crystallization (**Figure 6**) [69]. The first step, hydrolysis, ~~it~~ can take place in an aqueous or non-aqueous (organic solvents like alcohols) mediums. An acid or a base can be also added as a catalyst of hydrolysis, which is carried out at near room temperature and ~~it~~ employs metal alkoxides or acetylacetonates as precursors. Subsequently, the condensation is associated to the formation of a polymer network made of metal oxides linkages as a result of the elimination of water or alcohol

molecules, giving rise to a sol. Moreover, the viscosity of the solution increases as the polymer network grows, forming a porous structure within the liquid phase (gel). Herein, the size and crosslinking are correlated to the alkoxide precursor and the pH of solution [69]. In the aging process, the condensation proceeds until the precipitation of a gel network, where the structure and the properties of the gel vary continuously. Afterwards, depending on the drying process, the structure of the gel network will be disturbed and it can ~~be~~ generate~~d~~ different ~~kind~~ textures of gels such as xerogel, aerogel and cryogel. For instance, high temperature drying process will result in ~~a~~ low surface area and pore volume (xerogel). On the contrary, supercritical drying forms aerogels, characterized by high pore volume and surface area. In the latter, the gel network is not been affected. In addition, a cryogel is the results of a freeze-drying process, in which the surface area and pore volume ~~are~~ are even lower than for the xerogel.

Finally, thermal calcination is performed in order to remove the residues of water molecules within the structure and it will determine the pore size and density of the perovskites [69].

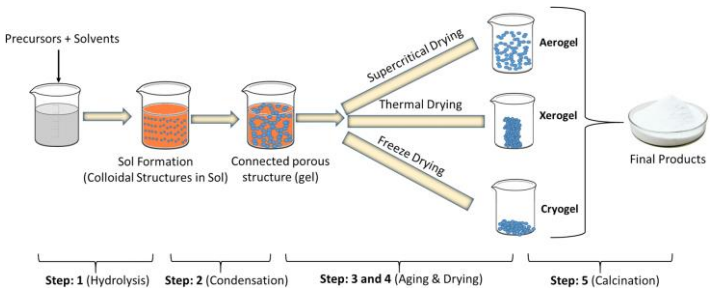

Figure 6. Step-by-step sol-gel method. Reproduced with permission from [69].

Zhao et al. [70] synthesized $Pb_{0.8}Co_{0.2}TiO_3$ thin films with homogeneous microstructure with low porosity by sol-gel method. Starting reagents such as lead acetate, tetra-n-

butyl titanate and cobalt nitrate were dissolved in 2-methoxyethanol. In addition, glacial acetic acid was used as stabilizer. Then, the solutions were deposited on Pt/Ti/SiO_2/Si substrate, dried and annealed at 700ºC in presence of O_2 and N_2 atmosphere. The results demonstrated ca. 200 nm thick perovskite films with a high crystalline structure without the presence of secondary phases. Nevertheless, depending on the annealing atmosphere preferential orientation (100) and oxygen vacancies were detected through XRD analysis and O1s XPS spectra, respectively. Under O_2 and air atmosphere (100) preferential orientation were exhibited, whereas under N_2 atmosphere (100) peak became weaker with random concentration. Nevertheless, the grain sizes of thin films were not affected according to the width of the peaks in the XRD pattern. In the same way, O1s XPS spectra showed oxygen vacancies of the thin film promoted in ~~the~~ N_2 atmosphere, while in ~~the~~ O_2 were inhibited, which altered detrimentally $Pb_{0.8}Co_{0.2}TiO_3$ thin films' ferroelectric properties.

On the other hand, Wan et al [71] synthesized by sol-gel route $Ca_{1-x}Zn_xTiO_3:Eu^{3+}$. The authors studied the effect of Zn incorporation in Ca position of $CaTiO_3:Eu^{3+}$ red phosphor. The starting solution was composed by a stoichiometric amount between $Ca(NO_3)_2{\cdot}4H_2O$, $Zn(NO_3)_2{\cdot}6H_2O$ and $Eu(NO_3)_3$ in ethanol solvent, while the Ti-source $(Ti(OC_4H_9)_4$ was added dropwise under stirring at 95ºC. The transparent gel was dried at 150ºC for 24 h and subsequently was heated at 900ºC in a furnace. The research yielded a significant improvement with the incorporation of Zn compared to pristine $CaTiO_3:Eu^{3+}$. However, the ~~rise~~ increase of Zn could also promote secondary phases such as $ZnTiO_3$ (20% of Zn^{2+}) and Zn_2TiO_4 (30% of Zn^{2+}), which affected the

Formattato: Apice

luminescent properties of the material. The authors concluded that $Ca_{0.9}Zn_{0.1}TiO_3:Eu^{3+}$ with uniform and spherical microstructure achieved an optimal compromise between load amount and luminescent properties, resulting in a three-fold enhancement compared to bare $CaTiO_3$: Eu^{3+}.

Formattato: Apice

Formattato: Apice

Li et al [72] synthesized a (Ba,Sr)TiO_3/TiO_2 heterostructure *via* sol-gel method. The heterostructured powder is composed by microcrystalline $BaTiO_3$ and $SrTiO_3$ cores coated with nano-TiO_2 shells. Commercial $BaTiO_3$ and $SrTiO_3$ were used as perovskite precursors and titanium butoxide ($Ti(OC_4H_9)_4$) was used as Ti-source for the coating. In the synthesis, an optimal mass ratio between titania and core starting materials (1:2:1) was fixed. The annealing temperature was analyzed as an essential parameter that affects the final photocatalytic activity of hydrogen production, due to its effect on the phase composition, crystallinity, porosity and surface area. $BaTiO_3$/TiO_2 heterostructures underwent an annealing process from 400 to 800ºC, whereas $SrTiO_3$/TiO_2 was annealed from 500 to 900ºC. The results of bare TiO_2 showed a conversion of anatase to rutile in TiO_2 (from 500 to 600ºC) as it was expected and a complete transformation at 800ºC. Nevertheless, the (Ba,–Sr)TiO_3/TiO_2 hetero-structured powders exhibited a phase transition in the range of 700-800ºC, but at 800ºC TiO_2 anatase phase is still more than a half. As the annealing temperature increased, the grain size of anatase and rutile increased. However, the authors concluded that $BaTiO_3$ retarded the phase transition of TiO_2 more than $SrTiO_3$.

II.1.5. Chemical Solution Deposition

Chemical Solution Deposition (CSD) is a wet chemical method devoted to the

fabrication of perovskites thin films between 50 and 150 nm in thickness and the optimization of their properties for specific application [73]. It is a low-cost, simple, versatile and scalable technique, useful for studying the effect of chemical substitutions or dopants [74]. It substantially consists in the deposition of a sol on a substrate to form a film. The synthesis method consists in four basic steps: (i) preparation of the precursor solution, which is usually composed by metal-organic compounds (e.g. alkoxides, acetates, or salts) dissolved in a solvent (alcohol or water), (ii) deposition of the coating on substrate by spinning and dipping, (iii) drying process at low temperature (300-400ºC) to decompose organic components and finally (iv) heating treatment with the purpose to crystallize the ceramic material. In addition, to achieve high-purity materials, the substrate plays an important role and it must be appropriately selected according to the crystal structure of the final film [73].

The fabrication of $Bi_{0.5}Na_{0.5}TiO_3$ (BNT) thin films, one of the most promising lead-free TiO_3 – based materials were synthesized by Christensen et al. in citrate and nitrate sol systems, using Titanium isopropoxide as Ti-source [75]. In the former, bismuth citrate was employed as Bi-precursor, whereas $Bi(NO_3)_3 \cdot 5H_2O$ was Bi ions source for the nitrate method. As Na ion sources, NaOH solution and $NaNO_3$ were employed. Moreover, the citrate method was performed in a pH range of 7-9 and NH_4OH solution was applied for this purpose, whereas HNO_3 was added in order to decrease pH within the nitrate method. However, this second system was not successful due to inferior stability and pH of nitrate sol, which could lead to safety risks, equipment failures, and reproducibility limitations. All BNT solutions were deposited on $SrTiO_3$ and thin films

underwent a thermal decomposition and annealing process. The research evidenced the effect of pyrolysis temperature in the formation of BNT pure phase films. The reduction of Bi^{3+} to metallic Bi produced segregation, which led to the formation of a pyrochlore secondary phase. It did not decompose at 400ºC and remained unaltered even after harsher heating treatment (700, 800 and 900ºC), whereas at 550ºC it was pyrolyzed and a single phase BNT was obtained.

$BiFeO_3/BaTiO_3$ (BFO/BTO) multilayer structure was prepared by Sharma et al. [76] *via* chemical solution deposition method. Barium acetate ($Ba(CH_3COO)_2$), bismuth nitrate pentahydrate ($(Bi(NO_3)_3 \cdot 5H_2O$), iron nitrate nonahydrate ($(Fe(NO_3)_3 \cdot 9H_2O$), and titanium n-butoxide ($Ti(C_4H_9O)_4$ were employed as precursors within glacial acetic acid and 2-methoxyethanol as solvents. BFO/BTO multilayer was spin coated on $Pt/SiO_2/Si$ substrate up to 350 nm of thickness (four layers BFO/BTO, 87 nm of thickness/layer). The layers were deposited, heated at 300ºC and underwent 800ºC. The results yielded a polycrystalline structure without secondary phases, owing to optimization of temperature and synthesis preparation. The polycrystallinity is issued by the presence of distorted rhombohedral (R3c) and tetragonal (P4mm) characterized of $BiFeO_3$ and $BaTiO_3$, respectively. Furthermore, Raeder et al. [70] synthesized $BaTiO_3$ thin films with pure phase using CSD method in aqueous medium. The Ba^{2+} and Ti^{4+} aqueous precursor solution was prepared by the addition of $Ba(NO_3)_2$, 4-Isopropoxide, EDTA, ammonia, and citric acid in 1:1:4:8:2 molar ratio, respectively. Thin films underwent a heat treatment of 650ºC, where $BaTiO_3$ crystalline phase showed pure.

II.1.6. Flame-based techniques

Pyrolysis allows the synthesis of a wide range of both inorganic and organic materials, usually with inexpensive apparatus and high reproducibility [77]. In short, it involves the preparation of a solution in which the salts of the precursors are dissolved and then an aerosol is formed in some way, for instance with ultrasound, nebulized through atomizers or nozzles or dispersed within a gas current. The droplets are then combusted at high temperature and the nanoparticles of the selected material are obtained. Post treatments may be required to improve the stability of the particles or to functionalize them, though if the bare oxide is desired, this method allows the one-pot continuous synthesis of nanostructured oxides. Below, a collection of the most used techniques is presented.

II.1.6.1. Flame spray pyrolysis and hydrolysis

The high temperature required to dry out and combust the droplets is reached with a torch, which is usually fed with oxygen or air as oxidizing agent while the fuels are methane or hydrogen [77-81] in the flame hydrolysis asset. By contrast, in the flame spray pyrolysis version of the technique, the fuel is constituted by the organic solvent used to dissolve the precursors of the oxide. The precursor solution is premixed and dispersed with oxygen (50-500 mL/min), then it reaches the flame, where a temperature between 1600-1800 °C is experienced for few milliseconds [80]. Once the solvent is evaporated, the NPs are calcined and the perovskite is formed. In the end, the materials are collected by means of an electrostatic precipitator operating at 10 kV [78, 80, 81] or by a filter. Abe et al. reported the synthesis of two kinds of lanthanum titanate [77,

79] via liquid-feed flame spray pyrolysis (LF-FSP), while Oliva and Fabbrini obtained $SrTiO_3$ [81], $Sr_{1-x}M_xTiO_{3\pm\delta}$ (x = 0 or 0.1; M = K or Gd) [78] and $Sr_{1-x}Ag_xTiO_3$ [80] through flame hydrolysis (FH).

The advantages of the technique are immediately understood. In principle, one single drop turns into a crystal and since the droplets average size belongs to the micrometer the so formed material is nanostructured and shows a narrow size distribution which cannot be replicated with conventional preparation methods as sol-gel. Moreover, the NPs can be synthetized at high temperature without stability issues. Higher stability towards poisoning was also exhibited in some specific applications, e.g., by the possibility to finely disperse protective promoters or allowing sufficient thermal resistance to regenerate the catalyst at sufficiently high temperature preserving catalyst surface area [82]. In addition, the parameters like flow rate, temperature and composition can be changed in order to modify the morphology and the particle size distribution (APs) of the NPs. $SrTiO_3$ [81] and derivatives where found to form spherical aggregates with size of 50-300 nm, whereas the crystallite size was 29-56 nm depending on the kind of precursors employed and operating conditions. Some of the disadvantages are the limited productivity, with a maximum of tens of grams per hour with bench-size apparatus [79].

In addition, the nanoparticles sometimes require a post treatment to increase the stability or the purity of the material. The latter can be carried out by treating the product at high temperature with the proper combination of heating rate and dwell time. Abe et al. [79] found that a thermal treatment is required in order to convert the lanthanum

carbonate and oxides into the desired phase, furthermore, a temperature above 1050 °C causes the conversion of the material. However, although the latter was obtained with the proper morphology (111 plane-type layered perovskite) the post-treatment caused the NPs aggregation into hexagonal particles with a diameter of 200-500 nm and the specific surface area (SSA) decreased from 42 m^2/g to 6.0 and 5.3 m^2/g, respectively, after 3 and 6 hours of heating. On the other hand, some studies [80, 81] reported the synthesis of different kind of strontium titanate that were calcined in air between 850 and 950 °C. It was observed an increased thermal stability with longer residence time in the furnace, despite a loss in the catalytic activity during the flameless combustion of methane.

II.1.6.2. Spray pyrolysis

The principles are the same of the flame spray pyrolysis, but a conventional electric furnace (CEF) replaces the flame. Furthermore, the ultrasonic atomization represents a widely employed technique that forms an aerosol with the precursor solution. Operating frequencies between 1.30 and 1.67 MHz have been reported, with formation of droplets of ca. 6 μm [83-85]. Chou [83] and Li [84] performed the synthesis of $SrTiO_3$ samples with different morphologies by dissolving the precursor into nitric acid solution and by addition of hydroxyl source such as hydrogen peroxide, glycerol or 1,2-propanediol. After the nebulization, the aerosol was taken into a furnace with three zone heated independently and respectively set at 300, 100 and 350 °C, then the NPs were collected through an electrostatic precipitator operating at 16 kV. Anyway, H_2O_2 was found to prevent the formation of a secondary phase when the material was heated at 900°C as

post treatment. In particular the recipe prevented the formation of the (100) plane, which lowers the conductivity of the strontium titanate, so lowering its performance when used as solid electrolyte (e.g. for fuel cells) [83]. On the other hand, the organic alcohol promotes the formation of spherical particles with irregular crystals that show a (111) plane on the surface. In addition, no change was observed in the morphology after sintering at 1500°C for one hour, since hydroxyl groups stabilized the phase formed during the pyrolysis [84].

Lanfredi et al. [85] prepared several strontium titanate based materials where both Ti and Sr were partially substituted by Cu and K, respectively, to obtain a performing catalyst for biodiesel production. The optimization was carried out by tuning the temperature of the CEF (700-900°C), the flow rate of the carries gas (air, 3-6 L/min) and the concentration of the precursor solution (0.025-0.5 M). Overall, it was found that the lower the air flow, the higher is the chance of the NPs to agglomerate into 200-400 nm aggregates. This negative effect can be partially counterbalanced by modifying the composition as in case of $Sr_{0.5}K_{0.5}TiCu_{0.25}O_3$, which was synthetized in form of smooth and spherical particles with few agglomerates only. Despite the precursor solution is still treated with ultrasound (1.6 MHz) and pyrolyzed using CET at 900°C, the product was collected by means of a cyclone. Again, during the post treatment it was observed that the surface conductivity of the NPs is strictly connected to the temperature at which the calcination is performed and the environment too (air vs. mixture of H_2/Ar).

Among the possible setups, Nimmo et al. [86] reported the nebulization of the precursor

solution by using an homemade mixer similar to those adopted in case of flame pyrolysis and that produces the aerosol through the carrier gas flow (15 mL/min of solution and 9 L/min of gas). Then, the particles of solution are carried into a three-meter-long electric furnace that is split into three different zones where the temperature can be independently controlled. In addition, several sampling ports are present on the oven and it allows to understand the effect of the temperature and the residence time on the lead zirconate titanate synthesis.

Singh et al. [87] adopted a totally different route by performing a batch production of calcium titanate where the precursor solution was pretreated for 15 minutes into a microwave oven operating at 2.45 GHz (750W). The material obtained was compared with an untreated sample after both were centrifuged and then pyrolysed into a CET at different temperatures. The latter parameter was found to cause the decomposition of a complex formed with the product and nitrilacetic acid added to the starting solution (540°C), whereas at higher temperature even the calcium carbonate decomposes with formation of the desired titanate. Either the traditional or the MW synthesis route leads to NPs with an irregular elongated shape, despite the particles produced after the MW treatment show a slightly bigger size (86 vs. 75 nm), slightly lower surface area (18 vs. 20 m^2/g) and lower porosity. However, the phase composition as well as the molecular structure was found unaffected by the setup of the pyrolysis.

II.2. Characterization

The interest in titanates and their application in different sectors has grown with the advances in analytical techniques. The most relevant aspects regarding the

characterization of these materials take into consideration their morphology, porosity, elemental composition, thermal stability and thermal behavior, crystalline and structure information, piezoelectric properties and so on. This kind of information become crucial for many reasons: optimizing synthetic methods, guaranteeing highly pure materials, tuning their properties, producing homogenous materials in terms of size and shape, etc. In this section the main analytical techniques used for the characterization of titanates are reported, along with some examples of application. A precise control of the shape and size of titanates is pivotal to develop highly performing materials because the surface morphology affect their photoreactivity [88]. It has been demonstrated that the size and morphology of these materials is strongly dependent not only on the kind of synthetic used methods (hydrothermal reaction, solvothermal reaction, sonochemical reaction, sol-gel reaction, electrospinning and so on), as summarized in **Table 1** and showed in **Figure 7** for $SrTiO_3$, but also on the employed reaction conditions (temperature, pH, etc.) (**Table 2**).

Table 1. Dependence of $SrTiO_3$ morphology and sizes from the synthetic method.

Synthetic method	**Morphology**	**Size (nm)**	**References**
Solid-state reaction	Nanoparticles	110-150	[89]
Polymerised complex	Nanoparticles	25-100	[89]
Solvothermal	Nanoparticles	50-80	[90]
Microwave-assisted hydrothermal	Nanocubes	46-57	[91]
Solvothermal	Nanocubes	~ 20	[92]
Hydrothermal	Nanocubes	20-200	[54]

Solvothermal	Nanocubes, nanospheres and nanoflakes	24-43	[93]
Hydrothermal	Core-~~s~~shell microspheres	~ 700	[94]
Electrospinning	Nanotubes	~ 100	[95]

Scanning Electron Microscopy (SEM), Field Emission Scanning Electron Microscopy (FESEM), Transmission Electron Microscopy (TEM) and High-Resolution Transmission Electron Microscopy (HR-TEM) represent the most suitable techniques for this type of investigations. As it is possible to observe~~d~~, nanospheres, hollow spheres, nanotubes, nanofibers and nanocubes can be easily ~~detected~~ distinguished by these techniques.

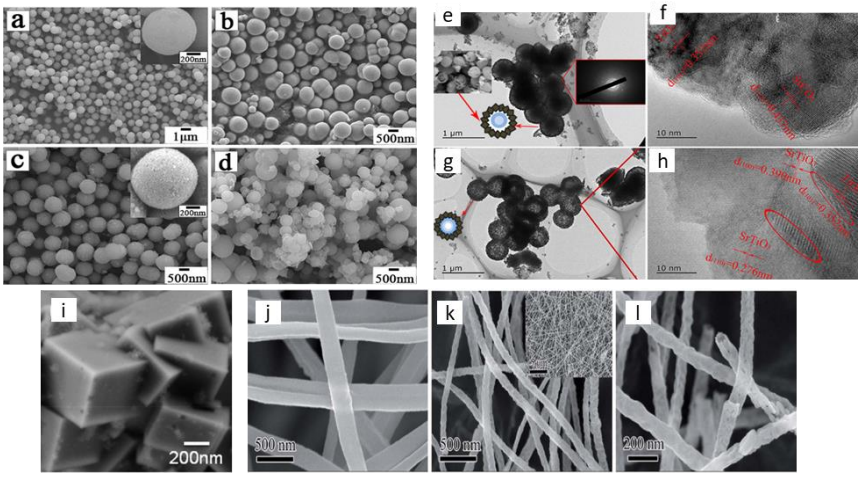

Figure 7. SEM and TEM images of different titanates synthesized by diverse approaches. (a-h) reproduced with permission from Ref [94], (i) Reproduced with permission from [91], (j-l) reproduced with permission from [95].

All these microscopic techniques also allow a fine control of the size variations after specific treatment (e.g., thermal treatment). This is particular important because some properties of titanates (e.g., dielectric and ferroelectric properties) are heavily dependent on the crystal size and as a consequence a precise control becomes fundamental. For example, in the case of ferroelectric properties of $BaTiO_3$ ceramics, it has been demonstrated that the dielectric constant significantly increases when the mean diameter of the particles passes from 10 to 1 μm and then immediately decreases as the particle size ~~goes down~~decreases below 1 μm [96]. Another important parameter whose value is strongly dependent on the size is the Curie temperature (T_c), that is the transition temperature between tetragonal and cubic phases. As reported by Hong and Fang [97], at room temperature the tetragonal distortion and, consequently, the ferroelectricity of $BaTiO_3$ nanowires decreases with decreasing particle sizes. Similar investigations carried out on $BaTiO_3$ nanoparticles demonstrated that the critical dimension below which the room-temperature ferroelectricity disappears is strongly dependent on the synthetic method employed, but, in general, is in the range 10-100 nm [98].

In addition to dielectric constant and Curie temperature (T_c), many other parameters are affect from the size and shape of titanates, such as piezoelectric constant, planar electromechanical coupling factor and remanent polarization that are higher for sintered $(Bi_{0.5}Na_{0.5})TiO_3$ nanofibers than for the corresponding nancubes [99].

The activity of titanates is also influenced by their crystal phase. It is well known that crystalline $BaTiO_3$ exists in various crystalline forms. The tetragonal ferroelectric form

is characterized by high dielectric constant at a range temperature of 0-130°C, above which it is converted into a paraelectric cubic structure [100]. The conversion of tetragonal $BaTiO_3$ to the haxagonal ploymorph can be carried out by the effect of the sintering temperatures and processing condition and x-rays powder diffraction (XRPD) is a powerful technique to follow the variation of the crystalline structure of titanates on the basis of their composition (**Figure 7**). **Table 2** summarizes the crystallographic parameters of both tetragonal and hexagonal structures, demonstrating that the hexagonal $BaTiO_3$ shows larger unit cell and volume than the corresponding tetragonal one [101]. **Table 3.** reports the application of crystallites sizes of different $SrTiO_3$ samples synthesized by an aerogel procedure (AP) and prepared in different alcohol–toluene mixtures, along with a commercial $SrTiO_3$ for comparison [102].

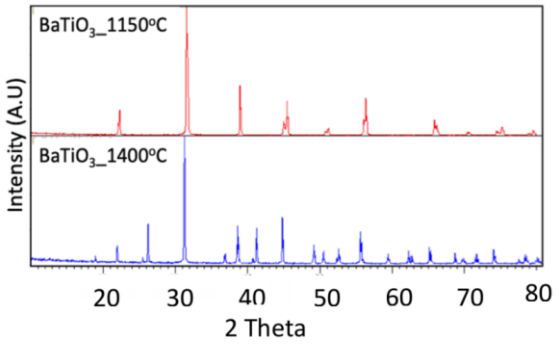

Figure 7. XRD patterns of (down) hexagonal $BaTiO_3$ sintered at 1400 °C for 12 hours, (up) tetragonal $BaTiO_3$ sintered at 1150 °C for 6 hours. Reproduced with permission from Ref [101].

Table 2. crystallographic parameters of both tetragonal and hexagonal $BaTiO_3$.

Form	a (Å)	b (Å)	c (Å)	V ($10^6 pm^3$)
Tetragonal	3.9990	3.9990	4.0220	64.32
hexagonal	5.7240	5.7240	13.9650	396.25

Table 3. average crystallite size of different $SrTiO_3$ samples obtained from XRPD.

Type of $SrTiO_3$	**Average crystallite sizes (nm)**
Methanol-$SrTiO_3$	25
Ethanol-$SrTiO_3$	8
Isopropanol-$SrTiO_3$	20
Commercial-$SrTiO_3$	145
Nanosized-commercial-$SrTiO_3$	25

Information on the elemental composition can be obtained by EDS (Energy-dispersive X-ray spectroscopy), a useful technique usually and extensively employed. Moreover, coupled with SEM, it allows the elemental composition for a particular area of the material of interest. By way of example, in **Figure 8** the elemental composition $Na_{0.5}Bi_{0.5}TiO_3$ (NBT) [103] materials obtained by EDS analysis is reported.

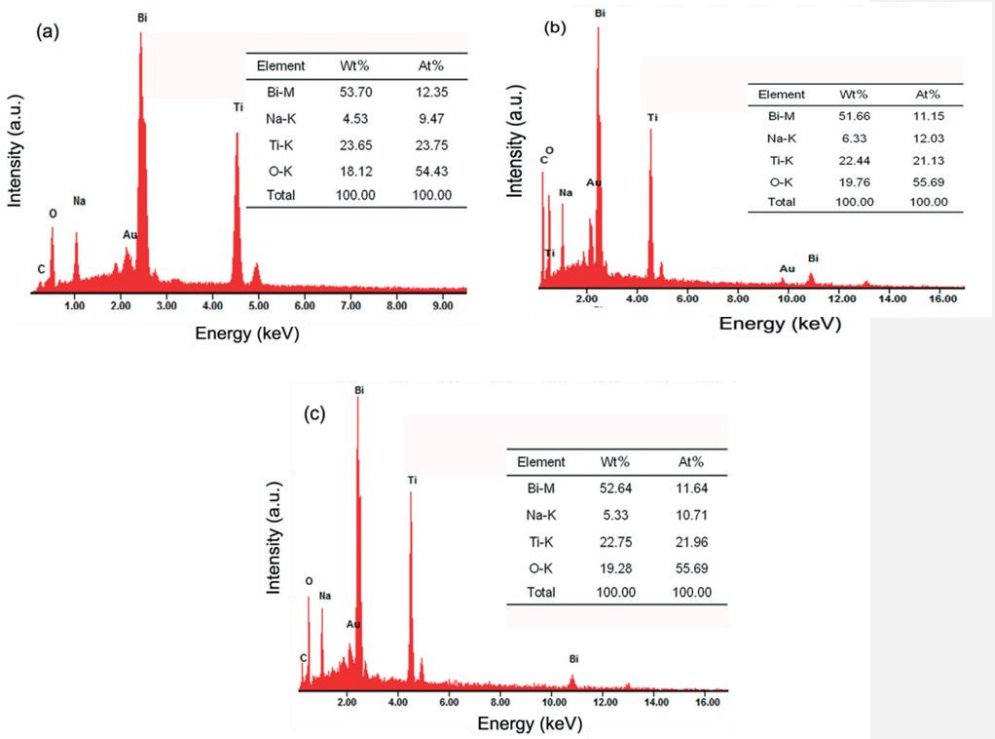

Figure 8. EDS analysis of NBT spherical agglomerates (a), nanowires (b) and microcubes (c).

However, EDS is not the unique technique able to give information on the elemental composition of materials. In fact, qualitative and quantitative information can be also obtained by X-ray photoelectron spectroscopy (XPS) that also allows the determination of the chemical state and crystalline phase of the elements constituting the surface (layer with several tens nm in thickness) of the material under investigation. By this technique, a first survey spectrum is generally acquired, that measures the amount of all detectable elements and allows to set up subsequent high-resolution XPS spectra acquisition.

Numerous studies have been performed by XPS to analyze the surface chemistry and surface phases of a variety of commercial and laboratory synthesized titanates [104-106]. XPS spectra permit the investigation of the chemical state and bonding of the elements. XPS represents also a powerful tool for the identification and quantification of the presence of impurities, such as carbonates, as demonstrated by Viviani *et al*. that identified the presence of $BaCO_3$ in $Ba_{(1-x)}Sr_xTiO_3$ powders also on the basis of the results of the XPS spectra in C1s and O1s zones (**Figure 9**) [107].

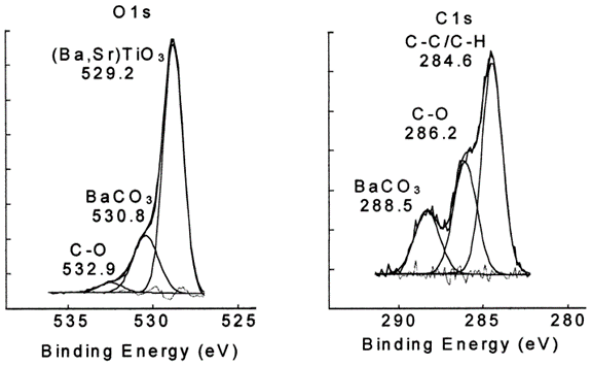

Figure 9. XPS spectra in C1s and O1s zones of $Ba_{(1-x)}Sr_xTiO_3$ powders.

Structural evolution in perovskites can be easily investigated by Raman spectroscopy on the basis of the presence of proper Raman-active modes. Even if the use of Raman spectroscopy for the investigation of phase transitions is less common than other techniques, an extensive literature exists. **Figure 10** shows the temperature evolution of the Raman spectra for undoped $BaTiO_3$ from room temperature to 300 °C [108].

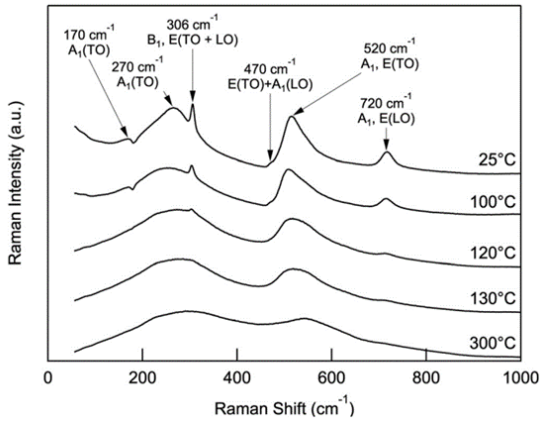

Figure 10. Temperature evolution of the Raman spectra for undoped $BaTiO_3$ from room temperature to 300 °C. Reproduced with permission from [108].

Briefly, the bands at about170 and 306 cm^{-1} and the asymmetric broader bands at 270, 520, and 720 cm^{-1} in the spectrum at room temperature are characteristic of the tetragonal phase. Increasing the temperature, all these bands become less intense, because of the disorder of Ti displacements in the octahedral [108].

This techniques has proved particularly useful for the determination of $(1-x)Na_{½}Bi_{½}TiO_{3-x}BaTiO_3$ (NBT–xBT) system composition [109]. These materials exhibit excellent piezoelectric properties at the rhombohedral-tetragonal morphotropic phase boundary (MPB) and represent good alternatives to replace lead containing piezoelectric ceramics. If compared to traditional lead-based materials, the diffuse phase transition in NBT is associated with global structural changes [110, 111]. Systems characterized by a low BT content become tetragonal because of the rather large lattice distortion of BT compared to the rhombohedral distortion in NBT. Route *et al.*

demonstrated ~~as~~ how Raman spectroscopy allows to detect these structural modifications [109].

Paramagnetic defects and defect complexes in polycrystalline titanates can be identified by electron paramagnetic resonance (EPR). **Table 4** summarizes the g-value (a constant of proportionality, whose value is the property of the electron in a certain environment) for several paramagnetic centers in $BaTiO_3$ [112].

Table 4. g-values of several paramagnetic centers in $BaTiO_3$ (Vo= oxygen vacancy, V'_{Ba}= ionized Ba vacancy).

g-value	Defect center	Temperature range (K)	References
1.907–1.936	Ti^{3+}	4.2-80	[112]
1.899–1.938	Ti^{3+}-Vo-K(Na)	4.2-80	[112, 113]
1.920–1.937	Ti^{3+}-Vo	10-80	[112, 113]
1.963–1.974	Ti^{3+}	300-423	[114]
	Ti^{3+}-Vo	200-400	[114, 115]
	Ti^{3+}-Ln^{3+}	300-400	[116]
	Cr^{3+}	77-500	[117]
1.997–2.005	V'_{Ba}	70-423	[114, 115]
	V'_{Ba}-Vo	77-500	[117, 118]
	Fe^{3+}	300-420	[112]

Numerous perovskites show ferroelectric properties. This means that they have a spontaneous electric polarization that can be reversed by the application of an external electric field. The generation of a surface charge in response to the application of an external stress to a material is called piezoelectricity, as already defined. BTO nanomaterials characterized by an elongated shape, such as nanofibers, nanotubes and nanoribbons, have exhibited extraordinarily high ferroelectric properties, if compared to traditional materials (e.g., ZnO nanocrystals) [119, 120]. Zhuang *et al*. used PFM to characterize BTO nanofibers in terms of ferroelectric and piezoelectric properties

Formattato: Pedice
Formattato: Apice
Formattato: Apice
Formattato: Pedice
Formattato: Pedice

(Figure 10) [121]. The different polarization directions can be obtained by the different contrast of various areas in the phase images observed in Figure 10,b, where the bright and dark regions correspond to the domains oriented upwards and backwards directions, respectively. In Figure 10,c, it is reported the amplitude and phase versus applied voltage loops (-30 to 30 V). The variation of amplitude corresponds to the change of strain under external electric field. At 30 V the hysteresis loop reaches a complete saturation.

In this condition, all the dipoles could be aligned along the direction of external electric field and form single domain. By all these results the piezoelectric coefficient or piezoelectric modulus (d_{33}), that quantifies the volume change of a piezoelectric material exposed to an electric field, or its polarization when a stress is applied, was calculated at 30 V and resulted to be 20 pm/V. If compared to bulk BTO materials for which d_{33} is 85 pC/N, this value is extraordinarily high and can be attributed to the size effect of BTO nanofiber [122].

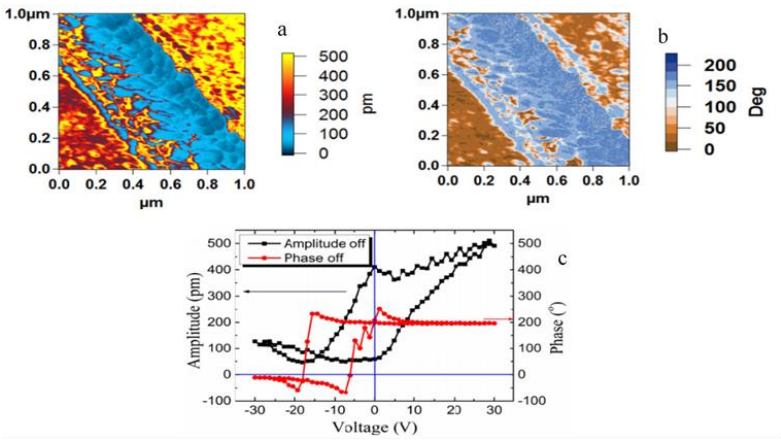

Figure 10. PFM images of a single BTO nanofiber obtained at 750°C for 2 h; (a)

vertical amplitude image; (b) vertical phase image, the presence of ferroelectric domains in the entire fiber is obvious; (c) amplitude and phase versus voltage loops, the loops indicate the domain switching and piezoelectric properties of a single BTO nanofiber.

III. Application of $XTiO_3$ perovskite-type oxides

III.1. Environmental remediation

$XTiO_3$ piezoelectric based materials such as $BaTiO_3$, $SrTiO_3$ and $CaTiO_3$ have been widely used for the removal of various compounds from the environment including organic/inorganic pollutants and bacteria. In this section the mechanistic pathways in $XTiO_3$ based materials systems for the generation of redox species will be addressed. Currently, such materials could be activated via the application of different driving forces such as ultrasound, heating or light irradiation. The relationship between the characteristics of $XTiO_3$ based materials and their activity will be discussed. On top of that, advances in the enhancement of the activity of these catalysts via the doping or combination with other materials to get better piezo- or/and photo-catalytic performances will be reviewed.

III.1.1. Piezocatalytic activity assisted by ultrasound or heat

Piezoelectric materials have the advantages to create electric charges under mechanical stress. These materials received great attention from both the scientific and industrial communities for many piezoelectric applications [123-129]. Of these materials, polycrystalline $BaTiO_3$ has been considered as one of the most efficient piezoelectric

material during the 1950s [130-134]. Later, lead zirconate titanate-based materials (PZT) with greater piezoelectric activity have been developed and applied in many areas [134-139]. However, due to the toxicity of Pb in PZT systems, the application of Pb based materials is very limited especially for environmental remediation. Therefore, the scientific community nowadays is addressing the development of lead-free piezoelectric materials to avoid the toxicity issues of PZT [140-146]. Over the last decade, many efforts have been done to develop lead-free $XTiO_3$ based materials via the modification with co-cations or its combination with other materials for various applications [19, 132, 147-151].

The formation of ROSs for the oxidation of organic pollutants on the surface of piezocatalyst by ultrasonic driven force is due to the generation of strain-induced electric charges on the catalyst surface as a result of the deformation and accumulation of charges. Hence, the piezocatalytic activity for the oxidation of organic pollutants depends on the ultrasonic vibration potential applied to the catalyst. Many reports mentioned that an enhanced piezocatalytic activity under ultrasonic vibration is obtained in materials with better piezoelectric potential along the polar axis [152]. The acoustic pressure will fluctuate in the form of wave in adjacent surrounding of piezocatalytic materials in the order of 10^5–10^6 Pa. Furthermore, the shock effect resulting from collapse of cavitation bubble induces a mechanical deformation and piezoelectric effect on the surface of the piezo-catalyst. The piezoelectric coefficient (d_{33}) is proportional to the spontaneous polarization (Ps) [153, 154] as follows $d_{33} = 2\varepsilon_{33}\varepsilon_0 k_{33} p_s$. Where, ε_{33} is the dielectric constant, ε_0 is the vacuum dielectric constant,

and $k_{33}$is the electrostriction coefficient.

On top to the structure and characteristics of piezo catalysts, the chemical environment can affect the polarization orientation and, therefore, results in different surface interactions with the species present in the medium [155]. The oxygen vacancies can affect the polarization orientation of piezo-materials [156, 157]. The wettability and water interaction with the surface of piezo-catalysts have a strong influence on the catalytic activity as well as on the formation of ROSs by piezo catalysts under light or/and under ultrasound. Geneste et al. [158] reported that water molecules exhibit strong interaction energies with $BaTiO_3$ (001) surface, while a high hydroxylation was detected on the surface. In addition, it was found that the bulk polarization was preferentially oriented parallel to the surface polarization associated to the hydroxyl groups. In terms of $BaTiO_3$ without any ultrasonic vibration, the conduction and valence bands are able thermodynamically to reduce and oxidize O_2 and HO^- respectively into $\cdot O_2^-$ and ·OH as shown in **Figure 11.a** [152]. However, because of the smaller yield of free electrons on the surface at thermal equilibrium, such free electrons will be exhausted as soon as the catalyst is immersed in the aqueous medium, leading to suppress the formation of ROSs species. Thus, no catalytic activity can be found without provoking the surface of piezocatalytic crystals via an external driving energy. The application of ultrasound driving force leads to form a piezoelectric polarization (Ppz) state on the $BaTiO_3$ surface, wherein, a high yield of separated electrons and positive holes are formed in the opposite direction on the surface of $BaTiO_3$ and such a phenomenon leads to tilt both the valence and conduction bands of the catalyst with a

Commentato [IR5]:

Commentato [IR6]: check

slope proportional to the piezoelectric potential, as schematized in **Figure 11.b**. At a potential equilibrium, the accumulated screen charges will take place (**Figure 11.c**), which in turn limits the redox reactions and the generation of ROSs. Afterwards, the potential equilibrium can be broken via the diminution in polarization upon dropping pressure, resulting in reversed charge transfer as shown in **Figure 11.d**, accompanied with novel redox reactions.

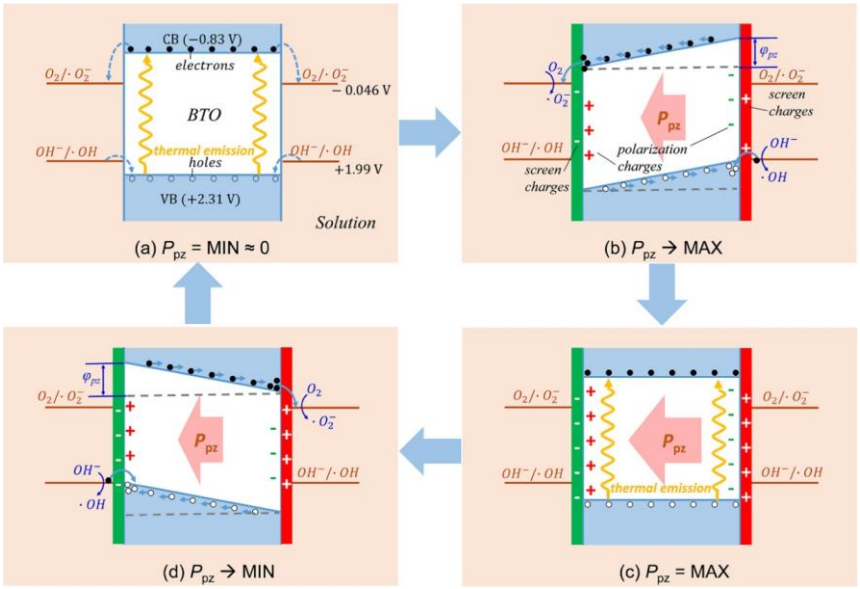

Figure 11. Piezocatalytic mechanistic pathways on the surface of $BaTiO_3$ under ultrasonic driving force. Reproduced with permission from [152].

The possible reactions for the generation of ROSs that could take place on the surface of piezo-catalysts under ultrasound are the following:

$$Piezo_{Catalyst} \xrightarrow{Ultrasonic\ vibration} Piezo_{Catalyst}(h^+ + e^-) \quad (1)$$

$$e^- + O_2 \rightarrow O^{\bullet}{}_2^- \quad (2)$$

$$4e^- + 4H_2O \rightarrow 4OH^- + 4H^{\bullet} \quad (3)$$

$$4H^{\bullet} \rightarrow 2H_2 \quad (4)$$

$$h^+ + OH^- \rightarrow OH^{\bullet} \quad (5)$$

$$Organic\ pollutants \xrightarrow{(ROSs:\ OH^{\bullet};\ O^{\bullet}{}_2^-;\ h^+ \ldots etc)} products\ (H_2O + CO_2) \quad (6)$$

The structure of $BaTiO_3$ is an important key and affects significantly the piezo catalytic degradation process. For example, Huang et al. [159] tested the cubic and tetragonal phases of $BaTiO_3$ towards the oxidation of MO (10^{-5}M) under ultrasonic irradiation (40 kHz, 300 W), and it was found that the cubic form was almost inactive within 60 min of ultrasonic irradiation, while the tetragonal form exhibited a degradation rate of 45% within the same period of irradiation time. On the other hand, the facet engineering is an efficient approach to the piezocatalytic activity of $XTiO_3$ catalysts, Ling et al. [160] fabricated $SrTiO_3$ nanocrystals with different facets including exposed (0 0 1), dominant (1 1 0) and co-exposed (0 0 1) and (1 1 0). It was found that the co-exposed facet based $SrTiO_3$ was the most efficient for the generation of ROSs ($\cdot O_2^-$, $\cdot OH$) under ultrasonic vibration for the oxidation of RhB.

The doping of $XTiO_3$ is a successful approach to enhance the piezocatalytic performance for organic pollutants oxidation. Liu *et al.* [16] have studied the piezocatalytic activity of $(Bi_{1/2}Na_{1/2})TiO_3$ under ultrasounds (100 W, 40 kHz) as a driving force for the oxidation of different dyes in water. SEM images (**Figure 12.a**) showed nanofibers of $(Bi_{1/2}Na_{1/2})TiO_3$ which exhibited a mean diameter of 163 nm. In

Figure 12.b, the decoloration of Acid Orange 7 with time is showed as well as the change of the color of $(Bi_{1/2}Na_{1/2})TiO_3$ after the reaction. The authors reported that the negatively charged molecules (RhB and MB) are likely to be electrostatically adsorbed on the positive surface and degraded by the ROSs produced on the surface of catalyst, while a positive side trends to trap the negatively charged dyes, as shown in Figure 12.c. Scavenging tests showed that the in-situ produced $^{\bullet}OH$ and $^{\bullet}O_2^-$ species are more effective for the degradation process compared to direct oxidation by h^+.

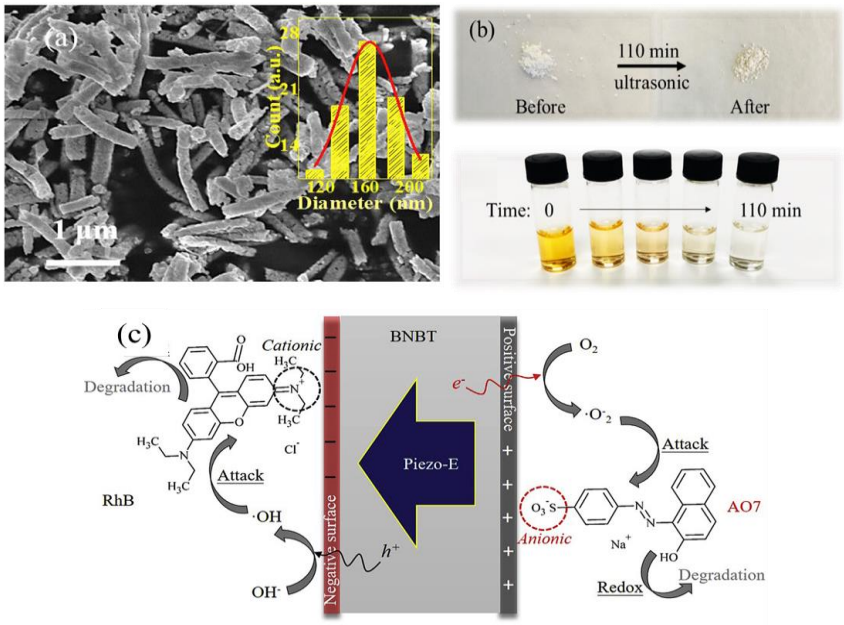

Figure 12. (a): SEM image of $(Bi_{1/2}Na_{1/2})TiO_3$ nanofibers, (b): Piezocatalytic decoloration of Acid Orange by $(Bi_{1/2}Na_{1/2})TiO_3$ assisted by ultrasonic, (c): Suggested mechanistic pathways for the degradation of cationic and anionic dyes. Reproduced with permission from [16].

$XTiO_3$ has been combined with different oxides for synergistic effects as well as to get multifunction smart based catalysts for environmental remediation. Kakekhani et al. [161] designed and studied the characteristics of CrO_2@$PbTiO_3$ towards the abatement of NO_x and CO. The authors reported that the combination of CrO_2 and $PbTiO_3$ brings a multifunction composite with a switchable property between fast interaction with the pollutant species which enhances the catalytic activity, and fast desorption of the final products to get a clean and active surface for further reactions.

As shown in **Figure 13.a**, the polarization of surface of CrO_2@$PbTiO_3$ can be switched repeatedly between a reductive polarization ($P > 0$) and oxidative polarization ($P < 0$). In terms of NO_x conversion, **Figure 13.b** shows the mechanism of the reduction of NO_x into N_2 and O_2 when the surface is reductive, and the desorption of N_2 when the surface turns to positive, while simultaneously the CrO_2@$PbTiO_3$ oxidizes CO to CO_2.

Formattato: Pedice

Formattato: Pedice

Formattato: Pedice

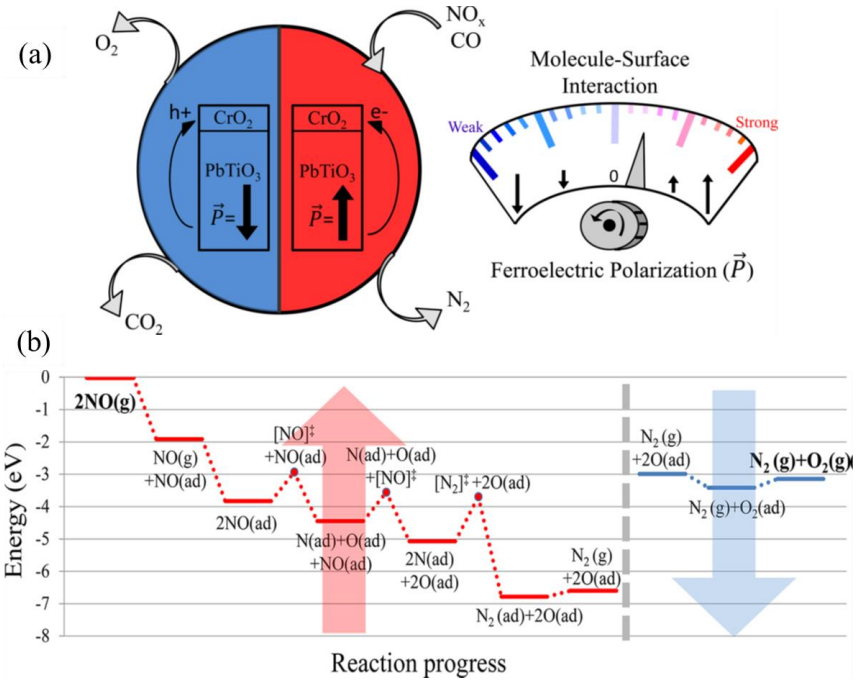

Figure 13. (a): CrO_2@$PbTiO_3$ with switchable polarization surface for catalytic conversion of NO_x and CO. (b): mechanistic pathways of NO_x conversion followed by N_2 desorption on the surface of CrO_2@$PbTiO_3$. Reproduced with permission from [161].

Formattato: Pedice

Formattato: Pedice

In place of ultrasound as a driving force to excite $XTiO_3$ based piezo catalysts, the thermal excitation has been also reported. Benke et al. [162] have studied the mechanistic pathways of ROSs generation on pyroelectric Pd doped $BaTiO_3$ system under heating. In such a process, pyroelectric-band tilting in $BaTiO_3$ under heating ($\Delta T \leq 50$ K) takes place as a first step. Afterwards, electrons move from $BaTiO_3$ to Pd nanoparticles leaving separated holes in the valence band of $BaTiO_3$ as shown in **Figure 14**. Such positive holes in the valence band react with OH^- to produce $^{\cdot}OH$, while electrons accumulated on Pd nanoparticles reduce O_2 to $^{\cdot-}O_2$. The same experiment was

carried out without heating and no significant ROSs were produced, confirming the thermal effect as a driving force for the excitation $BaTiO_3$ and charges transfer.

Wu et al. [163] have also studied the oxidation of organic pollutants using $BaTiO_3$, wherein the pyroelectric catalytic activity was assisted by temperature variation. The authors reported that $BaTiO_3$ nanowires with elongated polar axis, due to the larger pyroelectric potential, exhibited a better performance compared to equiaxial $BaTiO_3$. The results also showed that the degradation of RhB by $BaTiO_3$ takes place only during cold-hot cycles, wherein, the temperature of the medium is varied continuously between 25 and 45^oC. However, the oxidation performances were negligible under constant temperature (25 or 45^oC). An increase in the temperature of the medium induces opposite polarization charges on the polarity of $BaTiO_3$, while both the valence and conduction bands are tilted with a slope proportional to the polarization density of $BaTiO_3$. Electron/hole pairs will be generated for redox reactions. Afterwards, a new balance will be re-established at higher electric field, which in turn limits the redox reactions on the surface of $BaTiO_3$. Therefore, a further decrease in the temperature will break such an equilibrium and will reverse the slope and the charge transfer direction, and thus novel redox reactions may come into action. It was reported that the scavenging of positive holes mostly suppressed the activity, suggesting the high potential of h^+ for the direct oxidation or as a source of ROSs generation. However, unlike the high oxidation rate of RhB, it was found a lower oxidation of negatively charged MO dye molecules.

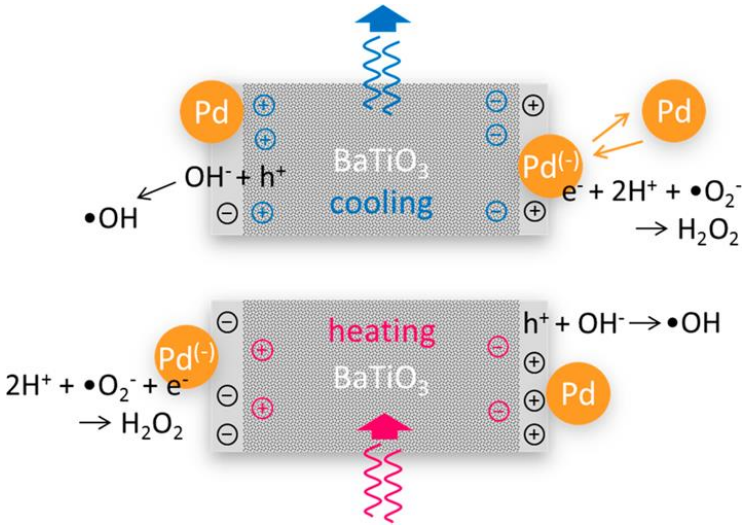

Figure 14. Thermal assisted generation of ROSs on pyroelectric Pd-$BaTiO_3$ catalyst, reproduced with permission from [162].

III.1.2. Photocatalytic activity of $XTiO_3$ based materials

$XTiO_3$ based materials can be photocatalytically activated via the irradiation of the catalyst surface with light irradiation of energy equal or greater than the band gap of the catalyst, forming redox species that may be used for environmental remediation. Usually, bare $XTiO_3$ catalysts have a wide band gap, which limits the use of solar radiation. Many research studies have been carried out to improve the effectiveness of these materials under visible light by different approaches. The synthesis conditions such as the temperature and solvents can affect significantly both the structural phases and the optical and physical features. For example, some studies reported that the tetragonal phase of $BaTiO_3$ exhibits a higher catalytic activity compared to cubic phase [159, 164]. On the other hand, Bantawal et al. [165] reported that the spheric shape of

$SrTiO_3$ was more efficient that the cubic one, in which, the form of $SrTiO_3$ particles was controlled by changing the solvent.

Doping or fabrication of heterojunction systems were the most popular reported strategies to improve visible light harvesting. Doping can decrease the band gap of $XTiO_3$ catalysts. Unlike conventional semiconductors, piezoelectric based semiconductors could improve the transfer of the charges due the presence of charge defects on their surface as a result of piezoelectric property, especially in heterojunction systems [166-168]. A study conducted by Yoshimatsu et al. [169] showed that the optical and photocatalytic performance in $XTiO_3$ (X = Mn, Fe, Co, and Ni) films follows this order: $NiTiO_3 > CoTiO_3 > FeTiO_3 \gg MnTiO_3$, which is due to the different electronic structures as a function of the metal cation incorporated in the $XTiO_3$ structure.

Zhou et al. [170] have investigated the effect of metal doping (such as Fe, Mn and Co) on the optical and structural characteristics of $SrTiO_3$ and $NaTiO_3$. The substitution of Sr ion by metal heteroions alters the structure. In bare $SrTiO_3$, the calculated bond lengths of Sr-O and Sr-Ti were 2.792 and 3.419 Å, respectively. M-O, M-Ti bond lengths are slightly shorter (e.g., for the case of M = Mn, 2.766 and 2.768 Å, respectively).

The values of conduction and valence bands obtained from experimental data are schematized in **Figure 15.a** for doped $SrTiO_3$ and $NaTiO_3$ samples. Compared to bare $SrTiO_3$ and $NaTiO_3$, a significant reduction in the band gaps was found. For example, the band gaps were reduced by 1.1 and 2.07 eV in the cases of Fe-doped $SrTiO_3$ and

Fe-doped $NaTiO_3$ compared to bare samples.

In $SrTiO_3$ systems, Irie et al. [171], reported that the doped $(Pb_xSr_{1-x})TiO_3$ (x = 0.01-0.3) showed an enhanced visible response as a function of x. Suresh et al. [172] also investigated the effect of Ca content in $Ba_{1-x}Ca_xTiO_3$ materials, finding that, with a ratio of x = 0.3, the photocatalytic efficiency for 2-propanol decomposition was significantly enhanced due to the high polarization. Additionally, the phase transition temperature of the composite decreased. The band gap was reduced from 3.2 to 2.2 eV after the introduction of Ca in $BaTiO_3$, resulting in enhanced Methyl orange oxidation under visible light from 30 to 65%. Kushwaha et al. [173] reported the photocatalytic activity of Li-Doped $Bi_{0.5}Na_{0.45}K_{0.5}TiO_3$–$BaTiO_3$ for the degradation of Methyl orange and Estriol under visible light (λ> 420 nm). In dark, the photocatalyst does not show a sufficient oxidation activity. However, under visible light, a significant degradation was detected for both organic pollutants, wherein, around 75% of 10 ppm of methyl orange and 84% of 1 ppm of estriol were degraded within 150 and 30 min, respectively, in the presence of 1 g/L of photocatalyst. The photoelectrochemical analysis showed that the photocurrent responses under visible light were enhanced three times compared to dark conditions, which confirms the photogeneration of electron/hole charges. The scavenging of ROSs tests showed that the $^{-}\cdot O_2$ and h^+ have the potential oxidative effects compared to ·OH radicals. Xiao et al. [174] have fabricated (N^{3-}, Ni^{2+})-codoped $(Na_{0.5}Bi_{0.5})TiO_3-BaTiO_3$ with lower band gap of 2.06 eV for enhanced visible light oxidation of organic pollutants in water such as RhB dye and dibenzothiophene from a model oil. The host material $(Na_{0.5}Bi_{0.5})TiO_3 - BaTiO_3$ exhibits a 34% of RhB

Commentato [IR7]: not uniform notation along the text

degradation under UV-Vis light. For the purpose of comparison, the authors have coated the host material with AgNPs 1.5 wt % which improved the oxidation rate to 56.4% within 80 min. However, interestingly the co-doping of $(Na_{0.5}Bi_{0.5})TiO_3-BaTiO_3$ with N^{3-} and Ni^{2+} decreased the band gap and improved the photocatalytic activity compared to Ag coated photocatalysts. With the N^{3-} and Ni^{2+} doped material, the photocatalytic activity was enhanced up to 92.4% within 80 min. In terms of photocatalytic oxidative desulfurization of dibenzothiophene, the doped $(Na_{0.5}Bi_{0.5})TiO_3-BaTiO_3$ showed ca. 90% degradation within 150 min, while less than 10% degradation resulted with the undoped catalyst. In addition, the authors reported that the single doping by N^{3-} or Ni^{2+} was not effective compared to co-doping. ROSs quenching tests showed that ·OH species were the most effective for the oxidation of dibenzothiophene compared to h^+ and $\cdot^{-}O_2$.

Song et al. [175] reported that the combination of $SrTiO_3$ and CeO_2 improved the photocatalytic efficiency four times compared to bare $SrTiO_3$ under UV light towards the oxidation of Direct Red 23. An internal electric field is formed at the heterojunction, which improves the generation of separated redox charges. Rioult et al. [176] reported that the photocurrent responses were improved twice for the $BaTiO_3$/Nb:$SrTiO_3$ system compared to bare $BaTiO_3$, due to the separation of photo-generated charges promoted by the internal electric field. Li et al. [177] tested the photocatalytic efficiencies of $PbTiO_3/TiO_2$ core/shell structure prepared by sol-gel and mechanically made $PbTiO_3/TiO_2$ towards the oxidation of methylene blue under visible light. It was obtained that $PbTiO_3/TiO_2$ core/shell structure sample exhibits several times better

efficiency than that of the mechanical mixture, reflecting the importance of charge transfer, which takes place at the interface between $PbTiO_3$ and TiO_2. Usually charge transfer is rare in mechanically made heterojunctions. Another example of $XTiO_3$ heterojunction systems is showed in **Figure 15.b,c.** The authors [178] investigated the effect of the presence of different ratios of $SrTiO_3$ (0.5, 1 and 2%) in $BiVO_3$ for the photocatalytic oxidation of sulfamethoxazole under Xe lamp irradiation as a solar simulator. The oxidation performance was improved when $SrTiO_3$ was introduced in $BiVO_3$, wherein, the highest oxidation rate of sulfamethoxazole was found with $BiVO_3/SrTiO_3$(1 %) at 91 % within 60 min, while the bare $BiVO_3$ showed a conversion of 54%, only.

Kong et al. [179] fabricated a multi-heterojunction based on $TiO_2/SrTiO_3/g\text{-}C_3N_4$ for toluene oxidation under visible light as shown in **Figure 15.d,e**. It was found that this multi-heterojunction composite showed 27 times better activity than TiO_2, 13.5 times than $SrTiO_3$ and 4.9 times than $g\text{-}C_3N_4$. In addition, the multi-heterojunction photocatalyst exhibits better photocatalytic performance than $TiO_2/SrTiO_3$. The main reasons behind this high photoactivity were the improved visible light responses and the transfer of photoinduced charges at the interface of $TiO_2/SrTiO_3/g\text{-}C_3N_4$, which boosts the separation of redox charges as well as the formation of higher yield of ROSs.

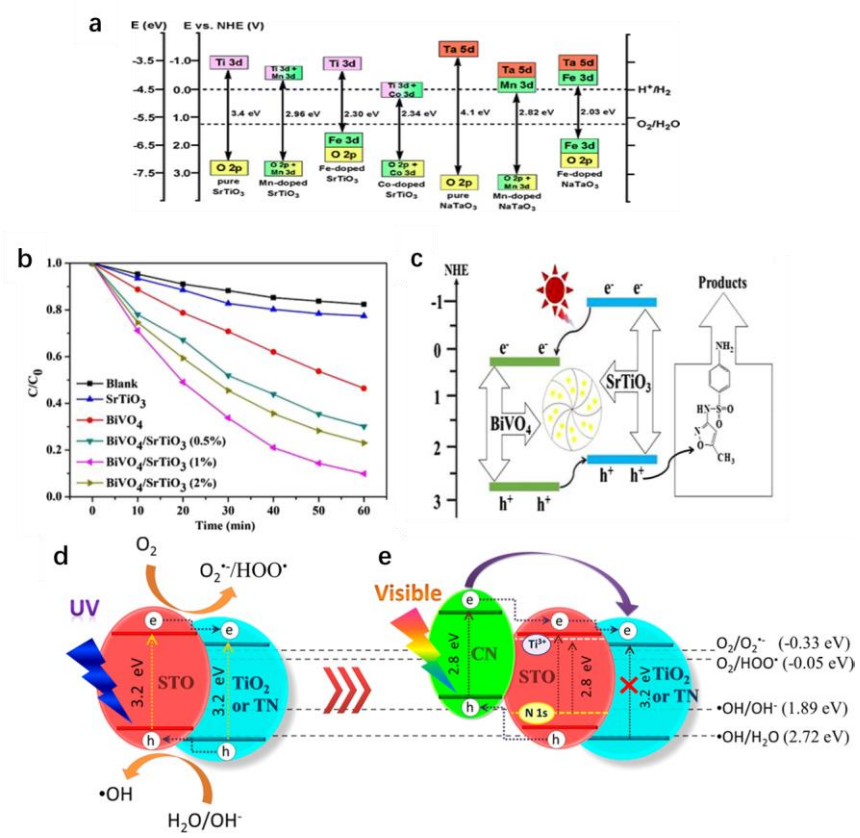

Figure 15. (a) Effect of metal doping (Mn, Fe and Co) on the optical band gaps of $SrTiO_3$ and $NaTiO_3$, reproduced with permission from [170]. (b) Photocatalytic oxidation of sulfamethoxazole using a solar simulator for $BiVO_3$, $SrTiO_3$ and $BiVO_3/SrTiO_3$ photocatalysts. (c) Band levels and photoinduced charges transfer in $BiVO_3/SrTiO_3$ system for enhanced photocatalytic oxidation, (b) and (c) reproduced with permission from [178]. (d) and (e) Diagram for the band levels for $TiO_2/SrTiO_3$ and $TiO_2/SrTiO_3$/g-C_3N_4 systems, the optical and transfer of photoproduced charges to enhance toluene gas oxidation under UV or visible light. Reproduced with permission from [179].

Besides the photocatalytic oxidation of organic pollutants by $XTiO_3$ based catalysts,

the reduction of metals by such materials has been reported. Zhen et al. [180] have used $PbTiO_3$ nanoplates for the photocatalytic deposition of noble metals and metal oxides under light irradiation. Pt was deposited by photocatalytic reduction in the form of nanoparticles on the (001) facets of $PbTiO_3$. Simultaneously, Mn was deposited via photooxidation reaction in the form of MnOx as shown in **Figure 16**.

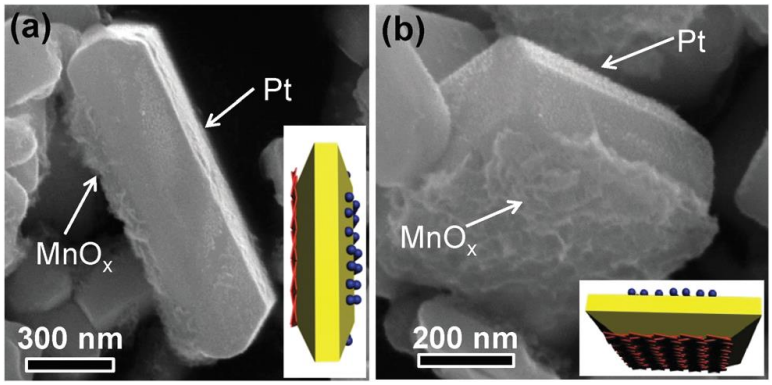

Figure 16. Photocatalytic deposition of Pt nanoparticles and MnO_x on the surface of $PbTiO_3$, reproduced with permission from [180].

Formattato: Pedice

The combination of $XTiO_3$ catalysts with carbonaceous materials leads also to enhance the photocatalytic activity through the decrease of band gap or/and decrease the recombination of electron/hole pairs. In addition, the surface area would be enhanced in $XTiO_3$/carbonaceous material systems resulting in better contact between the pollutants and the photoproduced ROSs via the so-called Adsorb and Shuttle mechanistic process which focuses on the combination of highly adsorbing domains to intensify the accumulation of contaminants near photoactive sites for further oxidation [181].

The synthesis of hybrid materials containing $SrTiO_3$ and graphene resulted in the formation of Sr−C bonds which boost the photocatalytic degradation of MB under visible light due to the transfer of photoinduced charges through this bond into the conductive graphene material [182]. Similar tendency was reported on TiO_2 combined with carbonaceous biomass [183, 184].

Such a combination also leads to enhanced energy density, dielectric constant, breakdown strength and piezoelectric properties [185, 186]. Baran et al. reported that the electronic and transport properties were significantly changed in hybrid $SrTiO_3$-graphene and carbon nanoribbon interfaces [187]. Sobahi et al. have fabricated $BaTiO_3$@Multi-walled carbon nanotube composites (TEM and HRTEM images are shown in Figure XX) for the photocatalytic oxidation of atrazine, an herbicide of high concern, under visible light (TEM and HRTEM images are shown in **Figure 17**). The authors reported that the incorporation of $BaTiO_3$ with MWCNT resulted in a great enhancement of the photoelectric and photocatalytic efficiencies. With a ratio of MWCNT (3.0 wt %) with $BaTiO_3$, the band gap was found to be 2.64 eV [188].

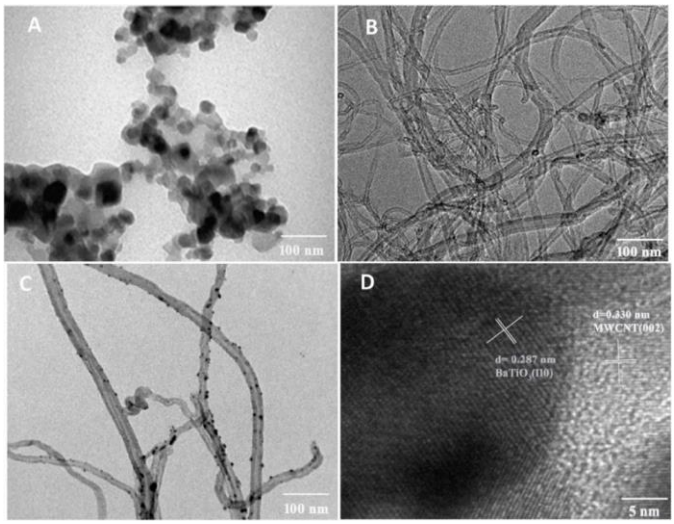

Figure 17. TEM images of (a) $BaTiO_3$, (b): Multi-walled carbon nanotube, (c): $BaTiO_3$@Multi-walled carbon nanotube. (d): HRTEM of $BaTiO_3$@Multi-walled carbon nanotube. Reproduced with permission from [188].

III.1.3. Synergistic piezo-photocatalytic activity

The introduction of polarization electric field features to the photocatalytic based materials has received a good attention recently as a new approach to enhance the photoefficiency through the increase of lifetime of the photogenerated carriers or/and the synergistical enhancement of the yield of redox species. It was widely reported that the higher piezoelectric activity of $XTiO_3$ based catalyst, the higher the photocatalytic activity. Huang et al. [159] reported that the combination of tetragonal phase $BaTiO_3$ with BiOI gives an enhanced photocatalytic efficiency under visible light compared to cubic $BaTiO_3$/BiOI because the cubic phase of $BaTiO_3$ has very low piezo-catalytic activity compared to the tetragonal phase. Therefore, the generation of separated redox

charges on the tetragonal phase is more pronounced. Similar tendency has been reported by Cui et al. [164], wherein, the authors studied the influence of the piezoelectricity on the photocatalytic efficiency of $BaTiO_3$ in terms of charges separation and stern layer generation. The authors reported that the enhancement of the piezoelectric nature resulted in better photocatalytic performance for the degradation of RhB under visible light due to the greater separation of electrons and holes, quite similar to that found in typical p−n junction systems. The authors reported also that the $BaTiO_3$ with higher piezoelectric nature has better dark adsorption of RhB molecules due to spontaneous polarization. Senthilkumar et al. [189] synthesized Ce-doped $BaTiO_3$ with different Ce loading and it was found that the sample with the highest polarization and d_{33} coefficient exhibits the best photocatalytic activity towards the oxidation of dyes.

Li et al. [190] fabricated multifunctional based catalysts via the combination of AgO with $BaTiO_3$. It was discovered that $Ag_2O-BaTiO_3$ composite is sono-catalytically active with an efficiency similar to the electrochemical one towards the oxidation of RhB. In addition, the performance of the sono-photocatalytic $Ag_2@BaTiO_3$ composites was more effective than those of other catalysts including $Ag_2O/BaTiO_3$ mechanically mixed, TiO_2P25, Ag_2O and $BaTiO_3$ under the same conditions. The electric field in $BaTiO_3$ can boost the separation of charges and increases the lifetime of such redox charges. The negative polarization side of $BaTiO_3$ can attract the positive holes photogenerated on Ag_2O, while the electrons can be repelled to the surface.

Lin et al. [19] have compared the efficiencies of piezocatalysis, UV-photocatalysis and piezo-photocatalysis for the oxidation of MO dye in water using $BaCaTiO_3$ nanowires

as a catalyst, and the degradation rates were found to be ~95% (100 min), ~90% (100 min) and 100% (40 min), respectively. Electron spin resonance (ESR) testes (**Figure 18.a,b**) showed that both ·OH and $\cdot^{-}O_2$ can be generated by different activation protocols, while a higher yield of ROSs was found in the synergistic piezophotocatalysis, explaining the highest efficiency towards MO degradation. As schematized in **Figure 18.c**, the ultrasonic and UV irradiation on the material leads to synergistic production of free charge carriers through the photo-excitation of the catalyst and the polarization charges, which in turn brings very effective advanced oxidation process. **Table 5 s**ummarizes the recent studies reported on the use of $XTiO_3$-based materials for the removal of chemical pollutants from water under different activation treatments.

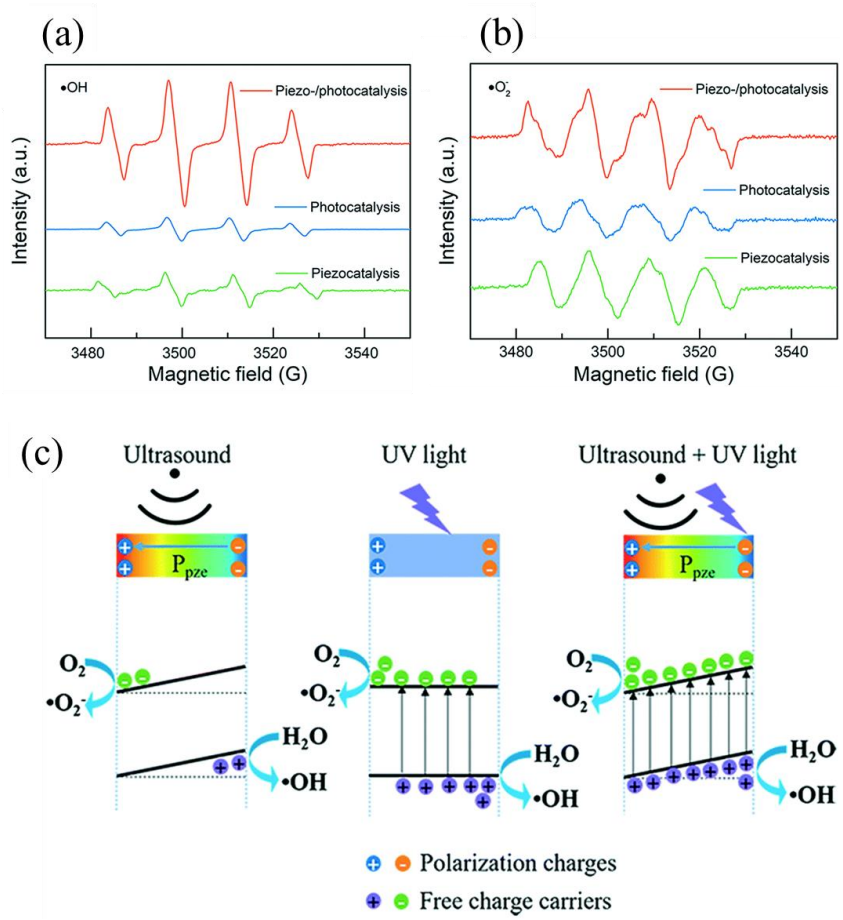

Figure 18. (a; b) ROSs generated by piezocatalysis, photocatalysis and piezo-photocatalysis (a: ·OH; b: $\cdot O_2^-$), (c): mechanistic pathways for the generation of ROSs. Reproduced with permission from [19].

Table 5. Applications of $XTiO_3$ based catalysts for the removal of pollutants from water

via piezocatalysis, photocatalysis or piezo-photocatalytic systems.

Catalyst	**E_g (eV)**	**Pollutants**	**Driving force**	**Dose**	**Removal rate (%)**	**ROSs**	**Ref**
Li-Doped $Bi_{0.5}Na_{0.45}K_{0.5}TiO_3$–$BaTiO_3$	1.95	Methyl orange (10 ppm); Estriol (1 ppm)	> 420 nm	1 g/L	75% for MO (150 min); 84% for Estriol (30 min)	$\cdot O_2^-$; h^+	[173]
(N^{3-}@Ni^{2+})-codoped $(Na_{0.5}Bi_{0.5})TiO_3$−$BaTiO_3$	2.06	Dibenzothiophene (100 ppm); RhB (10 ppm)	UV-Vis	1 g/L	90% for DBT (150 min) 92.4% for RhB (80 min)	·OH	[174]
$BaTiO_3$ and Ag@$BaTiO_3$	N.M.	Acid Black 1 (10 ppm)	UV-Vis	3 g/L	55% by $BaTiO_3$ (60 min) 80% by Ag@$BaTiO_3$ (60 min)	N.M.	[191]
Ag@$BaTiO_3$	2.95	MO (200 ppm)	UV	6 cm^2	~ 100 %(60 min)	N.M.	[192]
$(Bi_{1/2}Na_{1/2})TiO_3$	N.M.	MB, RhB, MO, AO7 (10 ppm)	100 W, 40 kHz	1 g/L	99.8, 95.0, 86.9, and 54.2% for AO7, MO, RhB, and MB, respectively (150 min)	·OH; $\cdot O_2^-$	[16]
$(Ba_{1-x}Ca_x)TiO3$	2.2	MO	λ > 420 nm	N.M.	65% (180 min)	N.M.	[172]
Bi0.5K0.5TiO3	3.31	MB (10^{-5} M)	UV	2 g/L	73 % (120 min)	N.M.	
$BaTiO_3$	N.M.	MO (5 ppm)	120 W, 40 kHz	1 g/L	>90% (160 min)	$\cdot O_2^-$; ·OH; h^+	[20]
$BaTiO_3$	N.M.	RhB (5 ppm)	40 kHz	0.1 g/L	97.5% (60 min)	·OH	[194]
BaTiO3	3.28	MB (20 ppm)	365-nm UV	1 g/L		N.M.	

Commentato [IR8]: subscripts here above and below

SrTiO3		3.35	MB (20 ppm)	365-nm UV	1 g/L		N.M.	
SrTiO3	(0 0 1)	N.M.	RhB (5 ppm)	300 W, 40 kHz	1 g/L	~ 58% (3h)	$\cdot O_2^-$; ·OH	[160]
	(1 1 0)					~ 52% (3h)		
	(0 0 1)/(1 1 0)					~ 83% (3h)		
$SrTiO_3$/BiOI		~ 1.8	MO (10 ppm)	λ > 420 nm	1 g/L	95% (40 min)	$\cdot O_2^-$	[195]
			Bisphenol A (10 ppm)			93% (120 min)		
			Antibiotic (20 ppm)			85% (90 min)		
BiVO3/ SrTiO3(1 %)		3.1	Sulfamethoxazole (10 ppm)	Solar simulator	1 g/L	91 % (60 min)	·OH, h^+ $\cdot O_2^-$	[178]
$SrTiO_3$/mesoporous-C3N4		2.80	Basic violet 10 (10 ppm)	240 W, 45 kHz	0.3 g/L	80% (120 min)	·OH, h^+ $\cdot O_2^-$	[196]
SrTiO3/Ag2S/CoWO4		2.6	Tetracycline (10 ppm)	300 W, 40 kHz	1 g/L	86% (300 min)	$\cdot O_2^-$, h^+, •OH	[197]
TiO_2/$SrTiO_3$/g-C3N4		2.88	Toluene (1000 ppm), (O_2/N_2 = 1/3)	420−780nm	0.2 g	~93% (6 h)	$\cdot O_2^-$, •OH	[179]
Graphene SrTiO3		/	MB (10 ppm)	410−700 nm	0.25 g/L	92% (120 min)	N/M	[182]
R-Graphene SrTiO3		~ 3.13	RhB (5 ppm)	Visible light	1 g/L	100% (7 h)	•OH, h^+	[198]
			Ciprofloxacin (5 ppm)			74.1% (7 h)		
			Ibuprofen(5 ppm)			68.4% (7 h)		
Rh doped $SrTiO_3$		2.42	MB (10 ppm)	410−700 nm	0.25	72.9% (120 min)	N.M.	[199]

					g/L			
$PbTiO_3$/TiO2		2.75	MB (10^{-5} M)	λ > 420 nm	4.6g/L	~ 80% (300 min)	N.M.	[177]
Ce Doped BaTiO3		N.M.	MB，MV，CR (5 ppm)	UV (254 nm)	0.3 g/L	90.2% （120 min） 82.4% (120 min) 78.5% (120 min)	N.M.	[189]
$BaTiO_3$		N.M.	Acid Orange 7	5.7×10^{-5} M		80% (90 min)	N.M.	[200]
$BaTiO_3$		N.M.	MO (5 ppm)	80 W，~40 kHz.	1 g/L	~100 % （160 min）	·OH; $\cdot O_2^-$	[152]
(Ba,Sr)TiO3			MO (5 ppm)	80 W, 40 kHz	1 g/L	~100 % （120 min）	·OH; $\cdot O_2^-$	[23]
N-doped BaTiO3		2.73	RhB (10 ppm)	420–780 nm	1 g/L	48 %(4h)	N.M.	[201]
$BaTiO_3$		2.93	CV (10 ppm)	UV (365 nm)	0.5 g/L	100 % （48 h）		[55]
$BaTiO_3$ Ag@$BaTiO_3$		N.M.	4-chlorophenol (25 ppm)	110 W, 40 kHz,	2 g/L	71% (120 min) 82.3% (120 min)	h^+; e-; •H, •OH; $\bullet O_2^-$; $^1O_2$; H_2O_2	[202]
$BaTiO_3$	Cubic	3.1	MO (10^{-5} M)	300 W, 40 kHz	0.75g/L	2% (60 min)	$\bullet O_2^-$	[159]
	Tetragonal	2.95				45% (60 min)		
$BaTiO_3$	Cubic	N.M.	RhB (10 ppm)	Solar simulator	3 g/L	~7% (60 min)	N.M.	[164]
	Tetragonal					~21% (60 min)		
Ag-$BaTiO_3$	Cubic	N.M.	RhB (10 ppm)	Solar simulator	3 g/L	~53% (60 min)	N.M.	[164]
	Tetragonal					100% (60 min)		
Bi_2O_3/$BaTiO_3$		~2.75	MO, MB (10 ppm)	365 nm	2 g/L	~99% (50 min)	N.M.	[166]

C-BaTiO3/BiOI	~1.87	MO (0.02 mM)	λ > 420 nm	1 g/L	50% (60 min)	$•O_2^-$	[159]
T-BaTiO3/BiOI	~1.87	MO (0.02 mM)	λ > 420 nm	1 g/L	85.5% (60 min)	$•O_2^-$	[159]
SrTiO3	3.21	MO (10 ppm)	365 nm	5mg/L	>95% (180 min)	N.M.	[203]
SrTiO3/CeO2	N.M.	Direct Red (100 ppm)	UV	1.5 g/L	~100% (60 min)		[175]
$La_{0.8}A_{0.2}TiO_{3.5-\delta}$	2.95	Congo red (100 ppm)	visible light	1 g/L	81% (60 min)	N.M.	[204]
(A=Ba, Sr, Ca)	2.9				70% (60 min)		
	2.9				67% (60 min)		
$Ba_{1-x}CaxTiO3$	N.M.	MO (5 ppm)	120 W, 40 kHz	1 g/L	~95% (100 min)	$·OH; ·O_2^-$	[19]
			365 nm`	1 g/L	90% (100 min)	$·OH; ·O_2^-$	
			US + light	1 g/L	100 % (40 min)	$·OH; ·O_2^-$	
$Ag_2O@BaTiO_3$	~2.7	RhB (15 ppm)	50 W, 40 kHz	1 g/L	~10% (60 min)	N.M.	[190]
			+ 365 nm	1 g/L	~62% (60 min)		
			US + light	1 g/L	~88% (60 min)		
BaTiO3@g-C3N4	N.M.	MO (5 ppm)	Solar simulator	0.5g/L	76% (6 h)	$·O_2^-, h^+$	[167]
Ag@BaTiO3/TiO2	N.M.	MB (10 ppm)	xenon lam	4 cm2	95% (180 min)	N.M.	[205]
(BaCa)(ZrTi)TiO3/Bi2O3	2.25	RhB (10 ppm)		1 g/L	92% (60 min)	$h^+; ·O_2^-$	[206]
BaTiO3/TiO2	2.99	Acetaminophen (5 ppm)	Solar simulator	1 g/L	95% (4 h)	N.M.	[168]
BaTiO3	N.M.	RhB (5ppm)	ΔT (25-45°	1 g/L	95% (80 × ΔT)	$h^+; ·O_2^-; ·$	[163]

			C)			OH	
BaTiO3/α-Fe2O3	3.1	RhB (10 ppm)	simulated sunlight	3 g/L	~98% (120 min)	h^+; ·OH	[207]
							[160]
BaTiO3 -MWCNT	2.64	Atrazine (50 ppm)	λ > 410 nm	2 g/L	100% (40 min)		

III.1.4. Antibacterial activity of $XTiO_3$-based catalysts

Many studies reported that $XTiO_3$-based materials exhibit an excellent antimicrobial activity. Herein, we exemplify the mechanistic antimicrobial pathways of $XTiO_3$-based catalysts in dark and under irradiation. Due to the strong antibacterial activity of Ag species [208, 209], Ag-decorated piezocatalysts were reported for enhanced piezo and antibacterial activities. Shuai et al., [210] have decorated $BaTiO_3$ by Ag nanoparticles (NPs) using dopamine to obtain a strawberry-like structured Ag@$BaTiO_3$, as shown in **Figure 19.a**. AgNPs in this catalyst enhance the strength of the polarized electric field on $BaTiO_3$ because of its excellent conductivity. Ag NPs on the top surface of $BaTiO_3$ reacts as antibacterial agent by releasing Ag^+ ions, which attack the pathogenic species, or by the generation of ROSs. After that, the authors incorporated Ag@$BaTiO_3$ into polyvinylidene fluoride (PVDF) scaffold self-developed Selective Laser Sintering (SLS) technique. It was found PVDF/Ag@$BaTiO_3$ has better ultrasonic piezoelectric and antibacterial activities against *E.coli* compared to PVDF/@$BaTiO_3$.

Kushwaha et al. [173] have tested the antibacterial activity of Li-doped $Bi_{0.5}Na_{0.45}K_{0.5}TiO_3$–$BaTiO_3$ towards *Escherichia coli* in dark condition. As shown in **Figure 19.b**, the antibacterial effect increased as a function of the catalyst mass. The

antifungal activity was evaluated against *Aspergillus Flavus*, which can cause food poisoning. It was reported that the antimicrobial activity is due to the diffusion of surface ions from the catalysts, which provoke the destruction of the membrane of microbial species. Wadge et al. [211] have studied the antibacterial activity of $GaTiO_3$ against Staphylococcus Aureus in dark. The authors reported that Staphylococcus aureus showed a high resistance compared to other pathogenic species (e.g., A. Baumannii) in similar conditions.

In terms of photocatalytic activation, Yamaguchi et al. [212] have synthesized and investigated the photocatalytic activity of Rh-doped $SrTiO_3$ for the selective inactivation of Bacteriophage Qβ (NBRC20012), known as a bacterial predator, in the presence of *E.coli* under visible light ($\lambda > 440$ nm) as shown in **Figure 19.c**. Rh-Doped $SrTiO_3$ under visible light was able to inactivate effectively Qβ in the presence or absence of *E.Coli*. Rh^{4+} deposited on the surface of $SrTiO_3$ is induced by light irradiation. In addition, the co-doping of $SrTiO_3$ by Rh^{4+} and Sb^{5+} was not effective for the inactivation of phage as Sb^{5+} suppresses by compensation the shift from Rh^{3+} to Rh^{4+} under light irradiation. The inactivation of Bacteriophage Qβ has a potential importance in bacterial fermentation processes. The antibacterial activity of $BaTiO_3$ under light was reported by Kumar et al [213]. The authors reported the excellent antibacterial activity is due to the remaining polarization on poled $BaTiO_3$ which in turn enhances the separation of charge carries of the photoexcited $BaTiO_3$. In addition, it was found that the positive pole of $BaTiO_3$ has better photocatalytic antibacterial activity due to stronger interaction with bacterial species.

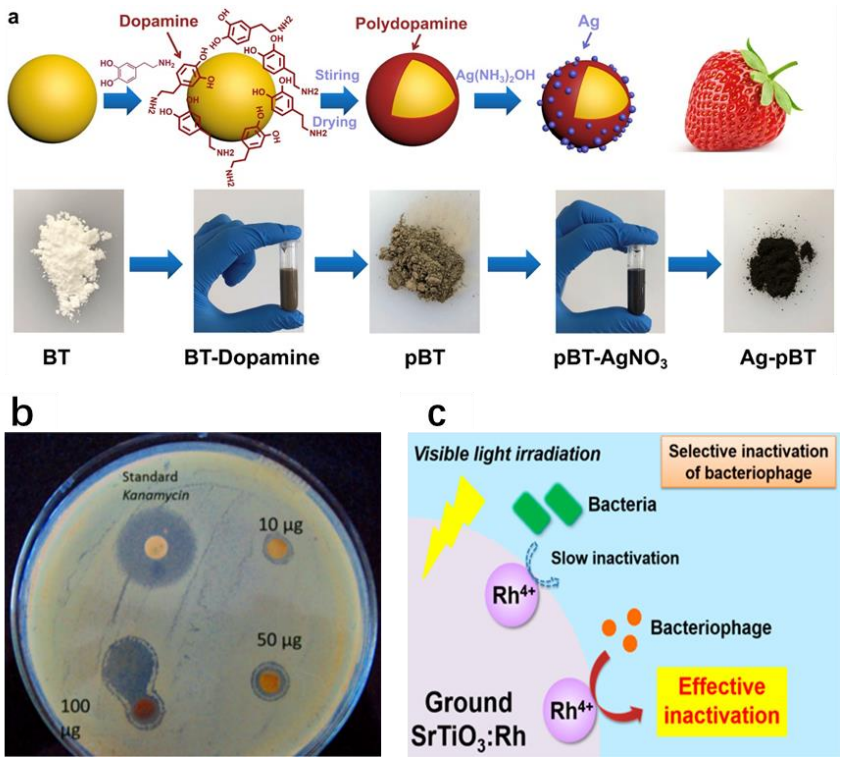

Figure 19. (a): Ag NPs/polydopamine decorated $BaTiO_3$ for the inactivation of *E.coli*. reproduced with permission from [210]. (b) Antibacterial activity of $Bi_{0.5}Na_{0.45}K_{0.5}TiO_3$–$BaTiO_3$ and commercial kanamycin towards *E.coli* inactivation, reproduced with permission from [173] . (c): $RhTiO_3$ as an efficient antiphage material (against Bacteriophage Qβ species) in the presence *E.coli* under visible light (λ > 440 nm), reproduced with permission from ref [212].

Table 6 summarizes comparatively the antibacterial activities of several $XTiO_3$ based materials.

Table 6. Bacteria inactivation by $XTiO_3$ materials

Catalyst	Microbial species	Remarks	Ref
(Li-Doped Bi0.5Na0.45K0.5TiO_3–$BaTiO_3$	Escherichia coli Aspergillus flavus	Dark condition via on Luria–Bertani (LB) agar. The authors reported that the activity is due to diffusion of ions from the catalyst.	[173]
Ga_2TiO_3	Staphylococcus aureus	S. aureusis showed a high antibacterial resistant in $GaTiO_3$ in dark condition.	[211]
$SrCaTiO_3$	Staphylococcus aureus	The authors studied the effect of Sr/Ca ratio in $SrCaTiO_3$ system has an impact on the antibacterial activity. The best samples showed a reduction rate of 97% against S aureus (10^4 CFU·mL^{-1}) within 24 h. Sample with the highest photoactivity has also the highest antibacterial activity.	[214]
$BaTiO_3$	S. aureus *E.coli*	$BaTiO_3$ has an excellent antibacterial activity against both bacterial species using disc diffusion method. The antibacterial activity was higher against Gram positive bacteria than Gram negative bacteria.	[215]

$BaTiO_3$	P. aeruginosa S. aureus	The inactivation rates of S. aureus and P. aeruginosa biofilms using BaTiO3NPs (100 µg/mL) were 85 and 80 %, respectively	[216]
$BaZrTiO_3$	S. aureus M.luteus E. coli, K. pneumoniae	$BaZrTiO_3$ has an effective antibacterial activity against both gram-positive and gram-negative bacterial species.	[217]
$AgO@SrTiO_3$	S. aureus	The long-term antibacterial activity was due to the controllable release of both Ag^+ and Sr^{2+} which are able to inhibit the growth of s. aureus.	[218]
Ag-decorated $BaTiO_3$	*E.coli*	AgNPs on the surface of $BaTiO_3$ leads to enhance the piezocatalytic activity due to its conductivity. $AgBaTiO_3$ could inactivate *E.coli* via the release of Ag+ species or by the generation of ROSs	[210]
Ga-polydopamine $SrTiO_3$	*E.coli* S. aureus	Ga doped $SrTiO_3$ has a potential antibacterial activity against both *E.coli* and S. aureus species, wherein, a total inhibitions was found within 24 h. However, the larger inhibition was observed against S. aureus than *E.coli*. As a control, bare $SrTiO_3$ showed low antibacterial activity. The synergistic Ga/Sr system is the reason behind the highest antibacterial observed in the case of Ga doped $SrTiO_3$.	[219]

Rh doped $SrTiO_3$	Bacteriophage Qβ	The selective inactivation of Bacteriophage Qβ was carried out using Rh@$SrTiO_3$ under visible light (λ > 440 nm) in the presence of *E.coli* as a bacterial example. Under dark, there was not inactivation process. The change from Rh^{3+} to Rh^{4+} under light was the main reason behind the antiphage mechanism. Co-doping of $SrTiO_3$ by Sr and Rh limits the antiphage reaction.	[212]
$BaTiO_3$	Escherichia coli	96% of *E.Coli* population was killed within 30 min by poled $BaTiO_3$ under UV light, which was more effective than unpoled $BaTiO_3$. In dark condition, the unpoled $BaTiO_3$ negative poled $BaTiO_3$ were inactive. However, the positive poled $BaTiO_3$ showed 90% bacterial inactivation within 60 min. It was found that the unpoled $BaTiO_3$ is not able to produce ROSs. While, the poled can produce $\bullet O_2^-$ in both dark and UV conditions.	[213]

III.2 Energy conversion

Titanate based materials are also widely used in the energy conversion field. Due to their photocatalytic properties, they can be active to promote up-hill photosynthetic reactions, such as the photoreduction of CO_2 to solar fuels or hydrogen production by

water splitting with or without sacrificial agents. Both these applications can be also interpreted as solar energy storage into various energy vectors. Other interesting applications are their use in hydroelectric cells or in piezoelectric devices, now intended for energy conversion, rather than for the ROSs generation for environmental remediation as in previous sections. Some significant examples have been selected and described in the following.

III.2.1. Photocatalytic reduction of water and CO_2

Perovskite crystals are made of corner-connected BO_6 octahedra and 12 oxygen coordinated A cations, located between the octahedral, in principle forming an undistorted cubic lattice. Due to the electronegativity of the cations and their ionic radius or to the presence of substituents, the octahedral can be tilted. The bond strength with oxygen is stronger for the B cation than for A [220]. $SrTiO_3$ is one of the most studied perovskites for the photocatalytic hydrogen production due to more negative conduction band potential with respect to TiO_2. It can be produced by hydrothermal synthesis in form of nanoparticles (30-60 nm) or in film by electrodeposition. Its main drawback is the limited solar light absorption due to wide band gap. This can be circumvented by doping with heterocations or by the realisation of heterojunctions with visible sensitive materials.

$SrTiO_3$ samples were prepared by a polymerised complex method, hydrothermal synthesis and ball milling [89]. The latter resulted in the incorporation of Fe 3d donor states, shifting the absorption edge towards visible light. H_2 productivity up to 3.2 mmol/g h was achieved with 500 W Hg lamp irradiation and using methanol as hole

scavenger. Enhanced visible absorption has been also achieved through Mo-doping of $SrTiO_3$ [221], where Mo^{2+}, Mo^{4+} and Mo^{6+} coexist. The latter is ineffective from the photocatalytic point of view, while the tetravalent species add acceptor levels below the conduction band of the titanate. Various other dopants were tested. In general, the best performance for the photocatalytic hydrogen production was achieved when dopants level near the conduction band were formed, because they effectively trap hot electrons and lower the band gap. On the contrary when impurity states are located in mid gap positions they predominantly act as recombination sites [220]. The addition of noble metal dopants such as Rh was also tested, experiencing a transition from n- to p-type semiconductor.

Composite heterojunctions with different lower band gap semiconductors and the assembly of composites with C-based materials such as g-C_3N_4 have been also tested for hydrogen evolution in photocatalytic or photoelectrocatalytic devices. A comprehensive review on the topic has been very recently published [220].

Mesoporous $SrTiO_3$ was prepared by surfactant assisted sol gel synthesis aiming at a better mass transfer thanks to larger pores. 0.156 mmol/h g_{cat} H_2 productivity was achieved upon UV light irradiation using again methanol as hole scavenger [222]. Interestingly, an increasing temperature increased the activity, confirming the same trend observed for the photoreduction of CO_2 [223, 224]. The addition of metal co-catalysts were also investigated, obtaining better results with Au (0.337 and 0.2 mmol/h g_{cat} under UV or Visible light irradiation, respectively), attributed to its electronegativity and electron affinity [225].

As in the case of carbon, also titania and titanate based materials can be shaped in elongated nanostructures, such as nanotubes, nanofibers, nanorods, etc., with relatively simple hydrothermal procedures which have been recently reviewed [226]. The use of alkaline hydrothermal conditions typically induces the formation of morphologically different and randomly oriented titanate nanotubes. Anodisation brings to the synthesis of a sharper array of sizes and uniformly oriented material, though at the expenses of a more complex procedure. By contrast, hydrothermal synthesis from a Ti precursor in alkali medium can occur under mild conditions (110-150°C, 24 h) with possible post-synthesis adjustment of the size through microwave or ultrasound treatment. To avoid operation under autogenous pressure, the synthesis under reflux conditions may be used, though non–unanimous results are reported leading either to nanotubes or to nanosheets. Some post processing of titanate nanosheets in colloidal suspension by exfoliation with NaOH has been reported [227], or using a mixture of NaOH and KOH [228]. Similar synthesis at temperature higher than 170°C leads instead to the formation of nanofibers [229]. The stability of these structures is poor in acidic media, which lead to the decomposition into anatase and rutile titania. On the contrary, mechanical treatment such as in ultrasounds shortens the length of the fibers.

These materials exhibit higher electron conductivity than anatase titania, suggesting their application in electrochemical devices for energy conversion, e.g., in electrodes for fuel cells and in lithium-ion batteries. This latter application is particularly straightforward due to the open mesoporous structure that allows fast transport of Li ions and consequent high value of the charge/discharge capacity. These features are

accompanied by robustness and good safety [230]. These titanate nanotubes have also different performance for photocatalytic applications. The presence of Na^+ ions due to the alkaline synthesis is detrimental for photocatalytic activity, these species acting as charge recombination sites. The deep ion exchange with protons improves the activity, but in most reports, the effective role of titanates themselves or rather of their decomposition products (rutile or anatase) is unclear.

$SrTiO_3$ nanotubes have been grown co-axially with TiO_2 nanotubes and functionalised with Au-Cu nanoparticles. They were employed for the photoreduction of CO_2 (33 % in Ar) under UV-Visible irradiation obtaining predominantly CO (3.8 mmol/h g) and hydrocarbons (0.725 mmol/h g), ca. 60% of which constituted by CH_4 [231]. A key feature was the obtainment of holes in the walls of the nanotubes, which improved the surface area and allowed better mass transfer in gas phase. Furthermore, the heterostructure allowed improved charge separation and hydrazine provided a reductive environment. Hydrazine, here used as a hydrogen storage material, decomposes to N_2 and H_2 and boosts the production of methane by ca. one order of magnitude with respect to H_2O. The presence of hydrazine also allows keeping the Au-Cu nano-alloy stable and in reduced form.

$NiTiO_3$ and $CoTiO_3$ have been used for the photoelectrochemical and photocatalytic production of H_2O_2. The latter has been selected for solar energy storage due to its potential for application as green oxidant or liquid fuel for fuel cells. The photocatalysts were selected based on their flat band potentials that rule out the possible parasitic reduction of water to hydrogen or of oxygen to water [232]. The materials were

prepared through a hydrothermal route. The activity for the production of H_2O_2 was higher for the $NiTiO_3$ material under photocatalytic reaction conditions and occurred both through partial oxidation of water and partial reduction of oxygen as desired.

The addition of NiO to $SrTiO_3$ also allows the photocatalytic water splitting by limiting the rate of charge recombination [233]. In order to clarify the role of the NiO co-catalyst some Density Functional Theory calculations have been carried out. The evaluation of the density of states pattern evidenced that no trapping states are present within the gap, the valence band is mainly constituted by NiO and the conduction one by $SrTiO_3$. Furthermore, considering the heterostructure, charge separation is interpreted as transfer of the photogenerated holes from $SrTiO_3$ to NiO.

$CaTiO_3$ is a cheap industrial semiconductor with band positions compatible with water splitting. Its high stability allows fine engineering of its formulation to improve its photocatalytic features, in particular the transport of the carriers. One attempted strategy was the doping with ZrO_2 to achieve $CaTi_{1-x}Zr_xO_3$ (x=0-0.21). An increase of band gap (from 3.42 to 3.55 eV), with decreasing valence band potential (from 2.12 to 1.75 eV and of the conduction band one (from -1.29 to -1.80 eV) at increasing x [234]. The maximum activity for hydrogen evolution was attained for x=0.09 and amounted to a stable productivity of 679 μmol/h g_{cat}.

The use of non-centrosymmetric mixed oxides is a possible strategy to hinder the electron-hole recombination in photocatalysts due to the formation of an intense polarisation potential. However, most semiconductors with this structure have wide band gap. Furthermore, the use of visible sensitisers such as CdS, leading to charge

transfer, shields this potential. If these materials also have a piezoelectric property, e.g., Ag_2O-$BaTiO_3$ they can be activated with ultrasounds as periodic wave, preventing such shielding effect. $PbTiO_3$ is also characterised by high polarizability and a photocatalyst with type II heterojunction has been prepared with CdS [235, 236]. The H_2 productivity during experiments of piezo-photocatalysis was 849 μmol/g h, extraordinarily higher than when tested as piezocatalyst (400 μmol/g h) or photocatalyst (ca. 100 μmol/g h). A finite element simulation was carried out to elucidate the reasons of so high activity improvement (**Figure 20**). The simulation evidenced that the $PbTiO_3$/CdS composite reached higher piezoelectric potential difference with respect to the pure components. For this reason, a higher piezo-photocatalytic hydrogen productivity was achieved through better carriers separation and prevention of the screening of the polarization electric field (**Figure 21**).

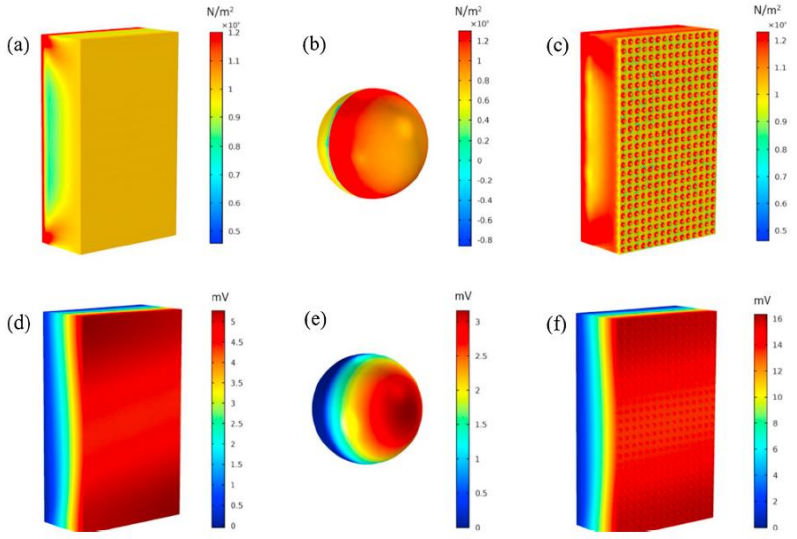

Figure 20. Finite elements modelling of the strain distribution and the corresponding piezoelectric potential distribution for the surface of $PbTiO_3$ (a, d), CdS (b, e), and $PbTiO_3$/CdS (c, f) with an external load of 1.0×10^8 Pa. Reproduced by kind permission of Elsevier BV from [34]. RICHIEDERE PERMESSO

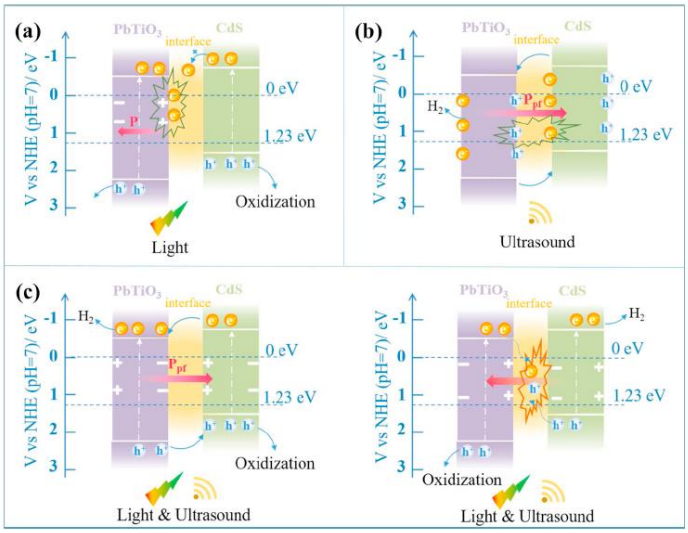

Figure 20. Schematic diagram of photocatalysis (a), piezocatalysis (b), and piezo-photocatalysis (c) for $PbTiO_3$/CdS composites. Reproduced by kind permission of Elsevier BV from [34]. RICHIEDERE PERMESSO

$SrTiO_3$ is widely employed as photocatalyst for reduction reactions due to its negative conduction band potential, constituted by Ti 3d orbitals, while the valence band is formed with O 2p orbitals [20]. DFT calculations suggested the possibility to dope this material with boron to get surface states near the valence band of the oxide [91]. The co-doping of $SrTiO_3$ with B and Fe was investigated for the photoreduction of CO_2 to

solar fuels and of water to H_2 [237]. According to structural characterisation Fe^{3+} substitutes Ti^{4+} and adds new energy states near the conduction band of $SrTiO_3$. An evident decrease of the band gap and a corresponding shift towards visible light absorption was observed. The band gaps were 3.4 eV (λ = 360 nm) for $SrTiO_3$, 3.0 eV (λ = 410 nm) for the Fe-doped material, 2.3 eV (λ = 540) for the B-doped catalyst and 1.9 eV (λ = 650 nm) for the Fe-B-codoped one (**Figure 21**). The photoluminescence of the doped samples was also reduced with respect to the bare titanate, evidencing lower charge recombination. For both the reactions a considerable improvement of photocatalytic activity was observed in the order Fe < B < Fe+B with rather constant performance during time [237].

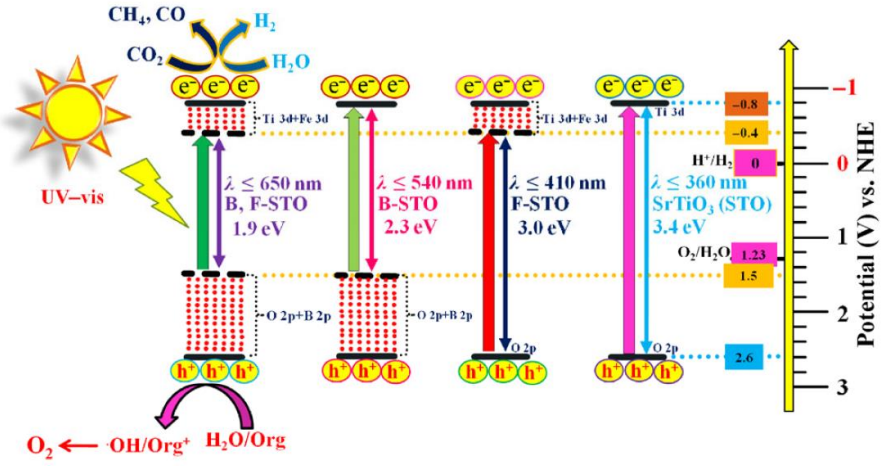

Figure 21. Band potentials for differently B and Fe doped $SrTiO_3$. Reproduced by kind permission of XXX from [237]. RICHIEDERE PERMESSO.

$SrTiO_3$ was epitaxially grown on the surface of p-Si to form a photocathode for a

photoelectrochemical cell. The incident light crosses the $SrTiO_3$ ultrathin layer to be absorbed by Si, where charge separation occurs. The electron travels back through the $SrTiO_3$ layer to reach a composite surface of Ti and Pt, where H_2 evolves. The addition of a further Ti layer over $SrTiO_3$ is motivated by the unstable incorporation of Pt over its surface. Furthermore, it serves to decouple Pt from Si, with the latter forming a junction with Ti and not with Pt [238]. Different nanodevices were assembled and tested for photocurrent generation upon irradiation, proving to be sensitive to visible light. Unfortunately, only a qualitative proof of hydrogen production is reported, without quantification and comparison with literature data.

In order to improve the photocatalytic activity for H_2 production, heterojunctions between $SrTiO_3$ (10-40%) nanoparticles and $SnNb_2O_6$ nanosheets was prepared [239]. Enhanced photocurrent was observed upon irradiation with intermittent visible light due to a considerable decrease of the band gap from 3.2 eV of the pristine $SrTiO_3$ to 2.59 eV of the niobate. The materials, loaded with 1 wt% Pt, were tested for the visible light induced photocatalytic hydrogen production using methanol as hole scavenger. Bare $SrTiO_3$ as expected was almost inactive due to negligible visible light absorption. All the composites were more active than the single components and the catalyst with 20% $SrTiO_3/SnNb_2O_6$ led to ca. 300 times increase of H_2 productivity with respect to the bare titanate and doubled the yield of the bare niobate, demonstrating the effectiveness of charge separation through the junction.

The perovskite structure is sufficiently stable to allocate a high concentration of oxygen vacancies. In the specific case of $SrTiO_3$ this corresponds to the partial reduction of Ti^{4+}

to Ti^{3+} with improved absorbance in the visible region. With relatively limited vacancy concentration (3.23 at%) a H_2 productivity of 2.2 mmol/h g was observed [240] and the formation of a stable photocurrent [241]. The reduction of $SrTiO_3$ to produce "black" strontium titanate has been reported also by direct hydrogenation and by molten aluminium reduction in a two zone furnace [242, 243].

Engineering the surface oxygen vacancies has been also considered as a strategy to improve the adsorption and activation of CO_2 and in turn the efficiency of its photoreduction. For instance, $Sr_2Bi_2Nb_2TiO_{12}$ with surface oxygen vacancies increased the photoresponse in the visible region and the electron hole separation. As a result increased CO productivity was observed [244]. $Bi_4Ti_3O_{12}$ nanosheets with oxygen vacancies were synthesised using a hydrothermal procedure followed by reduction with glyoxal. The resulting maximum CO productivity was 0.012 mmol/h g, enhancing by 3 times the value of the non-reduced sample [245].

$SrTiO_3$ has been widely used to assemble photoelectrochemical cells for water splitting and it was used to model the parameters affecting the overall performance of the photoelectrode since the material properties are well known. The performance of the semiconductor photoelectrode is characterised as $J_{ph} = e\Phi \times \eta_{ct} \times \eta_{sr}$. Where J_{ph} is the photocurrent density, e the elementary charge, Φ the absorbed flux of photons and η are the efficiencies of charge transfer (subscript *ct*) and of surface reaction (subscript *sr*). In particular, the effect of doping with Nb on the carriers density was studied by Kawasaki et al. [246]. With increasing the charge density, the recombination rate increased, with shorter lifetime. While increasing the Nb loading from 0 to 1 at% the

electron mobility remained almost unchanged, while the carrier density increased from 10^{15} to 10^{20} cm^{-3}. Overall, a photoanode with low carrier density layer of $SrTiO_3$ on a conductive (high carrier density) Nb:$SrTiO_3$ base exceeded the photon-to-current efficiency of homogeneously doped $SrTiO_3$ and attained ca. 100% efficiency irradiating at λ=300 nm. This insulating layer prolonged the photocarrier lifetime.

A photocathode has been assembled with an epitaxial $SrTiO_3$ layer grown on a n-p-GaAs(001) surface (**Figure 22**) [247]. The titanate layer protected the photocathode of GaAs for more than 24h continuous H_2 production. The voltage achieved did not allow unassisted H_2 evolution, but could be joined with a Si dual junction cell operating as a photocathode to overcome the needed thermodynamic minimum potential of 1.23 V.

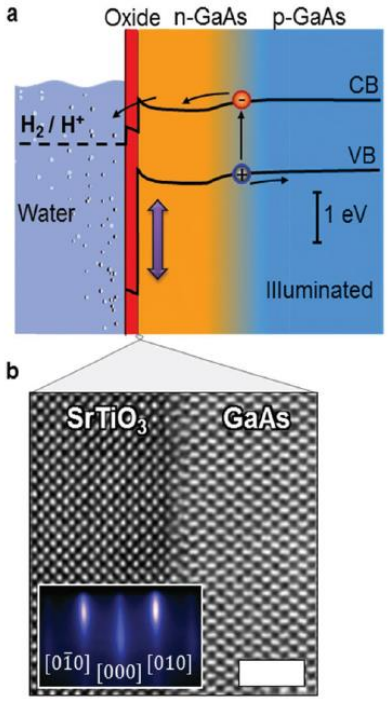

Figure 22. Epitaxial $SrTiO_3$ layer grown on a semiconductor solar cell. (a) Sketch of

the 16 nm-thick $SrTiO_3$/np-GaAs(001) photocathode, where sunlight is absorbed in the semiconductor solar cell, generating a voltage and driving electrons to the oxide–water interface for hydrogen evolution. (b) Atomic structure of the $SrTiO_3$/n-GaAs(001) interface using high-angle annular dark-field imaging (2 nm scale bar), and Reflection High-Energy Electron Diffraction (RHEED) of the $SrTiO_3$ surface taken along the [100] direction after growth (inset). Reproduced by courtesy of the Royal Society of Chemistry from [247] under the Creative Commons Licence.

III.2.2. Other energy related applications of $XTiO_3$-based materials

Hydroelectric cells (HECs) are new devices with potential application in energy conversion. Electric energy may be obtained by splitting water over specific materials, originally ferrite and magnetite, characterised by surface oxygen vacancies and unsaturated cations. The assembly of these defective oxides between two electrodes may end in water dissociation into H_3O^+ and OH^-, which migrate towards an Ag and Zn electrode, respectively, with formation of a net current and H_2 production [248]. TiO_2 and $BaTiO_3$ composites have been considered for this application.

Water molecule dissociation occurs thanks to surface oxygen vacancies and unsaturated cations: in this case surface Ti^{3+} ions act as Lewis acid and oxygen vacancies as Lewis base. These surface pairs attract the polar water molecules closer and charge transfer occurs with dissociation into OH^- and H^+ ions. The formed protons hop and get trapped inside nanopores at the Ag electrode side, leading to a high electrostatic potential that dissociates physisorbed water molecules. Thus, water dissociation is continuously

sustained on the surface. Hydroxyl groups, instead, diffuse through the oxygen vacancies towards the Zn electrode, where the metal is oxidised to $Zn(OH)_2$. The electron flow reduces the hydronium ion and reaching the Ag electrode produces H_2. HEC based on TiO_2 with ca. 3 cm^2 area achieved peak power of 0.245 mW and maximum current 3.05 mA. The one based on $BaTiO_3$ delivered peak power 0.324 mW and maximum current of 3.66 mA [249].

Supercapacitors have high capacitance, high power density and fast discharge rate. They may be used for peak power needs such as backup power devices or in association with batteries in electrical vehicles to support peak demand. Hydrogen titanate is a n-type semiconductor and can be used for this application, especially when it is configured as aligned nanotubes and in the presence of vacancies. This material was grown on a Ti foil by a hydrothermal technique in the form of nanotubes ca. 20 nm in diameter and with film thickness of 15 nm. Ion beam irradiation with Ar^+ improved the charge storage capacity (1572 F/g at a normalised mass current of 10 A/g), leading to higher capacitance with respect to other titanates and other oxides [250].

IV. Current Challenges and Outlook

$XTiO_3$ perovskite-type oxides, combining the piezocatalytic and photocatalytic activities, have been suggested as very useful multifunctional materials in environmental and energy applications. We propose the following conclusions and approaches to widen accurately the use of $XTiO_3$ perovskite-type oxides.

With regard to enhancing both the piezocatalytic and photocatalytic performances, many strategies have been reported to modify $XTiO_3$ perovskite-type oxides through

the introduction of heterocations, doping, combination with other semiconductors or carbon materials. It was concluded also that the activity of these $XTiO_3$ perovskite-type oxides is highly depending on the synthesis routes and conditions. The phase control of bare $XTiO_3$ catalysts is very important key. Many reports mentioned that the cubic form of $BaTiO_3$ is less or quasi-inactive under ultrasonic irradiation, while the tetragonal phase showed an excellent piezocatalytic activity. This latter is due to the enhanced piezoelectric potential of tetragonal phase, unlike cubic one. In addition, other significant parameters could be controlled during the synthesis for enhanced piezo-photocatalytic activity such as oxygen vacancies (which affect polarization orientation of piezo-materials), morphology, wettability and the crystalline size. It was reported also that the conductivity of piezocatalysts is a significant factor, which was found to be more decisive than the piezoelectric coefficient. Further studies, should be investigated to understand the well decisive phenomena that drive the piezo-catalytic or photocatalytic activity in $XTiO_3$ perovskite-type oxides, depending on the application.

Despite many studies carried out to investigate the piezo and/or photoactivity of $XTiO_3$ perovskite-type oxides, through this review, we figured out that most of reports have mainly focused on the oxidation of organic dyes, however, less attention was given to other types of pollutants. In this respect, the piezo-photocatalytic activities of $XTiO_3$ perovskite-type oxides should be well proved towards other organic/inorganic pollutants including pesticides, herbicides, pharmaceutical, heavy metals, NO_x, pathogenic species, and also mixed pollutants or real wastewaters.

As above-mentioned, the structure phase of $XTiO_3$ perovskite-type oxides, which is depending on calcination temperature, is a decisive factor. Therefore, $XTiO_3$ based materials could lose or partial suppress their piezo-(photo)-activities during industrial scaling up processing, e.g., the coating of tile surface which requires high temperature treatment. More attention to the dependency between the phase transformation and the piezo-(photo)-activities should be unraveled.

For environmental remediation, the deactivation of $XTiO_3$ perovskite-type oxides during piezo-catalytic or/and photocatalytic reactions, and approaches to prevent the fast deactivation should be investigated. In addition, toxicity assessment of $XTiO_3$ perovskite-type NPs in water should be considered.

In terms of photocatalytic applications for energy conversion, data are often provided with inappropriate quantification. For instance, in some studies only very detailed electro-chemical characterization is provided, without significant data on the productivity of hydrogen or solar fuels. This represents an incomplete information, since parasitic dissipation of charges may occur, or insufficient reactants adsorption and activation, which would drop the productivity to unacceptably low levels. Therefore, it is highly recommended to precisely quantify conversions and/or productivity to really estimate the applicative potential and allow estimates for feasibility and scale up.

For a wide transfer of $XTiO_3$ perovskite-type oxides to real industrial use, competitive $XTiO_3$ materials should be designed for a specific application, which the industry has interest. In this regard, innovation in synthesis and in nanoarchitectures is required to fulfil with an accurate industrial use.

References

[1] E. Rizzo, P. Bardos, L. Pizzol, A. Critto, E. Giubilato, A. Marcomini, C. Albano, D. Darmendrail, G. Döberl, M. Harclerode, Comparison of international approaches to sustainable remediation, Journal of environmental management, 184 (2016) 4-17.

[2] P. Favara, D. Raymond, M. Ambrusch, A. Libera, G. Wolf, J.A. Simon, B. Maco, E.R. Collins, M.A. Harclerode, A.D. McNally, Ten years later: The progress and future of integrating sustainable principles, practices, and metrics into remediation projects, Remediation Journal, 29 (2019) 5-30.

[3] P. Bardos, Progress in sustainable remediation, Remediation Journal, 25 (2014) 23-32.

[4] G. Centi, G. Iaquaniello, S. Perathoner, Chemical engineering role in the use of renewable energy and alternative carbon sources in chemical production, BMC Chemical Engineering, 1 (2019) 1-16.

[5] S.K. Ngoh, D. Njomo, An overview of hydrogen gas production from solar energy, Renewable and Sustainable Energy Reviews, 16 (2012) 6782-6792.

[6] F. Díaz-González, A. Sumper, O. Gomis-Bellmunt, R. Villafáfila-Robles, A review of energy storage technologies for wind power applications, Renewable and sustainable energy reviews, 16 (2012) 2154-2171.

[7] M. Asghar, J. Zhang, H. Wang, P. Lund, Device stability of perovskite solar cells–A review, Renewable and Sustainable Energy Reviews, 77 (2017) 131-146.

[8] L. Pan, G. Zhu, Perovskite materials: synthesis, characterisation, properties, and applications, BoD–Books on Demand2016.

[9] Y. Huang, J. Liu, Y. Deng, Y. Qian, X. Jia, M. Ma, C. Yang, K. Liu, Z. Wang, S. Qu, The application of perovskite materials in solar water splitting, Journal of Semiconductors, 41 (2020) 011701.

[10] T. Wu, W. Pisula, M.Y.A. Rashid, P. Gao, Application of Perovskite-Structured Materials in Field-Effect Transistors, Advanced Electronic Materials, 5 (2019) 1900444.

[11] A. Bhalla, R. Guo, R. Roy, The perovskite structure—a review of its role in ceramic science and technology, Materials research innovations, 4 (2000) 3-26.

[12] J.S. Lee, Photocatalytic water splitting under visible light with particulate semiconductor catalysts, Catalysis Surveys from Asia, 9 (2005) 217-227.

[13] O. Amiri, K. Salar, P. Othman, T. Rasul, D. Faiq, M. Saadat, Purification of wastewater by the piezo-catalyst effect of PbTiO3 nanostructures under ultrasonic vibration, Journal of hazardous materials, 394 (2020) 122514.

[14] Y. Chen, X. Deng, J. Wen, J. Zhu, Z. Bian, Piezo-promoted the generation of reactive oxygen species and the photodegradation of organic pollutants, Applied Catalysis B: Environmental, 258 (2019) 118024.

[15] J. Feng, J. Sun, X. Liu, J. Zhu, Y. Xiong, S. Tian, Enhancement and mechanism of nano-BaTiO 3 piezocatalytic degradation of tricyclazole by co-loading Pt and RuO 2, Environmental Science: Nano, 6 (2019) 2241-2252.

[16] D. Liu, Y. Song, Z. Xin, G. Liu, C. Jin, F. Shan, High-piezocatalytic performance of eco-friendly

(Bi1/2Na1/2) TiO3-based nanofibers by electrospinning, Nano Energy, 65 (2019) 104024.
[17] K.P. Singh, G. Singh, R. Vaish, Utilizing the localized surface piezoelectricity of centrosymmetric Sr1-xFexTiO3 (x≤ 0.2) ceramics for piezocatalytic dye degradation, Journal of the European Ceramic Society, 41 (2021) 326-334.
[18] Z.-X. Chen, Y. Chen, Y.-S. Jiang, Comparative study of abo3 perovskite compounds. 1. ATiO3 (A= Ca, Sr, Ba, and Pb) perovskites, The Journal of Physical Chemistry B, 106 (2002) 9986-9992.
[19] E. Lin, J. Wu, N. Qin, B. Yuan, Z. Kang, D. Bao, Enhanced piezocatalytic, photocatalytic and piezo-/photocatalytic performance of diphasic Ba 1− x Ca x TiO 3 nanowires near a solubility limit, Catalysis Science & Technology, 9 (2019) 6863-6874.
[20] C. Jin, D. Liu, J. Hu, Y. Wang, Q. Zhang, L. Lv, F. Zhuge, The role of microstructure in piezocatalytic degradation of organic dye pollutants in wastewater, Nano Energy, 59 (2019) 372-379.
[21] P. Wang, X. Li, S. Fan, X. Chen, M. Qin, D. Long, M.O. Tadé, S. Liu, Impact of oxygen vacancy occupancy on piezo-catalytic activity of BaTiO3 nanobelt, Applied Catalysis B: Environmental, 279 (2020) 119340.
[22] D. Liu, C. Jin, F. Shan, J. He, F. Wang, Synthesizing BaTiO3 nanostructures to explore morphological influence, kinetics, and mechanism of piezocatalytic dye degradation, ACS applied materials & interfaces, 12 (2020) 17443-17451.
[23] B. Yuan, J. Wu, N. Qin, E. Lin, D. Bao, Enhanced piezocatalytic performance of (Ba, Sr) TiO3 nanowires to degrade organic pollutants, ACS Applied Nano Materials, 1 (2018) 5119-5127.
[24] Z. Zhao, L. Wei, S. Li, L. Zhu, Y. Su, Y. Liu, Y. Bu, Y. Lin, W. Liu, Z. Zhang, Exclusive enhancement of catalytic activity in Bi 0.5 Na 0.5 TiO 3 nanostructures: new insights into the design of efficient piezocatalysts and piezo-photocatalysts, Journal of Materials Chemistry A, 8 (2020) 16238-16245.
[25] A. Das, D. Mahata, M.K. Adak, Perovskite Based Photocatalyst for Wastewater Treatment: Green Approach of Environmental Sustainability, American Journal of Biological and Environmental Statistics, 7 (2021) 1-8.
[26] C. Sun, J.A. Alonso, J. Bian, Recent advances in perovskite-type oxides for energy conversion and storage applications, Advanced Energy Materials, 11 (2021) 2000459.
[27] K. Maeda, Rhodium-doped barium titanate perovskite as a stable p-type semiconductor photocatalyst for hydrogen evolution under visible light, ACS applied materials & interfaces, 6 (2014) 2167-2173.
[28] Y.W. Teh, M.K. Chee, X.Y. Kong, S.-T. Yong, S.-P. Chai, An insight into perovskite-based photocatalysts for artificial photosynthesis, Sustainable Energy & Fuels, 4 (2020) 973-984.
[29] P. Kanhere, Z. Chen, A review on visible light active perovskite-based photocatalysts, Molecules, 19 (2014) 19995-20022.
[30] Y. Wang, M. Zhang, J. Liu, H. Zhang, F. Li, C.W. Tseng, B. Yang, G. Smith, J. Zhai, Z. Zhang, Domain Wall Free Polar Structure Enhanced Photodegradation Activity in Nanoscale Ferroelectric BaxSr1-xTiO3, Advanced Energy Materials, 10 (2020) 2001802.
[31] X. Zhang, K. Huo, L. Hu, Z. Wu, P.K. Chu, Synthesis and photocatalytic activity of highly ordered TiO2 and SrTiO3/TiO2 nanotube arrays on Ti substrates, Journal of the American Ceramic Society, 93 (2010) 2771-2778.
[32] Y. Fang, X. Kong, D. Wang, J. Liu, S. Cui, First principle calculations of electronic, band structural, and optical properties of BixSr1-xTiO3 perovskite, Journal of Physics and Chemistry of Solids, 127 (2019) 107-114.

[33] X. Liu, L. Xiao, Y. Zhang, H. Sun, Significantly enhanced piezo-photocatalytic capability in BaTiO3 nanowires for degrading organic dye, Journal of Materiomics, 6 (2020) 256-262.
[34] X. Huang, R. Lei, J. Yuan, F. Gao, C. Jiang, W. Feng, J. Zhuang, P. Liu, Insight into the piezo-photo coupling effect of PbTiO3/CdS composites for piezo-photocatalytic hydrogen production, Applied Catalysis B: Environmental, 282 (2021) 119586.
[35] R. Zhang, X. Wu, Y. Li, W. Shao, Y. Zhang, Z. Liu, J. Nie, J. Tan, W. Ye, Enhanced piezo-photocatalytic performance by piezoelectric and visible light photoexcitation coupling through piezoelectric Na 0.5 Bi 0.5 TiO 3 micron crystals, RSC Advances, 10 (2020) 7443-7451.
[36] M. Sharma, A. Halder, R. Vaish, Effect of Ce on piezo/photocatalytic effects of Ba0. 9Ca0. 1CexTi1-xO3 ceramics for dye/pharmaceutical waste water treatment, Materials Research Bulletin, 122 (2020) 110647.
[37] J.S. Forrester, J.S. Zobec, D. Phelan, E.H. Kisi, Synthesis of PbTiO3 ceramics using mechanical alloying and solid state sintering, Journal of Solid State Chemistry, 177 (2004) 3553-3559.
[38] S. Shao, J. Zhang, Z. Zhang, P. Zheng, M. Zhao, J. Li, C. Wang, High piezoelectric properties and domain configuration in BaTiO3 ceramics obtained through the solid-state reaction route, Journal of Physics D: Applied Physics, 41 (2008) 125408.
[39] L. Cavalcante, V. Marques, J. Sczancoski, M. Escote, M. Joya, J.A. Varela, M. Santos, P. Pizani, E. Longo, Synthesis, structural refinement and optical behavior of CaTiO3 powders: A comparative study of processing in different furnaces, Chemical Engineering Journal, 143 (2008) 299-307.
[40] X.-L. Shi, H. Wu, Q. Liu, W. Zhou, S. Lu, Z. Shao, M. Dargusch, Z.-G. Chen, SrTiO3-based thermoelectrics: Progress and challenges, Nano Energy, (2020) 105195.
[41] B. Noheda, D. Cox, G. Shirane, R. Guo, B. Jones, L. Cross, Stability of the monoclinic phase in the ferroelectric perovskite PbZr 1− x Ti x O 3, Physical Review B, 63 (2000) 014103.
[42] L. Kong, J. Ma, W. Zhu, O. Tan, Preparation and characterization of PLZT ceramics using high-energy ball milling, Journal of alloys and compounds, 322 (2001) 290-297.
[43] P.B. Groszewicz, M. Gröting, H. Breitzke, W. Jo, K. Albe, G. Buntkowsky, J. Rödel, Reconciling local structure disorder and the relaxor state in (Bi 1/2 Na 1/2) TiO 3-BaTiO 3, Scientific reports, 6 (2016) 1-11.
[44] S. Jo, C.-H. Hong, D.S. Kim, H.-W. Kang, C.W. Ahn, H.-G. Lee, S. Nahm, W. Jo, S.H. Han, Phase transition behavior and mechanical properties of (1-x)(Bi1/2Na1/2) TiO3-xSrTiO3 lead-free piezoelectric ceramics, Sensors and Actuators A: Physical, 258 (2017) 201-207.
[45] A. Molak, A. Winiarski, A.Z. Szeremeta, D.K. Mahato, J. Macutkevic, I. Gruszka, S. Miga, J. Koperski, E. Palaimiene, S. Pawlus, Electrical features of ferroelectric (Ba0. 83Ca0. 17) TiO3 ceramics with diffused phase transition under pressure, Journal of Alloys and Compounds, 856 (2021) 158216.
[46] A. Berenov, F. Le Goupil, N. Alford, Effect of ionic radii on the Curie temperature in Ba 1-xy Sr x Ca y TiO 3 compounds, Scientific reports, 6 (2016) 1-10.
[47] S. Patel, K. Srikanth, S. Steiner, R. Vaish, T. Froemling, Pyroelectric and impedance studies of the 0.5 Ba (Zr0. 2Ti0. 8) O3-0.5 (Ba0. 7Sr0. 3) TiO3 ceramics, Ceramics International, 44 (2018) 21976-21981.
[48] H.-T. Kim, J.-H. Ji, B.S. Kim, J.-H. Koh, Strain related curie temperature and improved piezoelectric properties of lead-free (1-x) Ba (Sn, Ti) O3-x (Ba, Ca) TiO3 ceramics, Ceramics International, 46 (2020) 25050-25057.
[49] G.-J. Lee, E.-K. Park, S.-A. Yang, J.-J. Park, S.-D. Bu, M.-K. Lee, Rapid and direct synthesis of

complex perovskite oxides through a highly energetic planetary milling, Scientific reports, 7 (2017) 1-11.
[50] W. Shi, S. Song, H. Zhang, Hydrothermal synthetic strategies of inorganic semiconducting nanostructures, Chemical Society Reviews, 42 (2013) 5714-5743.
[51] G. Canu, V. Buscaglia, Hydrothermal synthesis of strontium titanate: thermodynamic considerations, morphology control and crystallisation mechanisms, CrystEngComm, 19 (2017) 3867-3891.
[52] K. Fujinami, K. Katagiri, J. Kamiya, T. Hamanaka, K. Koumoto, Sub-10 nm strontium titanate nanocubes highly dispersed in non-polar organic solvents, Nanoscale, 2 (2010) 2080-2083.
[53] F. Dang, K.-i. Mimura, K. Kato, H. Imai, S. Wada, H. Haneda, M. Kuwabara, Growth of monodispersed SrTiO3 nanocubes by thermohydrolysis method, CrystEngComm, 13 (2011) 3878-3883.
[54] S.-T. Huang, W.W. Lee, J.-L. Chang, W.-S. Huang, S.-Y. Chou, C.-C. Chen, Hydrothermal synthesis of SrTiO3 nanocubes: Characterization, photocatalytic activities, and degradation pathway, Journal of the Taiwan Institute of Chemical Engineers, 45 (2014) 1927-1936.
[55] W.W. Lee, W.-H. Chung, W.-S. Huang, W.-C. Lin, W.-Y. Lin, Y.-R. Jiang, C.-C. Chen, Photocatalytic activity and mechanism of nano-cubic barium titanate prepared by a hydrothermal method, Journal of the Taiwan Institute of Chemical Engineers, 44 (2013) 660-669.
[56] T. Kimijima, K. Kanie, M. Nakaya, A. Muramatsu, Hydrothermal synthesis of size-and shape-controlled CaTiO 3 fine particles and their photocatalytic activity, CrystEngComm, 16 (2014) 5591-5597.
[57] D. Li, J.T. McCann, Y. Xia, M. Marquez, Electrospinning: a simple and versatile technique for producing ceramic nanofibers and nanotubes, Journal of the American Ceramic Society, 89 (2006) 1861-1869.
[58] W. Sigmund, J. Yuh, H. Park, V. Maneeratana, G. Pyrgiotakis, A. Daga, J. Taylor, J.C. Nino, Processing and structure relationships in electrospinning of ceramic fiber systems, Journal of the American Ceramic Society, 89 (2006) 395-407.
[59] B. Sahoo, P. Panda, Preparation and characterization of barium titanate nanofibers by electrospinning, Ceramics International, 38 (2012) 5189-5193.
[60] S. Choi, J. Park, J. Kang, S.W. Koh, Y.C. Kang, Synthesis and characterization of lead zirconate titanate nanofibers obtained by electrospinning, Bulletin of the Korean Chemical Society, 36 (2015) 1594-1598.
[61] N. Bhardwaj, S.C. Kundu, Electrospinning: a fascinating fiber fabrication technique, Biotechnology advances, 28 (2010) 325-347.
[62] Y. Zhang, Z. Jiang, J. Huang, L.Y. Lim, W. Li, J. Deng, D. Gong, Y. Tang, Y. Lai, Z. Chen, Titanate and titania nanostructured materials for environmental and energy applications: a review, RSC advances, 5 (2015) 79479-79510.
[63] M. Fan, W. Hui, Z. Li, Z. Shen, H. Li, A. Jiang, Y. Chen, R. Liu, Fabrication and piezoresponse of electrospun ultra-fine Pb (Zr0. 3, Ti0. 7) O3 nanofibers, Microelectronic engineering, 98 (2012) 371-373.
[64] J. Yuh, J.C. Nino, W.M. Sigmund, Synthesis of barium titanate (BaTiO3) nanofibers via electrospinning, Materials Letters, 59 (2005) 3645-3647.
[65] N. Dharmaraj, H. Park, C. Kim, H. Kim, D. Lee, Nickel titanate nanofibers by electrospinning, Materials chemistry and physics, 87 (2004) 5-9.

[66] Z. Imran, S. Batool, M. Israr, J. Sadaf, M. Usman, H. Jamil, M. Javed, M. Rafiq, M. Hasan, O. Nur, Fabrication of cadmium titanate nanofibers via electrospinning technique, Ceramics International, 38 (2012) 3361-3365.
[67] N. Dharmaraj, H. Park, B. Lee, P. Viswanathamurthi, H. Kim, D. Lee, Preparation and morphology of magnesium titanate nanofibres via electrospinning, Inorganic Chemistry Communications, 7 (2004) 431-433.
[68] T.K. Tseng, Y.S. Lin, Y.J. Chen, H. Chu, A review of photocatalysts prepared by sol-gel method for VOCs removal, International journal of molecular sciences, 11 (2010) 2336-2361.
[69] M. Parashar, V.K. Shukla, R. Singh, Metal oxides nanoparticles via sol–gel method: A review on synthesis, characterization and applications, Journal of Materials Science: Materials in Electronics, 31 (2020) 3729-3749.
[70] H. Zhao, J. Wang, L. Zhang, Y. Rong, J. Chen, K. Ibrahim, X. Xing, Effects of oxygen vacancy on the electronic structure and multiferroics in sol–gel derived Pb 0.8 Co 0.2 TiO 3 thin films, Dalton Transactions, 42 (2013) 10358-10364.
[71] Y. Wang, W. Zhang, P. Zhang, J. Li, J. Long, Effect of replacement of Ca by Zn on the structure and optical property of CaTiO3: Eu3+ red phosphor prepared by sol-gel method, Luminescence, 30 (2015) 533-537.
[72] L. Li, X. Liu, Y. Zhang, P.A. Salvador, G.S. Rohrer, Heterostructured (Ba, Sr) TiO3/TiO2 core/shell photocatalysts: influence of processing and structure on hydrogen production, international journal of hydrogen energy, 38 (2013) 6948-6959.
[73] T. Schneller, R. Waser, M. Kosec, D. Payne, Chemical solution deposition of functional oxide thin films, Springer2013.
[74] T.M. Raeder, K. Bakken, J. Glaum, M.-A. Einarsrud, T. Grande, Enhanced in-plane ferroelectricity in BaTiO3 thin films fabricated by aqueous chemical solution deposition, AIP Advances, 8 (2018) 105228.
[75] M. Christensen, M.-A. Einarsrud, T. Grande, Fabrication of lead-free Bi0. 5Na0. 5TiO3 thin films by aqueous chemical solution deposition, Materials, 10 (2017) 213.
[76] S. Sharma, M. Tomar, A. Kumar, N.K. Puri, V. Gupta, Photovoltaic effect in BiFeO3/BaTiO3 multilayer structure fabricated by chemical solution deposition technique, Journal of Physics and Chemistry of Solids, 93 (2016) 63-67.
[77] Y. Abe, R.M. Laine, Photocatalytic La4Ti3O12 nanoparticles fabricated by liquid-feed flame spray pyrolysis, Ceramics International, 46 (2020) 18656-18660.
[78] C. Oliva, S. Cappelli, I. Rossetti, A. Kryukov, L. Bonoldi, L. Forni, Effect of M ion oxidation state in Sr1− xMxTiO3±δ perovskites in methane catalytic flameless combustion, Journal of molecular catalysis A: Chemical, 245 (2006) 55-61.
[79] Y. Abe, R.M. Laine, Photocatalytic plate-like La2Ti2O7 nanoparticles synthesized via liquid-feed flame spray pyrolysis (LF-FSP) of metallo-organic precursors, Journal of the American Ceramic Society, 103 (2020) 4832-4839.
[80] L. Fabbrini, A. Kryukov, S. Cappelli, G. Chiarello, I. Rossetti, C. Oliva, L. Forni, Sr1–xAgxTiO3±δ (x= 0, 0.1) perovskite-structured catalysts for the flameless combustion of methane, Journal of Catalysis, 232 (2005) 247-256.
[81] C. Oliva, L. Bonoldi, S. Cappelli, L. Fabbrini, I. Rossetti, L. Forni, Effect of preparation parameters on SrTiO3±δ catalyst for the flameless combustion of methane, Journal of Molecular Catalysis A: Chemical, 226 (2005) 33-40.

[82] I. Rossetti, O. Buchneva, C. Biffi, R. Rizza, Effect of sulphur poisoning on perovskite catalysts prepared by flame-pyrolysis, Applied Catalysis B: Environmental, 89 (2009) 383-390.
[83] Y.-J. Chou, K.I. Sucipto, H.S. Ningsih, T. Moriga, S.-J. Shih, Inhibition of secondary phase formation with orientation-controlled SrTiO3 nanoparticles, Ceramics International, 45 (2019) 9197-9202.
[84] T.-Y. Li, K. Nakata, T. Moriga, S.-J. Shih, Modification of grain boundary structure of SrTiO3 using hydroxyl additives, Ceramics International, 44 (2018) 3960-3965.
[85] S. Lanfredi, E. Djurado, M.A. Nobre, Preparation and Physical Chemistry Characterization of New Nanostructured Oxides Catalysts by Spray Pyrolysis Method for the Biodiesel Production, Materials Science Forum, Trans Tech Publ, 2018, pp. 7-11.
[86] W. Nimmo, N.J. Ali, R. Brydson, C. Calvert, S.J. Milne, Particle formation during spray pyrolysis of lead zirconate titanate, Journal of the American Ceramic Society, 88 (2005) 839-844.
[87] R.P. Singh, Conventional and microwave synthesis of mesoporous calcium titanate nanopowders: a comparative study, Journal of Sol-Gel Science and Technology, 88 (2018) 574-583.
[88] B.L. Phoon, C.W. Lai, J.C. Juan, P.L. Show, W.H. Chen, A review of synthesis and morphology of SrTiO 3 for energy and other applications, International Journal of Energy Research, 43 (2019) 5151-5174.
[89] Y. Liu, L. Xie, Y. Li, R. Yang, J. Qu, Y. Li, X. Li, Synthesis and high photocatalytic hydrogen production of SrTiO3 nanoparticles from water splitting under UV irradiation, Journal of Power Sources, 183 (2008) 701-707.
[90] U. Sulaeman, S. Yin, T. Sato, Solvothermal synthesis and photocatalytic properties of nitrogen-doped SrTiO3 nanoparticles, Journal of Nanomaterials, 2010 (2010).
[91] A. Souza, G. Santos, B. Barra, W. Macedo Jr, S. Teixeira, C. Santos, A. Senos, L. Amaral, E. Longo, Photoluminescence of SrTiO3: influence of particle size and morphology, Crystal growth & design, 12 (2012) 5671-5679.
[92] K. Nakashima, M. Kera, I. Fujii, S. Wada, A new approach for the preparation of SrTiO3 nanocubes, Ceramics International, 39 (2013) 3231-3234.
[93] T. Kimijima, K. Kanie, M. Nakaya, A. Muramatsu, Solvothermal synthesis of SrTiO3 nanoparticles precisely controlled in surface crystal planes and their photocatalytic activity, Applied Catalysis B: Environmental, 144 (2014) 462-467.
[94] W. Zhao, N. Liu, H. Wang, L. Mao, Sacrificial template synthesis of core-shell SrTiO3/TiO2 heterostructured microspheres photocatalyst, Ceramics International, 43 (2017) 4807-4813.
[95] D. Hou, X. Hu, W. Ho, P. Hu, Y. Huang, Facile fabrication of porous Cr-doped SrTiO 3 nanotubes by electrospinning and their enhanced visible-light-driven photocatalytic properties, Journal of Materials Chemistry A, 3 (2015) 3935-3943.
[96] B. Jiang, J. Iocozzia, L. Zhao, H. Zhang, Y.-W. Harn, Y. Chen, Z. Lin, Barium titanate at the nanoscale: controlled synthesis and dielectric and ferroelectric properties, Chemical Society Reviews, 48 (2019) 1194-1228.
[97] J. Hong, D. Fang, Size-dependent ferroelectric behaviors of Ba Ti O 3 nanowires, Applied Physics Letters, 92 (2008) 012906.
[98] Z. Zhao, V. Buscaglia, M. Viviani, M.T. Buscaglia, L. Mitoseriu, A. Testino, M. Nygren, M. Johnsson, P. Nanni, Grain-size effects on the ferroelectric behavior of dense nanocrystalline BaTiO 3 ceramics, Physical Review B, 70 (2004) 024107.

[99] M.B. Ghasemian, Q. Lin, E. Adabifiroozjaei, F. Wang, D. Chu, D. Wang, Morphology control and large piezoresponse of hydrothermally synthesized lead-free piezoelectric (Bi 0.5 Na 0.5) TiO 3 nanofibres, RSC Advances, 7 (2017) 15020-15026.
[100] E.W. Shi, C.T. Xia, W.Z. Zhong, B.G. Wang, C.D. Feng, Crystallographic properties of hydrothermal barium titanate crystallites, Journal of the American Ceramic Society, 80 (1997) 1567-1572.
[101] N.H. Yusoff, R.A.M. Osman, M.S. Idris, K.N.D.K. Muhsen, N.I.M. Nor, Dielectric and structural analysis of hexagonal and tetragonal phase BaTiO3, AIP Conference Proceedings, AIP Publishing LLC, 2020, pp. 020038.
[102] D. Demydov, K.J. Klabunde, Characterization of mixed metal oxides (SrTiO3 and BaTiO3) synthesized by a modified aerogel procedure, Journal of non-crystalline solids, 350 (2004) 165-172.
[103] X. Zhou, C. Jiang, C. Chen, H. Luo, K. Zhou, D. Zhang, Morphology control and piezoelectric response of Na 0.5 Bi 0.5 TiO 3 synthesized via a hydrothermal method, CrystEngComm, 18 (2016) 1302-1310.
[104] C. Hérard, A. Faivre, J. Lemaître, Surface decontamination treatments of undoped BaTiO3—part I: powder and green body properties, Journal of the European Ceramic Society, 15 (1995) 135-143.
[105] C. Miot, E. Husson, C. Proust, R. Erre, J. Coutures, X-ray photoelectron spectroscopy characterization of barium titanate ceramics prepared by the citric route. Residual carbon study, Journal of materials research, 12 (1997) 2388-2392.
[106] M.d.C.B. López, G. Fourlaris, B. Rand, F.L. Riley, Characterization of barium titanate powders: barium carbonate identification, Journal of the American Ceramic Society, 82 (1999) 1777-1786.
[107] M. Viviani, M. Buscaglia, P. Nanni, R. Parodi, G. Gemme, A. Dacca, XPS investigation of surface properties of Ba (1-x) SrxTiO3 powders prepared by low temperature aqueous synthesis, Journal of the European Ceramic Society, 19 (1999) 1047-1051.
[108] J. Pokorný, U. Pasha, L. Ben, O. Thakur, D. Sinclair, I. Reaney, Use of Raman spectroscopy to determine the site occupancy of dopants in BaTiO3, Journal of Applied Physics, 109 (2011) 114110.
[109] D. Rout, K.-S. Moon, V.S. Rao, S.-J.L. Kang, Study of the morphotropic phase boundary in the lead-free Na1/2Bi1/2TiO3-BaTiO3 system by Raman spectroscopy, Journal of the Ceramic Society of Japan, 117 (2009) 797-800.
[110] C.-S. Tu, I. Siny, V.H. Schmidt, Sequence of dielectric anomalies and high-temperature relaxation behavior in Na 1/2 Bi 1/2 TiO 3, Physical review B, 49 (1994) 11550.
[111] G. Jones, P. Thomas, The tetragonal phase of Na0. 5Bi0. 5TiO3–a new variant of the perovskite structure, Acta Crystallographica Section B: Structural Science, 56 (2000) 426-430.
[112] S. Köhne, O. Schirmer, H. Hesse, T.W. Kool, V. Vikhnin, Ti3+ Jahn–Teller Polarons and Bipolarons in BaTiO3, Journal of superconductivity, 12 (1999) 193-195.
[113] R. Scharfschwerdt, O. Schirmer, H. Krösz, T.W. Kool, Oxygen vacancy related defects in BaTiO3, Ferroelectrics, 185 (1996) 9-12.
[114] T. Kutty, P. Murugaraj, N. Gajbhiye, Activation of trap centres in PTC BaTiO3, Materials letters, 2 (1984) 396-400.
[115] N. Hari, P. Padmini, T.N. KUTTY, Complex impedance analyses of n-BaTiO3 ceramics showing positive temperature coefficient of resistance, Journal of Materials Science: Materials in Electronics, 8 (1997) 15-22.

[116] M.D. Glinchuk, I.P. Bykov, S.M. Kornienko, V.V. Laguta, A.M. Slipenyuk, A.G. Bilous, O.I. V'yunov, O.Z. Yanchevskii, Influence of impurities on the properties of rare-earth-doped barium-titanate ceramics, Journal of Materials Chemistry, 10 (2000) 941-947.
[117] S.s. Jida, T. Miki, Electron paramagnetic resonance of Nb-doped BaTiO3 ceramics with positive temperature coefficient of resistivity, Journal of applied physics, 80 (1996) 5234-5239.
[118] T. Miki, A. Fujimoto, S.s. Jida, An evidence of trap activation for positive temperature coefficient of resistivity in BaTiO 3 ceramics with substitutional Nb and Mn as impurities, Journal of applied physics, 83 (1998) 1592-1603.
[119] Z. Wang, J. Hu, A.P. Suryavanshi, K. Yum, M.-F. Yu, Voltage generation from individual BaTiO3 nanowires under periodic tensile mechanical load, Nano letters, 7 (2007) 2966-2969.
[120] Z. Wang, A.P. Suryavanshi, M.-F. Yu, Ferroelectric and piezoelectric behaviors of individual single crystalline Ba Ti O 3 nanowire under direct axial electric biasing, Applied physics letters, 89 (2006) 082903.
[121] Y. Zhuang, F. Li, G. Yang, Z. Xu, J. Li, B. Fu, Y. Yang, S. Zhang, Fabrication and piezoelectric property of BaTiO 3 nanofibers, Journal of the American Ceramic Society, 97 (2014) 2725-2730.
[122] N. Bao, L. Shen, A. Gupta, A. Tatarenko, G. Srinivasan, K. Yanagisawa, Size-controlled one-dimensional monocrystalline BaTiO 3 nanostructures, Applied Physics Letters, 94 (2009) 253109.
[123] K.K. Shung, J. Cannata, Q. Zhou, Piezoelectric materials for high frequency medical imaging applications: A review, Journal of Electroceramics, 19 (2007) 141-147.
[124] H. Liu, J. Zhong, C. Lee, S.-W. Lee, L. Lin, A comprehensive review on piezoelectric energy harvesting technology: Materials, mechanisms, and applications, Applied Physics Reviews, 5 (2018) 041306.
[125] K.S. Ramadan, D. Sameoto, S. Evoy, A review of piezoelectric polymers as functional materials for electromechanical transducers, Smart Materials and Structures, 23 (2014) 033001.
[126] J. Jung, W. Lee, W. Kang, E. Shin, J. Ryu, H. Choi, Review of piezoelectric micromachined ultrasonic transducers and their applications, Journal of Micromechanics and Microengineering, 27 (2017) 113001.
[127] S.B. Lang, S. Muensit, Review of some lesser-known applications of piezoelectric and pyroelectric polymers, Applied Physics A, 85 (2006) 125-134.
[128] S. Mishra, L. Unnikrishnan, S.K. Nayak, S. Mohanty, Advances in piezoelectric polymer composites for energy harvesting applications: a systematic review, Macromolecular Materials and Engineering, 304 (2019) 1800463.
[129] M. Salim, D. Salim, D. Chandran, H.S. Aljibori, A.S. Kherbeet, Review of nano piezoelectric devices in biomedicine applications, Journal of Intelligent Material Systems and Structures, 29 (2018) 2105-2121.
[130] A.F. Devonshire, XCVI. Theory of barium titanate: Part I, The London, Edinburgh, and Dublin Philosophical Magazine and Journal of Science, 40 (1949) 1040-1063.
[131] A. Devonshire, CIX. Theory of barium titanate—Part II, The London, Edinburgh, and Dublin Philosophical Magazine and Journal of Science, 42 (1951) 1065-1079.
[132] M. Acosta, N. Novak, V. Rojas, S. Patel, R. Vaish, J. Koruza, G. Rossetti Jr, J. Rödel, BaTiO3-based piezoelectrics: Fundamentals, current status, and perspectives, Applied Physics Reviews, 4 (2017) 041305.
[133] H. Jaffe, Titanate ceramics for electromechanical purposes, Industrial & Engineering Chemistry, 42 (1950) 264-268.

[134] G.H. Haertling, Ferroelectric ceramics: history and technology, Journal of the American Ceramic Society, 82 (1999) 797-818.
[135] G.H. Haertling, C.E. Land, Hot - pressed (Pb, La)(Zr, Ti) O3 ferroelectric ceramics for electrooptic applications, Journal of the American Ceramic Society, 54 (1971) 1-11.
[136] A.B. Schäufele, K. Heinz Härdtl, Ferroelastic properties of lead zirconate titanate ceramics, Journal of the American Ceramic Society, 79 (1996) 2637-2640.
[137] C. Luo, G. Cao, I. Shen, Development of a lead-zirconate-titanate (PZT) thin-film microactuator probe for intracochlear applications, Sensors and Actuators A: Physical, 201 (2013) 1-9.
[138] W.-Q. Liao, D. Zhao, Y.-Y. Tang, Y. Zhang, P.-F. Li, P.-P. Shi, X.-G. Chen, Y.-M. You, R.-G. Xiong, A molecular perovskite solid solution with piezoelectricity stronger than lead zirconate titanate, Science, 363 (2019) 1206-1210.
[139] X. Hao, J. Zhai, L.B. Kong, Z. Xu, A comprehensive review on the progress of lead zirconate-based antiferroelectric materials, Progress in materials science, 63 (2014) 1-57.
[140] T. Ibn-Mohammed, I. Reaney, S. Koh, A. Acquaye, D. Sinclair, C.A. Randall, F. Abubakar, L. Smith, G. Schileo, L. Ozawa-Meida, Life cycle assessment and environmental profile evaluation of lead-free piezoelectrics in comparison with lead zirconate titanate, Journal of the European Ceramic Society, 38 (2018) 4922-4938.
[141] G. Schileo, G. Grancini, Lead or No Lead? Availability, Toxicity, Sustainability and Environmental Impact of Lead-Free Perovskites Solar Cells, Journal of Materials Chemistry C, (2020).
[142] T. Ibn-Mohammed, S. Koh, I. Reaney, A. Acquaye, D. Wang, S. Taylor, A. Genovese, Integrated hybrid life cycle assessment and supply chain environmental profile evaluations of lead-based (lead zirconate titanate) versus lead-free (potassium sodium niobate) piezoelectric ceramics, Energy & Environmental Science, 9 (2016) 3495-3520.
[143] J. Roedel, J.-F. Li, Lead-free piezoceramics: Status and perspectives, MRS Bulletin, 43 (2018) 576-580.
[144] E. Cross, Lead-free at last, Nature, 432 (2004) 24-25.
[145] C.F. Tan, W.L. Ong, G.W. Ho, Self-biased hybrid piezoelectric-photoelectrochemical cell with photocatalytic functionalities, ACS nano, 9 (2015) 7661-7670.
[146] J. Wu, N. Qin, E. Lin, B. Yuan, Z. Kang, D. Bao, Synthesis of Bi 4 Ti 3 O 12 decussated nanoplates with enhanced piezocatalytic activity, Nanoscale, 11 (2019) 21128-21136.
[147] W. Liu, X. Ren, Large piezoelectric effect in Pb-free ceramics, Physical review letters, 103 (2009) 257602.
[148] J.A. Dawson, H. Chen, I. Tanaka, Crystal structure, defect chemistry and oxygen ion transport of the ferroelectric perovskite, Na 0.5 Bi 0.5 TiO 3: insights from first-principles calculations, Journal of Materials Chemistry A, 3 (2015) 16574-16582.
[149] N. Das, S. Kandimalla, Application of perovskites towards remediation of environmental pollutants: an overview, International Journal of Environmental Science and Technology, 14 (2017) 1559-1572.
[150] H.-M. Huang, H.-Y. Li, X.-X. Wang, X. Guo, Detecting low concentration of H2S gas by BaTiO3 nanoparticle-based sensors, Sensors and Actuators B: Chemical, 238 (2017) 16-23.
[151] Y. Zhang, H. Sun, W. Chen, A brief review of Ba (Ti0. 8Zr0. 2) O3-(Ba0. 7Ca0. 3) TiO3 based lead-free piezoelectric ceramics: past, present and future perspectives, Journal of Physics and

Chemistry of Solids, 114 (2018) 207-219.
[152] J. Wu, N. Qin, D. Bao, Effective enhancement of piezocatalytic activity of BaTiO3 nanowires under ultrasonic vibration, Nano Energy, 45 (2018) 44-51.
[153] G.T. Hwang, H. Park, J.H. Lee, S. Oh, K.I. Park, M. Byun, H. Park, G. Ahn, C.K. Jeong, K. No, Self-powered cardiac pacemaker enabled by flexible single crystalline PMN-PT piezoelectric energy harvester, Advanced materials, 26 (2014) 4880-4887.
[154] A. Bune, C. Zhu, S. Ducharme, L.M. Blinov, V.M. Fridkin, S.P. Palto, N. Petukhova, S.G. Yudin, Piezoelectric and pyroelectric properties of ferroelectric Langmuir–Blodgett polymer films, Journal of applied physics, 85 (1999) 7869-7873.
[155] D. Li, M.H. Zhao, J. Garra, A. Kolpak, A. Rappe, D. Bonnell, J. Vohs, Direct in situ determination of the polarization dependence of physisorption on ferroelectric surfaces, nature materials, 7 (2008) 473-477.
[156] R. Wang, D. Fong, F. Jiang, M. Highland, P. Fuoss, C. Thompson, A. Kolpak, J. Eastman, S. Streiffer, A. Rappe, Reversible chemical switching of a ferroelectric film, Physical review letters, 102 (2009) 047601.
[157] Y. Mi, G. Geneste, J.E. Rault, C. Mathieu, A. Pancotti, N. Barrett, Polarization dependent chemistry of ferroelectric BaTiO3 (001) domains, Journal of Physics: Condensed Matter, 24 (2012) 275901.
[158] G. Geneste, B. Dkhil, Adsorption and dissociation of H 2 O on in-plane-polarized BaTiO 3 (001) surfaces and their relation to ferroelectricity, Physical Review B, 79 (2009) 235420.
[159] H. Huang, S. Tu, X. Du, Y. Zhang, Ferroelectric spontaneous polarization steering charge carriers migration for promoting photocatalysis and molecular oxygen activation, Journal of colloid and interface science, 509 (2018) 113-122.
[160] J. Ling, K. Wang, Z. Wang, H. Huang, G. Zhang, Enhanced piezoelectric-induced catalysis of SrTiO3 nanocrystal with well-defined facets under ultrasonic vibration, Ultrasonics sonochemistry, 61 (2020) 104819.
[161] A. Kakekhani, S. Ismail-Beigi, Ferroelectric-based catalysis: switchable surface chemistry, ACS Catalysis, 5 (2015) 4537-4545.
[162] A. Benke, E. Mehner, M. Rosenkranz, E. Dmitrieva, T. Leisegang, H. Stöcker, W. Pompe, D.C. Meyer, Pyroelectrically driven• OH generation by barium titanate and palladium nanoparticles, The Journal of Physical Chemistry C, 119 (2015) 18278-18286.
[163] J. Wu, N. Qin, B. Yuan, E. Lin, D. Bao, Enhanced pyroelectric catalysis of BaTiO3 nanowires for utilizing waste heat in pollution treatment, ACS applied materials & interfaces, 10 (2018) 37963-37973.
[164] Y. Cui, J. Briscoe, S. Dunn, Effect of Ferroelectricity on Solar-Light-Driven Photocatalytic Activity of BaTiO3 Influence on the Carrier Separation and Stern Layer Formation, Chemistry of Materials, 25 (2013) 4215-4223.
[165] H. Bantawal, U.S. Shenoy, D.K. Bhat, Tuning the photocatalytic activity of SrTiO3 by varying the Sr/Ti ratio: Unusual effect of viscosity of the synthesis medium, The Journal of Physical Chemistry C, 122 (2018) 20027-20033.
[166] X. Lin, J. Xing, W. Wang, Z. Shan, F. Xu, F. Huang, Photocatalytic activities of heterojunction semiconductors Bi2O3/BaTiO3: a strategy for the design of efficient combined photocatalysts, The Journal of Physical Chemistry C, 111 (2007) 18288-18293.
[167] T. Xian, H. Yang, L. Di, J. Dai, Enhanced photocatalytic activity of BaTiO3@ g-C3N4 for the

degradation of methyl orange under simulated sunlight irradiation, Journal of Alloys and Compounds, 622 (2015) 1098-1104.
[168] T.A. Kurniawan, L. Yanyan, T. Ouyang, A.B. Albadarin, G. Walker, BaTiO3/TiO2 composite-assisted photocatalytic degradation for removal of acetaminophen from synthetic wastewater under UV–vis irradiation, Materials Science in Semiconductor Processing, 73 (2018) 42-50.
[169] K. Yoshimatsu, H. Mashiko, N. Umezawa, K. Horiba, H. Kumigashira, A. Ohtomo, Electronic Structures and Photoanodic Properties of Ilmenite-type M TiO3 Epitaxial Films (M= Mn, Fe, Co, Ni), The Journal of Physical Chemistry C, 121 (2017) 18717-18724.
[170] X. Zhou, J. Shi, C. Li, Effect of metal doping on electronic structure and visible light absorption of SrTiO3 and NaTaO3 (Metal= Mn, Fe, and Co), The Journal of Physical Chemistry C, 115 (2011) 8305-8311.
[171] H. Irie, Y. Maruyama, K. Hashimoto, Ag+-and Pb2+-doped SrTiO3 photocatalysts. A correlation between band structure and photocatalytic activity, The Journal of Physical Chemistry C, 111 (2007) 1847-1852.
[172] P. Suresh, P. Mathiyalagan, K. Srikanth, Structural, ferroelectric and photocatalytic performance of Ba1-xCaxTiO3 ceramics, Ferroelectrics, 555 (2020) 74-87.
[173] H. Kushwaha, A. Halder, D. Jain, R. Vaish, Visible light-induced photocatalytic and antibacterial activity of Li-doped Bi 0.5 Na 0.45 K 0.5 TiO 3–BaTiO 3 ferroelectric ceramics, Journal of Electronic Materials, 44 (2015) 4334-4342.
[174] H. Xiao, C. Luo, G. Huangfu, Y. Guo, Boosting the Photocatalytic Ability of Band-gap Engineered (Na0. 5Bi0. 5) TiO3-BaTiO3 by N-Ni Co-doping, The Journal of Physical Chemistry C, (2020).
[175] S. Song, L. Xu, Z. He, H. Ying, J. Chen, X. Xiao, B. Yan, Photocatalytic degradation of CI Direct Red 23 in aqueous solutions under UV irradiation using SrTiO3/CeO2 composite as the catalyst, Journal of Hazardous materials, 152 (2008) 1301-1308.
[176] M. Rioult, S. Datta, D. Stanescu, S. Stanescu, R. Belkhou, F. Maccherozzi, H. Magnan, A. Barbier, Tailoring the photocurrent in BaTiO3/Nb: SrTiO3 photoanodes by controlled ferroelectric polarization, Applied Physics Letters, 107 (2015) 103901.
[177] L. Li, Y. Zhang, A.M. Schultz, X. Liu, P.A. Salvador, G.S. Rohrer, Visible light photochemical activity of heterostructured PbTiO 3–TiO 2 core–shell particles, Catalysis Science & Technology, 2 (2012) 1945-1952.
[178] J. Li, F. Wang, L. Meng, M. Han, Y. Guo, C. Sun, Controlled synthesis of BiVO4/SrTiO3 composite with enhanced sunlight-driven photofunctions for sulfamethoxazole removal, Journal of colloid and interface science, 485 (2017) 116-122.
[179] J. Kong, Z. Rui, H. Ji, Carbon nitride polymer sensitization and nitrogen doping of SrTiO3/TiO2 nanotube heterostructure toward high visible light photocatalytic performance, Industrial & Engineering Chemistry Research, 56 (2017) 9999-10008.
[180] C. Zhen, C.Y. Jimmy, G. Liu, H.-M. Cheng, Selective deposition of redox co-catalyst (s) to improve the photocatalytic activity of single-domain ferroelectric PbTiO 3 nanoplates, Chemical Communications, 50 (2014) 10416-10419.
[181] R. Djellabi, M.F. Ghorab, A. Smara, C.L. Bianchi, G. Cerrato, X. Zhao, B. Yang, Titania–Montmorillonite for the photocatalytic removal of contaminants from water: adsorb & shuttle process, Green materials for wastewater treatment, Springer2020, pp. 291-319.
[182] H. Bantawal, M. Sethi, U.S. Shenoy, D.K. Bhat, Porous Graphene Wrapped SrTiO3

Nanocomposite: Sr–C Bond as an Effective Coadjutant for High Performance Photocatalytic Degradation of Methylene Blue, ACS Applied Nano Materials, 2 (2019) 6629-6636.
[183] R. Djellabi, B. Yang, Y. Wang, X. Cui, X. Zhao, Carbonaceous biomass-titania composites with TiOC bonding bridge for efficient photocatalytic reduction of Cr (VI) under narrow visible light, Chemical Engineering Journal, 366 (2019) 172-180.
[184] R. Djellabi, B. Yang, K. Xiao, Y. Gong, D. Cao, H.M.A. Sharif, X. Zhao, C. Zhu, J. Zhang, Unravelling the mechanistic role of TiOC bonding bridge at titania/lignocellulosic biomass interface for Cr (VI) photoreduction under visible light, Journal of colloid and interface science, 553 (2019) 409-417.
[185] Y. Ma, H. Luo, R. Guo, K. Zhou, D. Zhang, Enhanced performance in multilayer-structured nanocomposites using BaTiO3 and Ba0. 8Sr0. 2TiO3 decorated graphene hybrids, Ceramics International, 44 (2018) 20871-20876.
[186] J. Yan, Y.G. Jeong, Roles of carbon nanotube and BaTiO3 nanofiber in the electrical, dielectric and piezoelectric properties of flexible nanocomposite generators, Composites Science and Technology, 144 (2017) 1-10.
[187] J.D. Baran, C. Eames, K. Takahashi, M. Molinari, M.S. Islam, S.C. Parker, Structural, Electronic, and Transport Properties of Hybrid SrTiO3-Graphene and Carbon Nanoribbon Interfaces, Chemistry of Materials, 29 (2017) 7364-7370.
[188] T.R. Sobahi, M. Amin, Photocatalytic oxidation of atrazine using BaTiO3-MWCNT nanocomposites under visible light, Ceramics International, (2021).
[189] P. Senthilkumar, D.A. Jency, T. Kavinkumar, D. Dhayanithi, S. Dhanuskodi, M. Umadevi, S. Manivannan, N. Giridharan, V. Thiagarajan, M. Sriramkumar, Built-in electric field assisted photocatalytic dye degradation and photoelectrochemical water splitting of ferroelectric Ce doped BaTiO3 nanoassemblies, ACS Sustainable Chemistry & Engineering, 7 (2019) 12032-12043.
[190] H. Li, Y. Sang, S. Chang, X. Huang, Y. Zhang, R. Yang, H. Jiang, H. Liu, Z.L. Wang, Enhanced ferroelectric-nanocrystal-based hybrid photocatalysis by ultrasonic-wave-generated piezophototronic effect, Nano letters, 15 (2015) 2372-2379.
[191] Y.F. Cui, J. Briscoe, S. Dunn, An investigation into the effect of ferroelectricity of BaTiO3 on the photocatalytic activity in dye decolourisation, Advances in Science and Technology, Trans Tech Publ, 2014, pp. 190-195.
[192] J. Liu, Y. Sun, Z. Li, Ag loaded flower-like BaTiO 3 nanotube arrays: fabrication and enhanced photocatalytic property, CrystEngComm, 14 (2012) 1473-1478.
[193] L.H. Bac, N. Van Chinh, N.T. Khoa, D. Van Thiet, T. Van Trung, D.D. Dung, Tailoring the structural, optical properties and photocatalytic behavior of ferroelectric Bi0. 5K0. 5TiO3 nanopowders, Materials Letters, 164 (2016) 631-635.
[194] X. Xu, Z. Wu, L. Xiao, Y. Jia, J. Ma, F. Wang, L. Wang, M. Wang, H. Huang, Strong piezo-electro-chemical effect of piezoelectric BaTiO3 nanofibers for vibration-catalysis, Journal of Alloys and Compounds, 762 (2018) 915-921.
[195] X.-J. Wen, C.-G. Niu, L. Zhang, C. Liang, G.-M. Zeng, An in depth mechanism insight of the degradation of multiple refractory pollutants via a novel SrTiO3/BiOI heterojunction photocatalysts, Journal of Catalysis, 356 (2017) 283-299.
[196] P. Eghbali, A. Hassani, B. Sündü, Ö. Metin, Strontium titanate nanocubes assembled on mesoporous graphitic carbon nitride (SrTiO3/mpg-C3N4): Preparation, characterization and catalytic performance, Journal of Molecular Liquids, 290 (2019) 111208.

[197] J. Qiao, H. Zhang, G. Li, S. Li, Z. Qu, M. Zhang, J. Wang, Y. Song, Fabrication of a novel Z-scheme SrTiO3/Ag2S/CoWO4 composite and its application in sonocatalytic degradation of tetracyclines, Separation and Purification Technology, 211 (2019) 843-856.
[198] M. Ahmadi, M.S. Dorraji, M. Rasoulifard, A. Amani-Ghadim, The effective role of reduced-graphene oxide in visible light photocatalytic activity of wide band gap SrTiO3 semiconductor, Separation and Purification Technology, 228 (2019) 115771.
[199] U.S. Shenoy, H. Bantawal, D.K. Bhat, Band engineering of SrTiO3: effect of synthetic technique and site occupancy of doped rhodium, The Journal of Physical Chemistry C, 122 (2018) 27567-27574.
[200] K.-S. Hong, H. Xu, H. Konishi, X. Li, Piezoelectrochemical effect: a new mechanism for azo dye decolorization in aqueous solution through vibrating piezoelectric microfibers, The Journal of Physical Chemistry C, 116 (2012) 13045-13051.
[201] J. Cao, Y. Ji, C. Tian, Z. Yi, Synthesis and enhancement of visible light activities of nitrogen-doped BaTiO3, Journal of alloys and compounds, 615 (2014) 243-248.
[202] S. Lan, J. Feng, Y. Xiong, S. Tian, S. Liu, L. Kong, Performance and mechanism of piezo-catalytic degradation of 4-chlorophenol: finding of effective piezo-dechlorination, Environmental science & technology, 51 (2017) 6560-6569.
[203] T. Puangpetch, T. Sreethawong, S. Yoshikawa, S. Chavadej, Synthesis and photocatalytic activity in methyl orange degradation of mesoporous-assembled SrTiO3 nanocrystals prepared by sol–gel method with the aid of structure-directing surfactant, Journal of Molecular Catalysis A: Chemical, 287 (2008) 70-79.
[204] M. Bradha, T. Vijayaraghavan, S. Suriyaraj, R. Selvakumar, A.M. Ashok, Synthesis of photocatalytic La (1–x) AxTiO3. 5–δ (A= Ba, Sr, Ca) nano perovskites and their application for photocatalytic oxidation of congo red dye in aqueous solution, Journal of Rare Earths, 33 (2015) 160-167.
[205] Q. Li, R. Li, L. Zong, J. He, X. Wang, J. Yang, Photoelectrochemical and photocatalytic properties of Ag-loaded BaTiO3/TiO2 heterostructure nanotube arrays, International journal of hydrogen energy, 38 (2013) 12977-12983.
[206] S. Abhinay, P. Tarai, R. Mazumder, Preparation and characterization of (Ba 0.85 Ca 0.15)(Zr 0.1 Ti 0.9) TiO 3 (BCZT)/Bi 2 O 3 composites as efficient visible-light-responsive photocatalysts, Journal of Materials Science, 55 (2020) 1904-1914.
[207] Y. Cui, J. Briscoe, Y. Wang, N.V. Tarakina, S. Dunn, Enhanced photocatalytic activity of heterostructured ferroelectric BaTiO3/α-Fe2O3 and the significance of interface morphology control, ACS applied materials & interfaces, 9 (2017) 24518-24526.
[208] C. Bianchi, B. Bresolin, R. Djellabi, G. Cerrato, S. Rtimi, V. Capucci, Continuous Photocatalytic Antibacterial Activity of AgNPs doped TiO2 Digital Printed on Commercial Porcelain-grès Tiles, International Symposium on Eco-materials Processing and Design-ISEPD, 2020.
[209] K. Xie, Z. Zhou, Y. Guo, L. Wang, G. Li, S. Zhao, X. Liu, J. Li, W. Jiang, S. Wu, Long-Term Prevention of Bacterial Infection and Enhanced Osteoinductivity of a Hybrid Coating with Selective Silver Toxicity, Advanced healthcare materials, 8 (2019) 1801465.
[210] C. Shuai, G. Liu, Y. Yang, F. Qi, S. Peng, W. Yang, C. He, G. Wang, G. Qian, A strawberry-like Ag-decorated barium titanate enhances piezoelectric and antibacterial activities of polymer scaffold, Nano Energy, (2020) 104825.
[211] M.D. Wadge, B.W. Stuart, K.G. Thomas, D.M. Grant, Generation and characterisation of

gallium titanate surfaces through hydrothermal ion-exchange processes, Materials & Design, 155 (2018) 264-277.
[212] Y. Yamaguchi, S. Usuki, Y. Kanai, K. Yamatoya, N. Suzuki, K.-i. Katsumata, C. Terashima, T. Suzuki, A. Fujishima, H. Sakai, Selective inactivation of bacteriophage in the presence of bacteria by use of ground Rh-doped SrTiO3 photocatalyst and visible light, ACS applied materials & interfaces, 9 (2017) 31393-31400.
[213] S. Kumar, M. Sharma, S. Powar, E. Kabachkov, R. Vaish, Impact of remnant surface polarization on photocatalytic and antibacterial performance of BaTiO3, Journal of the European Ceramic Society, 39 (2019) 2915-2922.
[214] O. Jongprateep, N. Sato, R. Techapiesancharoenkij, K. Surawathanawises, P. Siwayaprahm, P. Watthanarat, Photocatalytic and antimicrobial activities of Sr x Ca (1-x) TiO 3 (x= 0, 0.25, 0.5, 0.75 and 1) powders synthesized by solution combustion technique, Journal of Metals, Materials and Minerals, 29 (2019).
[215] S. Raja, D. Bheeman, R. Rajamani, S. Pattiyappan, S. Sugamaran, C.S. Bellan, Synthesis, characterization and remedial aspect of BaTiO3 nanoparticles against bacteria, Nanomedicine and Nanobiology, 2 (2015) 16-20.
[216] A.A. Shah, A. Khan, S. Dwivedi, J. Musarrat, A. Azam, Antibacterial and antibiofilm activity of barium titanate nanoparticles, Materials Letters, 229 (2018) 130-133.
[217] S. Mohseni, M. Aghayan, A. Ghorani-Azam, M. Behdani, A. Asoodeh, Evaluation of antibacterial properties of Barium Zirconate Titanate (BZT) nanoparticle, Brazilian Journal of Microbiology, 45 (2014) 1393-1399.
[218] Y. Chen, A. Gao, L. Bai, Y. Wang, X. Wang, X. Zhang, X. Huang, R. Hang, B. Tang, P.K. Chu, Antibacterial, osteogenic, and angiogenic activities of SrTiO3 nanotubes embedded with Ag2O nanoparticles, Materials Science and Engineering: C, 75 (2017) 1049-1058.
[219] H. Qiao, C. Zhang, X. Dang, H. Yang, Y. Wang, Y. Chen, L. Ma, S. Han, H. Lin, X. Zhang, Gallium loading into a polydopamine-functionalised SrTiO3 nanotube with combined osteoinductive and antimicrobial activities, Ceramics International, 45 (2019) 22183-22195.
[220] R. Joy, S. Haridas, Strontuim titanate aided water splitting: An overview of current scenario, International Journal of Hydrogen Energy, (2020).
[221] H.W. Kang, S.B. Park, Effects of Mo sources on Mo doped SrTiO3 powder prepared by spray pyrolysis for H2 evolution under visible light irradiation, Materials Science and Engineering: B, 211 (2016) 67-74.
[222] T. Puangpetch, T. Sreethawong, S. Yoshikawa, S. Chavadej, Hydrogen production from photocatalytic water splitting over mesoporous-assembled SrTiO3 nanocrystal-based photocatalysts, Journal of Molecular Catalysis A: Chemical, 312 (2009) 97-106.
[223] I. Rossetti, A. Villa, M. Compagnoni, L. Prati, G. Ramis, C. Pirola, C. Bianchi, W. Wang, D. Wang, CO 2 photoconversion to fuels under high pressure: effect of TiO 2 phase and of unconventional reaction conditions, Catalysis Science & Technology, 5 (2015) 4481-4487.
[224] A. Olivo, E. Ghedini, M. Signoretto, M. Compagnoni, I. Rossetti, Liquid vs. gas phase CO2 photoreduction process: which is the effect of the reaction medium?, Energies, 10 (2017) 1394.
[225] T. Puangpetch, T. Sreethawong, S. Chavadej, Hydrogen production over metal-loaded mesoporous-assembled SrTiO3 nanocrystal photocatalysts: effects of metal type and loading, International Journal of Hydrogen Energy, 35 (2010) 6531-6540.
[226] D.V. Bavykin, F.C. Walsh, Elongated titanate nanostructures and their applications, European

Journal of Inorganic Chemistry, 2009 (2009) 977-997.
[227] R. Ma, Y. Bando, T. Sasaki, Directly rolling nanosheets into nanotubes, The Journal of Physical Chemistry B, 108 (2004) 2115-2119.
[228] D.V. Bavykin, A.N. Kulak, F.C. Walsh, Metastable nature of titanate nanotubes in an alkaline environment, Crystal growth & design, 10 (2010) 4421-4427.
[229] Z.-Y. Yuan, B.-L. Su, Titanium oxide nanotubes, nanofibers and nanowires, Colloids and Surfaces A: Physicochemical and Engineering Aspects, 241 (2004) 173-183.
[230] F. Cheng, Z. Tao, J. Liang, J. Chen, Template-directed materials for rechargeable lithium-ion batteries, Chemistry of Materials, 20 (2008) 667-681.
[231] Q. Kang, T. Wang, P. Li, L. Liu, K. Chang, M. Li, J. Ye, Photocatalytic reduction of carbon dioxide by hydrous hydrazine over Au–Cu alloy nanoparticles supported on SrTiO3/TiO2 coaxial nanotube arrays, Angewandte Chemie, 127 (2015) 855-859.
[232] T. Baran, S. Wojtyła, A. Vertova, A. Minguzzi, S. Rondinini, Photoelectrochemical and photocatalytic systems based on titanates for hydrogen peroxide formation, Journal of Electroanalytical Chemistry, 808 (2018) 395-402.
[233] Y. Fo, M. Wang, Y. Ma, H. Dong, X. Zhou, Origin of highly efficient photocatalyst NiO/SrTiO3 for overall water splitting: Insights from density functional theory calculations, Journal of Solid State Chemistry, 292 (2020) 121683.
[234] Q. Gao, J. Meng, Y. Yang, Q. Lin, Y. Lu, X. Wei, J. Li, G. Han, Z. Zhang, Zirconium doping in calcium titanate perovskite oxides with surface nanostep structure for promoting photocatalytic hydrogen evolution, Applied Surface Science, 542 (2021) 148544.
[235] L.J. Zhang, S. Li, B.K. Liu, D.J. Wang, T.F. Xie, Highly efficient CdS/WO3 photocatalysts: Z-scheme photocatalytic mechanism for their enhanced photocatalytic H2 evolution under visible light, ACS Catalysis, 4 (2014) 3724-3729.
[236] B. Wang, S. He, W. Feng, L. Zhang, X. Huang, K. Wang, S. Zhang, P. Liu, Rational design and facile in situ coupling non-noble metal Cd nanoparticles and CdS nanorods for efficient visible-light-driven photocatalytic H2 evolution, Applied Catalysis B: Environmental, 236 (2018) 233-239.
[237] M. Humayun, L. Xu, L. Zhou, Z. Zheng, Q. Fu, W. Luo, Exceptional co-catalyst free photocatalytic activities of B and Fe co-doped SrTiO 3 for CO 2 conversion and H 2 evolution, Nano Research, 11 (2018) 6391-6404.
[238] L. Ji, M.D. McDaniel, S. Wang, A.B. Posadas, X. Li, H. Huang, J.C. Lee, A.A. Demkov, A.J. Bard, J.G. Ekerdt, A silicon-based photocathode for water reduction with an epitaxial SrTiO 3 protection layer and a nanostructured catalyst, Nature nanotechnology, 10 (2015) 84-90.
[239] Y. Jin, D. Jiang, D. Li, P. Xiao, X. Ma, M. Chen, SrTiO3 nanoparticle/SnNb2O6 nanosheet 0D/2D heterojunctions with enhanced interfacial charge separation and photocatalytic hydrogen evolution activity, ACS Sustainable Chemistry & Engineering, 5 (2017) 9749-9757.
[240] H. Tan, Z. Zhao, W.-b. Zhu, E.N. Coker, B. Li, M. Zheng, W. Yu, H. Fan, Z. Sun, Oxygen vacancy enhanced photocatalytic activity of pervoskite SrTiO3, ACS applied materials & interfaces, 6 (2014) 19184-19190.
[241] L. Shi, W. Zhou, Z. Li, S. Koul, A. Kushima, Y. Yang, Periodically ordered nanoporous perovskite photoelectrode for efficient photoelectrochemical water splitting, ACS nano, 12 (2018) 6335-6342.
[242] X. Zhou, N. Liu, T. Yokosawa, A. Osvet, M.E. Miehlich, K. Meyer, E. Spiecker, P. Schmuki, Intrinsically activated SrTiO3: photocatalytic H2 evolution from neutral aqueous methanol solution

in the absence of any noble metal cocatalyst, ACS applied materials & interfaces, 10 (2018) 29532-29542.
[243] W. Zhao, W. Zhao, G. Zhu, T. Lin, F. Xu, F. Huang, Black strontium titanate nanocrystals of enhanced solar absorption for photocatalysis, CrystEngComm, 17 (2015) 7528-7534.
[244] H. Yu, J. Li, Y. Zhang, S. Yang, K. Han, F. Dong, T. Ma, H. Huang, Three-in-one oxygen vacancies: whole visible-spectrum absorption, efficient charge separation, and surface site activation for robust CO2 photoreduction, Angewandte Chemie International Edition, 58 (2019) 3880-3884.
[245] L. Liu, H. Huang, F. Chen, H. Yu, N. Tian, Y. Zhang, T. Zhang, Cooperation of oxygen vacancies and 2D ultrathin structure promoting CO2 photoreduction performance of Bi4Ti3O12, Science Bulletin, 65 (2020) 934-943.
[246] S. Kawasaki, R. Takahashi, M. Lippmaa, Gradient Carrier Doping as a Method for Maximizing the Photon-to-Current Efficiency of a SrTiO3 Water-Splitting Photoanode, The Journal of Physical Chemistry C, 123 (2019) 15551-15556.
[247] L. Kornblum, D. Fenning, J. Faucher, J. Hwang, A. Boni, M. Han, M. Morales-Acosta, Y. Zhu, E. Altman, M. Lee, Solar hydrogen production using epitaxial SrTiO 3 on a GaAs photovoltaic, Energy & Environmental Science, 10 (2017) 377-382.
[248] R. Kotnala, R. Gupta, A. Shukla, S. Jain, A. Gaur, J. Shah, Metal oxide based hydroelectric cell for electricity generation by water molecule dissociation without electrolyte/acid, The Journal of Physical Chemistry C, 122 (2018) 18841-18849.
[249] U. Bhakar, A. Agarwal, S. Sanghi, J. Shah, R.K. Kotnala, Production of green electricity from strained BaTiO3 and TiO2 ceramics based hydroelectric cells, Materials Chemistry and Physics, 262 (2021) 124277.
[250] P. Das, S. Das, S. Ratha, B. Chakraborty, S. Chatterjee, Ion beam engineered hydrogen titanate nanotubes for superior energy storage application, Electrochimica Acta, (2021) 137774.